CHAPTER 5
VALIDITY OF ESTIMATION FORMULA WITH NUMERICAL SIMULATION

5.1 General

The estimation formula for the collision force of drifted container modified in present study was compared with hydraulic model experiments for checking the validity of the formula in Chapter 2. In this chapter, the comparison with numerical experiments is conducted for validity of the estimation formula. For reproducing collision phenomena, the most popular way is the use of the finite element method. Aforementioned LS-DYNA is the representative finite element model, and the applicability was confirmed. Unlike other finite element models, the LS-DYNA enables to analyze the Fluid-Structure Interaction (FSI). Actually, not only the common finite element analysis such as vehicle collision (e.g., Atahan, 2006; Elmarakbi et al., 2006) and structural analysis (e.g., Tryland et al., 2004) but also the FSI analysis such as sloshing (e.g., Ma and Usman, 2004), bird strike (e.g., Souli etal., 2002; Hanssen et al., 2006), and water landing of space vehicle (e.g., Tutt, 2004) has been accomplished by using Arbitrary Lagrangian Eulerian (ALE) method (LSTC, 2003). The present study utilizes the ALE method described in above chapter for analysis of behavior of the container drifted by the run-up tsunami. Tokura and Ida (2005) investigated wave propagations in presence of flexible and rigid submerged structures by using ALE method. They, however, performed 2-dimensional analysis hence the total number of solid elements in fluid region reached 6000 only. And Tokura et al. (2006) carried out another 3-dimensional FSI simulation with ALE method, in which they estimated wave forces acting on a shore structure. However, wave generator was placed just in front of the revetment, and it is unreasonable to reproduce actual tsunami phenomena with long period. As described above, the researchers using LS-DYNA have taken various ideas for reducing calculation load because of extremely high calculation load in using LS-DYNA to reproduce the actual wave phenomenon. In the present study, combination of the drifting model based on the IB method and LS-DYNA is performed in order to reduce

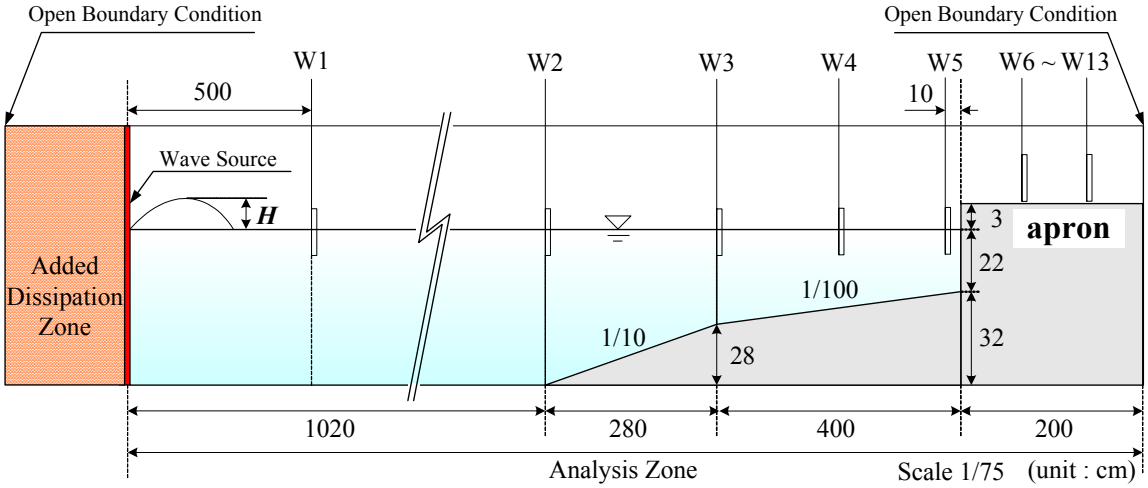

Fig. 5.1 Schematic figure of numerical wave flume for measurement of wave fluctuations and fluid velocities

calculation load in LS-DYNA and investigate behavior of the container drifted by run-up tsunami. The drifting model is employed from wave generation to container drifting while the collision model (LS-DYNA) is from just before the container collision. The results, which are drifting velocity of the container and wave level and fluid velocity behind container, from the drifting simulation are employed to the collision model as initial conditions. The collision force via this process is compared with the modified estimation formula to confirm the validity of the formula. First of all, verifications of the drifting, collision and coupled models are conducted.

5.2 Verification of Numerical Models

5.2.1 *Drifting model*

Fig. 5.1 shows a numerical wave flume for verifying the validity of the drifting model. An apron with impermeable vertical revetment and slops (1/10 and 1/100) are installed simply in the flume, and an added dissipation zone is placed in the left side of the wave source for non-reflection wave generation. The wave fluctuations at W1 to W13 and the fluid velocities at W7 to W9 are measured to compare with the hydraulic model experiments. The measurement points W1 to W5 are positioned at 5.0, 10.2, 13.0, 15.0 and 16.9m from the wave source and W6 to W13 are 0.1, 0.2, 0.3, 0.4, 0.5, 0.8, 1.3 and 1,8m from the edge of the apron.

The time variations of experimental and numerical wave fluctuations for incident wave Case 4 (see Table 2.1) are shown in Fig. 5.2. The circle and line represent the

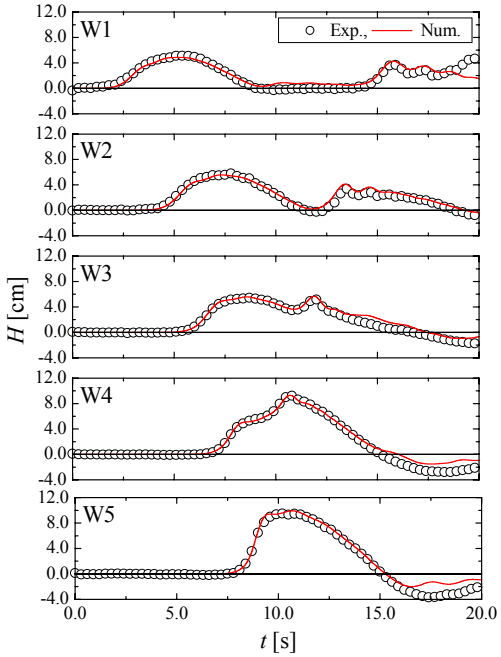

(a) Wave fluctuation at W1 to W5

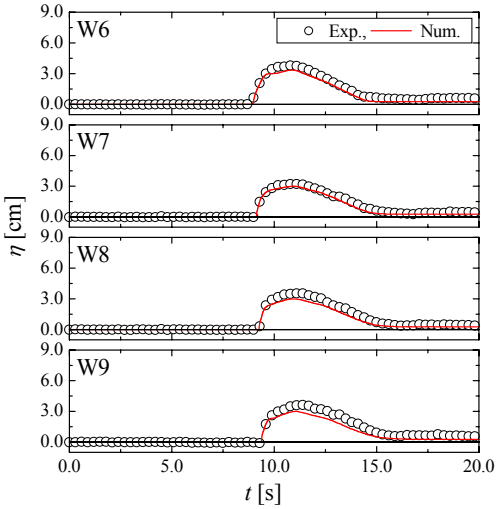

(b) Run-up wave fluctuation at W6 to W9

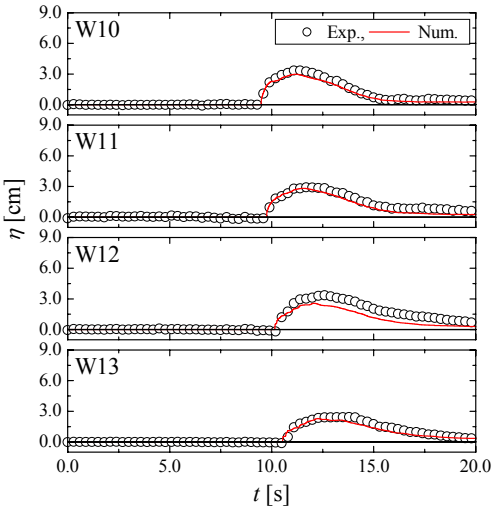

(c) Run-up wave fluctuation at W10 to W13

Fig. 5.2 Comparison of experimental and numerical wave fluctuations

experimental and numerical results, respectively. It is known that the numerical results are in good agreement with the experimental ones including reflected wave from the apron at W1 to W5 in seaward side. Besides, at W6 to W13 on the apron, it is found that the numerical results show a little underestimated tendency however the overall correspondence between both results is found.

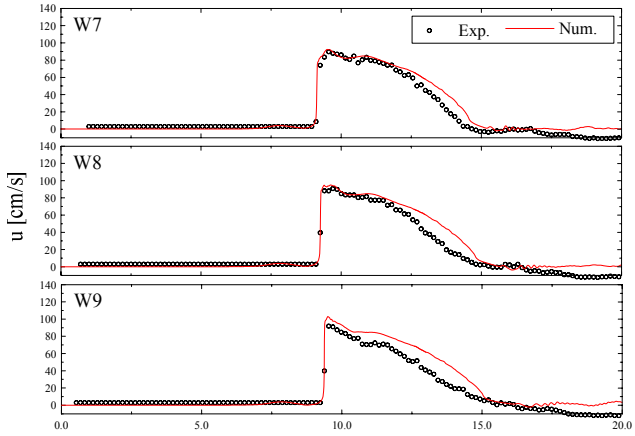

Fig. 5.3 Comparison of experimental and numerical fluid velocities at W7 to W9

Fig. 5.3 shows the time variations of the experimental fluid velocities and the numerical ones. From the figure, the numerical result is slightly overestimated the experimental one at W9, however it is found that the numerical results predict the experimental ones in a good degree on the whole.

For comparison of drifting behavior of the container, the numerical and laboratory experiments were conducted as illustrated in Fig. 5.4. The figure depicts the numerical experiment setup, and the container is initially placed at x_c=50cm from the edge of the apron. Case 4 in Table 2.1 was generated as the incident wave, and the container model was employed FT40G5 in Fig. 2.2 and Table 2.2. The numerical simulation was performed by half in y-direction because of symmetrical configuration.

In the laboratory experiment, video cameras were installed at the upper and lateral sides of the apron to record the behavior of the drifted container. The behavior of the container is related to the coefficient of friction between the container and the apron. In order to reproduce exactly the behavior of drifted container in the laboratory experiment, the author calibrated the coefficient of friction in the numerical experiment to the laboratory experimental one. Because duration between the contact of the run-up wave and the container and the commencement of the container drifting depend on the coefficient of static friction, and because the drifting velocity of the container depends on the coefficient of kinetic friction, the numerical coefficients of friction were adjusted to the experimental ones through tuning the aforementioned coefficients of static and kinetic frictions. Hence the conditions of the numerical simulation for comparison of the drifting behavior with the laboratory experiment were prepared. As the results, the coefficient of static friction (μ_s) was 2.0 while the coefficient of kinetic friction (μ_k) was 0.3 in the laboratory experiments. However the coefficient of static friction (μ_s) of 2.0 is too large value as compared with general one. The author found out that the

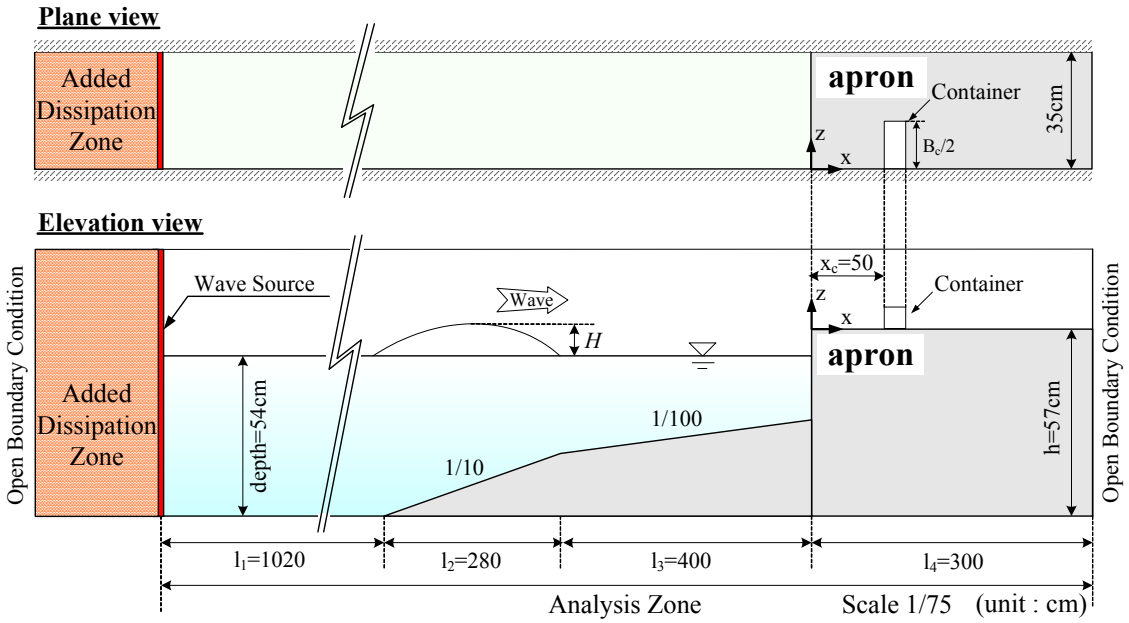

Fig. 5.4 Schematic figure of numerical wave flume for the container drifting

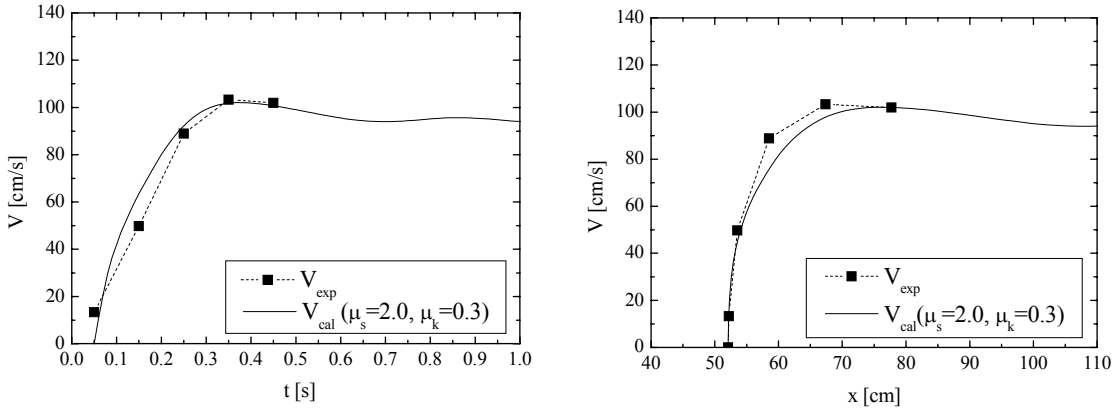

(a) Time variation (b) Spatial variation

Fig. 5.5 Drifting velocities of the container in laboratory and numerical experiments

coefficient of friction between the container and apron in the laboratory experiments was depended on viscosity due to the presence of moisture on the apron. Therefore the laboratory experiments had a too large coefficient of static friction. Fig. 5.5 shows the drifting velocities of the container by the laboratory and numerical experiments. Fig. 5.5 (a) and (b) represent the time and spatial variations of the drifting velocities, and dotted line with solid square and solid line indicate the experimental and numerical results, respectively. From the figures, it is known that the commencement and velocity of the drifted container just before collision (regarding collided body placed at x=80cm) of the numerical simulation are in accordance with the experimental ones.

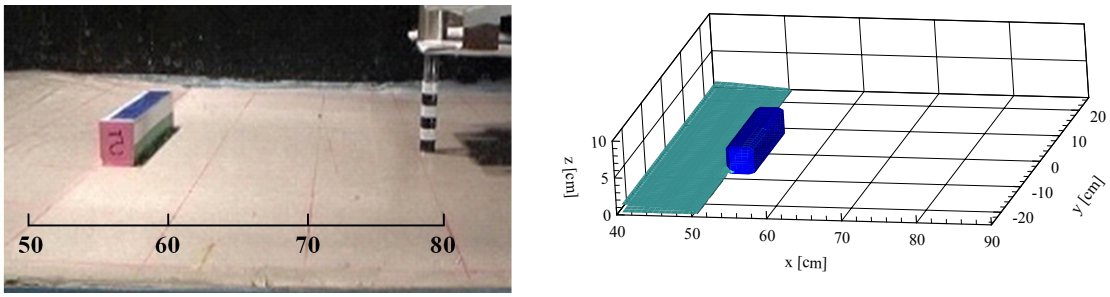

(a) At the moment contacting run-up wave to container

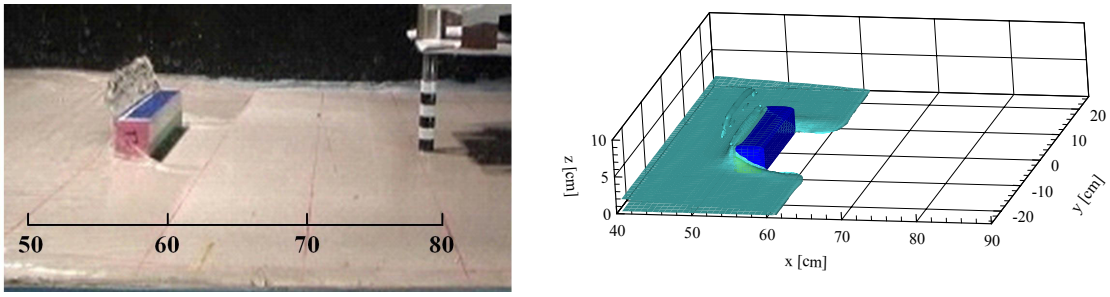

(b) After 0.1s

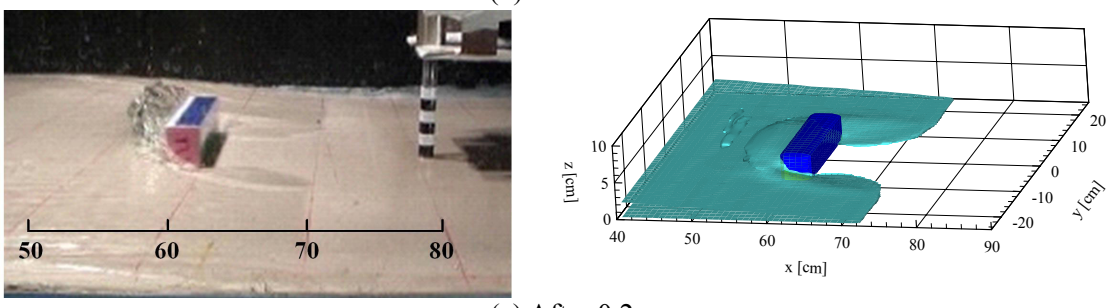

(c) After 0.2s

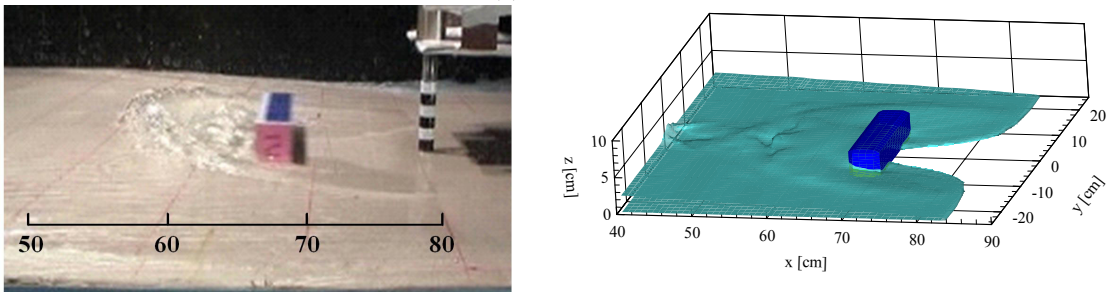

(d) After 0.3s

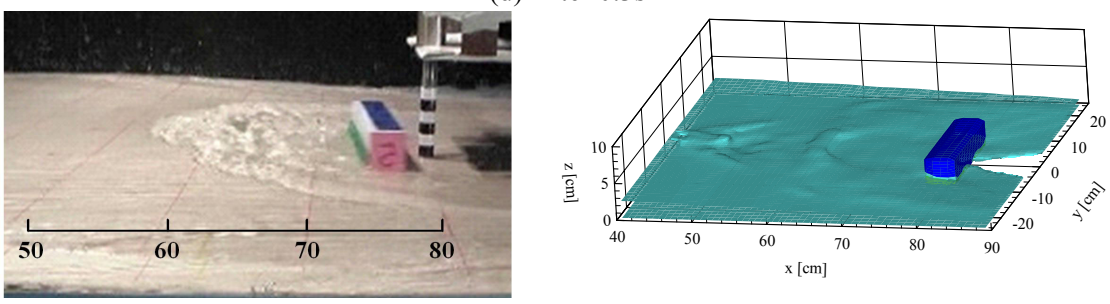

(e) After 0.4s

Fig. 5.6 Comparison of behavior of drifted container (Left: experimental results; Right: numerical results; Incident wave: Case 4; Container model: FT40G5; Initial position: x_c=50cm)

Then the behavior of the drifted container by the numerical simulation is compared with the experimental one in Fig. 5.6. The left and right figures represent the experimental and numerical results, respectively, and the moment of contact of the run-up wave to the container is set t=0.0s. From the figure, it is known that the positions of the drifted container and the deformations of the run-up wave behind the container in the numerical simulation predict well the experimental ones.

From the above results, the validity of the drifting model is confirmed, and verification of the collision model is conducted in next subsection.

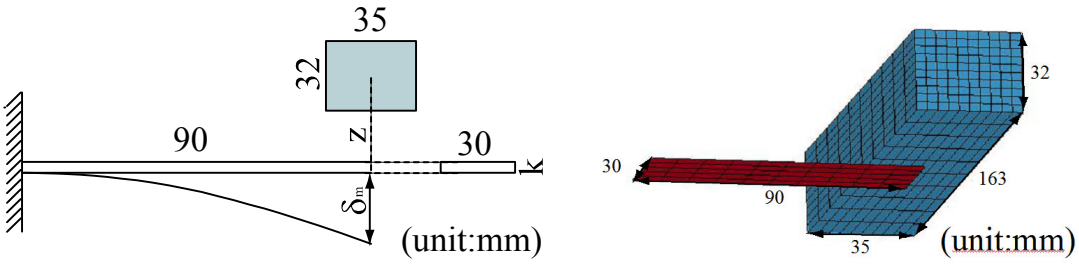

(a) Laboratory experiment (b) LS-DYNA

Fig. 5.7 Models for free falling test

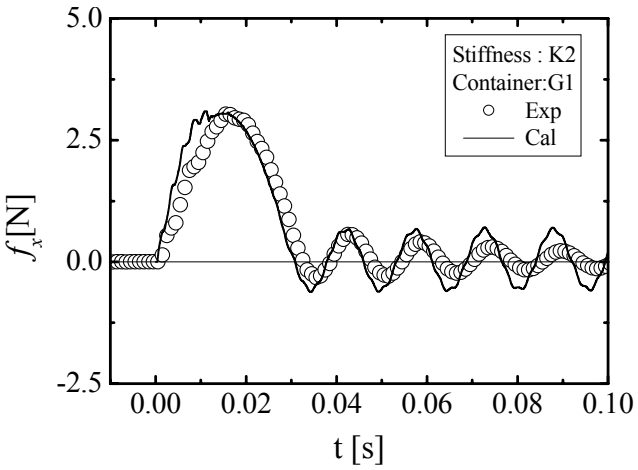

Fig. 5.8 Collision forces from the laboratory experiment and LS-DYNA on free falling test.

5.2.2 *Collision model*

Applicability of the collision model, LS-DYNA, is examined through the model test using a freely falling container. In the model experiment, FT40G2 container model mentioned in Fig. 2.2 and Table 2.2 was dropped from 100mm (z) above onto the end of

the k2 (thickness 2mm) acrylic resin plate. Fig.5.7 illustrates the model experiment and its modeling used in LS-DYNA. In the numerical simulation, container and plate models are considered as elasticity, and the physical properties were employed identically, in which the Young's ratio is 3.14E3 MPa; and the Poisson's ratio is 0.23. In the laboratory experiment, the collision force was calculated from the relationship between displacement at the edge of the plate and strain gauge attached on the plate, and in the LS-DYNA, from relationship between displacement at the edge of the plate and bending stiffness obtained from the laboratory experiments by using the concept of load acting on cantilever. The time variations of the collision forces by the laboratory experiment and LS-DYNA are shown in Fig. 5.8. The circle and line represent the experimental and numerical results, respectively. A fairly good agreement between two results is found and it can be concluded that the LS-DYNA is applicable to simulate the collision of container.

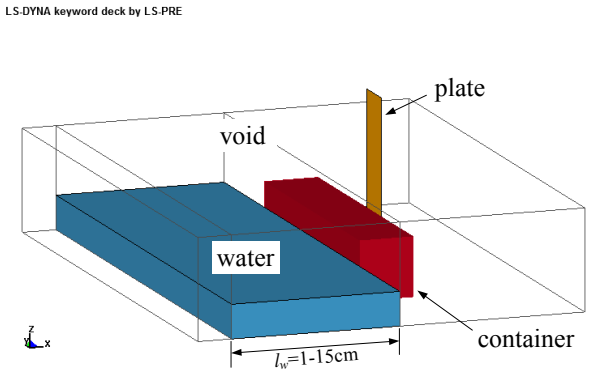

Fig. 5.9 Initial condition of numerical simulation for effective water length

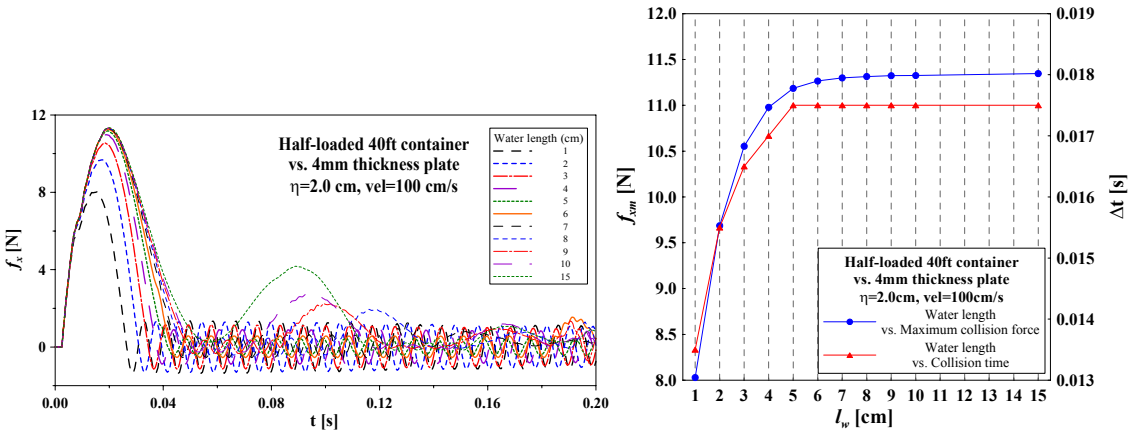

(a) Time variations of the collision force (b) Maximum collision force and collision time as varying water length

Fig. 5.10 Simulation results for effective range of run-up wave behind the drifted container

Table 5.1 Physical properties of collision simulation for determination of effective wave range

	Material type	Young's ratio E [MPa]	Poisson ratio	Viscosity coefficient μ [g/cm·s]
Container	Mat_1-Elastic	3.14E3	0.23	-
Plate	Mat_1-Elastic	1.85E3	0.23	-
Column	Mat_3-Plastic_Kinematic	2.06E5	0.30	-
Water	Mat_9-Null	-	-	1.002E-2

5.2.3 *Drifting collision coupled model*

5.2.3.1 Determination of wave range behind container

The validations of the drifting and collision (LS-DYNA) models were confirmed, then validity of drifting collision coupled model will be verified. We know that the coupling of the drifting and collision models, in which results in the drifting model is used as initial conditions of the LS-DYNA, is performed in order to reduce calculation load in the LS-DYNA for the drifting collision simulation. Hence it is very important to determine the range of the run-up wave behind the drifted container in aspect of reducing calculation load.

In order to grasp the effective range of the run-up wave behind the container, the numerical simulations were carried out with the LS-DYNA as shown in Fig. 5.9. The container model is employed FT40G2 (half-loaded 40ft container scaled in 1/75) in Fig. 2.2 and Table 2.2, and k4 (thickness 4mm) plate model with 2.4cm wide and 8.3cm high is used. The run-up wave behind the container is modeled as 30.0cm wide and 2.0cm high, and the length (0) of the wave column is varied from 1.0 to 15.0cm. The container and wave move together toward to the plate with initial velocity 100cm/s, and midpoint of the container collides at the end of the plate. The plate fixed upper side is regarded as a cantilever hence the collision force is calculated from the relationship between displacement of the end of the plate and the bending stiffness. Then the collision force is examined according to varying length of behind wave. Details of physical properties of the container, plate and water models used in these simulations are listed in Table 5.1. The container and plate are modeled by Lagrangian elements while the water and void by Eulerian elements for ALE method. Fig. 10 (a) represents the time variations of the collision force as varying wave length behind the drifting container. The maximum collision force shows the similar value after l_w=5cm. For detailed discussion, the maximum collision forces (f_{xm}) and the collision times (Δt) are represented in Fig. 10 (b). In the figure, the circle and triangle denote the maximum collision force and

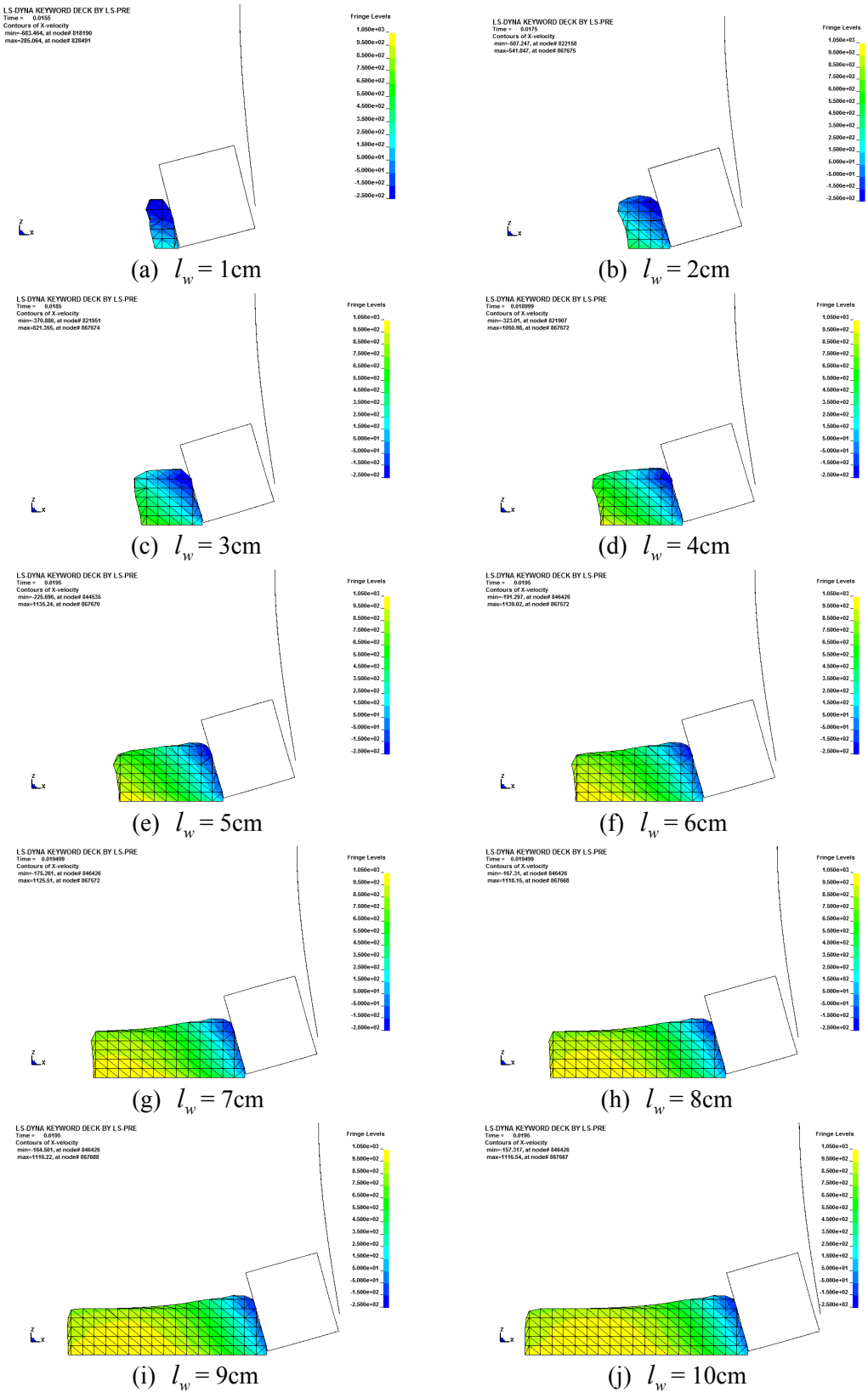

(a) $l_w = 1\text{cm}$ (b) $l_w = 2\text{cm}$

(c) $l_w = 3\text{cm}$ (d) $l_w = 4\text{cm}$

(e) $l_w = 5\text{cm}$ (f) $l_w = 6\text{cm}$

(g) $l_w = 7\text{cm}$ (h) $l_w = 8\text{cm}$

(i) $l_w = 9\text{cm}$ (j) $l_w = 10\text{cm}$

Fig. 5.11 Distribution of fluid velocity behind the drifted container

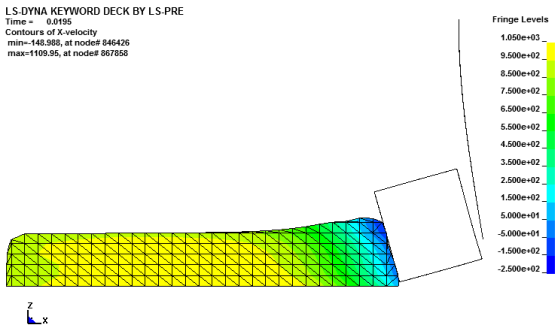

(k) l_w = 15cm

Fig. 5.11 Continued

collision time according to changing wave length, respectively. From the figure, the maximum collision force shows nearly uniform value after l_w=6cm and the collision time after l_w=5cm. Consequently, it is said that both a maximum collision force and a collision time represent constant values when the length of run-up wave behind the drifted container is larger than a particular length (in the present study, the length is 6cm).

The distribution of the fluid velocity on midsection behind the container at the moment of the maximum collision force is shown in Fig. 5.11. Deceleration is confirmed in the whole water for l_w=1cm to 5cm (Fig. 5.11 (a) - (e)) whereas it is found that the initial velocity 100cm/s was not changed at the rear side of the water after l_w=6cm (Fig. 5.11 (f)). It represents the same tendency with Fig. 5.10. From this point, some parts of water behind the container act as an added mass for the collision, not whole part. The effective range of the run-up wave behind the container depends on the conditions of colliding and collided bodies. Therefore the distribution of fluid velocity behind the drifted container at the moment of maximum collision force should be confirmed to judge appropriateness of the water length considered in the numerical simulation.

5.2.3.2 Validity of coupled model

Coupling scheme using the drifting and collision models verified is discussed. The applicability of the drifting collision coupled model, which the results in the drifting model is used in the collision model as initial conditions, is verified through the comparison with laboratory experiments. Two comparisons are performed, in which an acrylic resin plate model and a steel column model are employed as the collided body.

At first, it is described on the collision with the acrylic resin plate. The laboratory

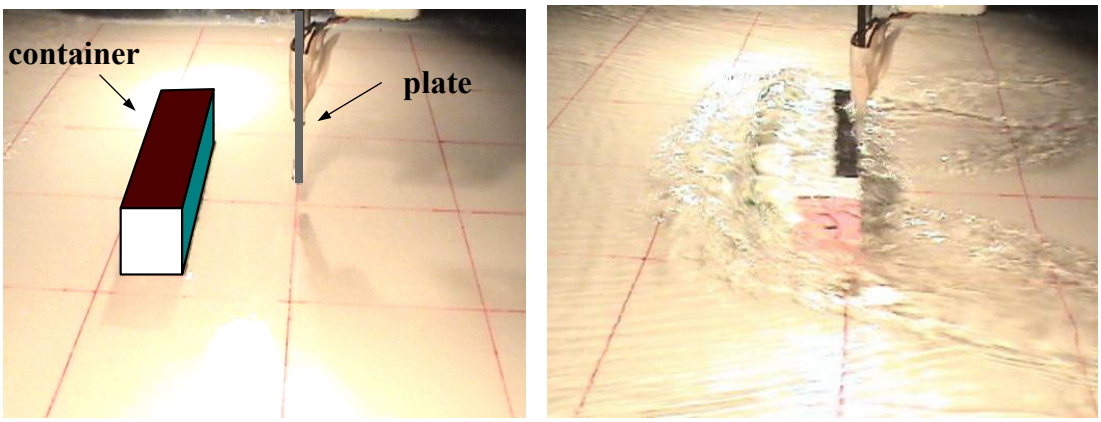

(a) Initial setup (b) moment of collision

Photo 5.1 Laboratory experiment for drifting collision of FT40G6 with k4 plate generated by Case 4

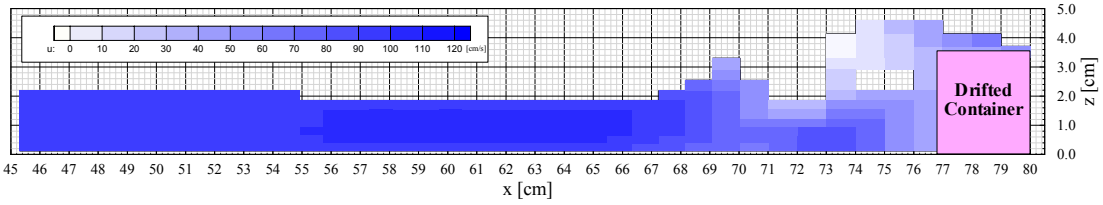

Fig. 5.12 Distribution of fluid velocity behind the drifted container FT40G6 with incident wave Case 4

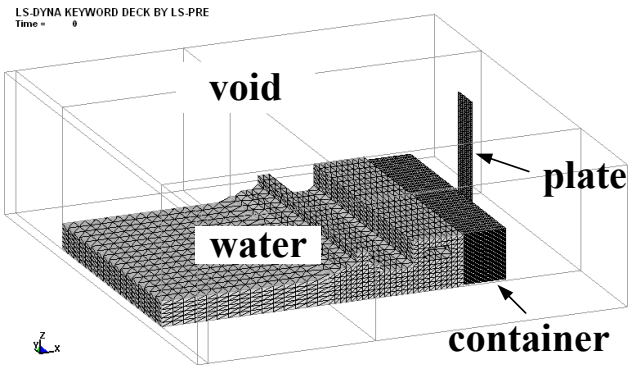

Fig. 5.13 Geometry of the collision model (LS-DYNA) using Fig. 5.9 as initial condition

experimental setup is same as that shown in Fig. 5.4 except for x_c and container model. This experiment was employed x_c = 70cm and FT40G6 container model (see Fig. 2.2 and Table 2.2). The acrylic resin plate and incident wave are also identical with above simulation as k4 and Case 4. Photo 5.1 (a) and (b) shows the initial set up and wave deformation for the collision.

In order to reproduce the behavior of drifted container in the laboratory experiment,

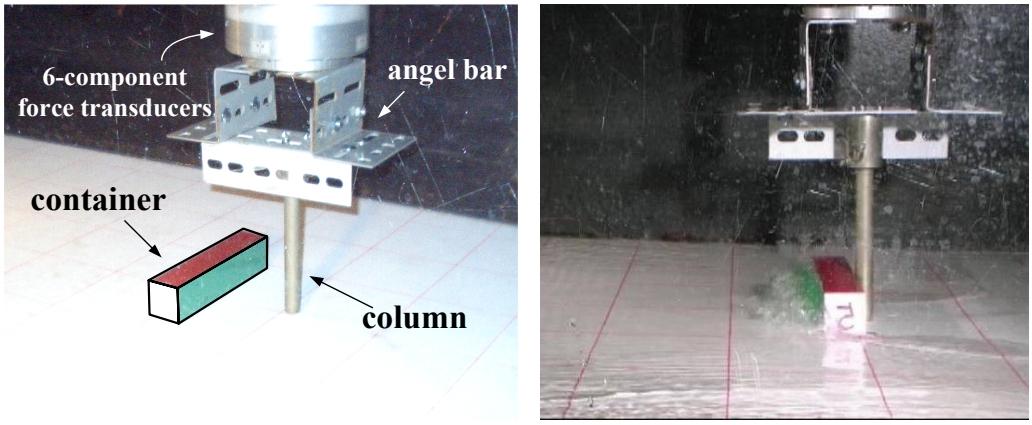

(a) Initial setup (b) moment of collision

Photo 5.2 Laboratory experiment for drifting collision of FT40G5 with the steel column

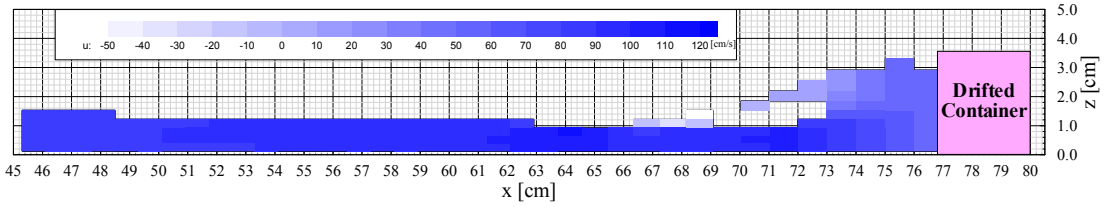

Fig. 5.14 Distribution of fluid velocity behind the drifted container FT40G5 with incident wave, T=6.5s and H=3.76cm

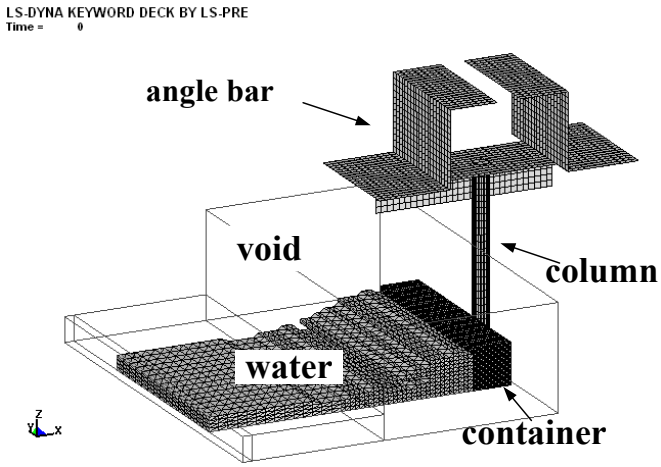

Fig. 5.15 Geometry of the collision model (LS-DYNA) using Fig. 5.11 as initial condition

the coefficients of friction in the numerical experiment was adjusted with same concept in Fig. 5.5, in which the coefficients of static (μ_s) and kinetic (μ_k) frictions are 1.0 identically. Distribution of the fluid velocity behind the drifted container just before collision is shown in Fig. 5.12, and then the shape of wave and fluid velocity are modeled as shown in Fig. 5.13 by utilizing LS-DYNA (collision model). Since the ALE

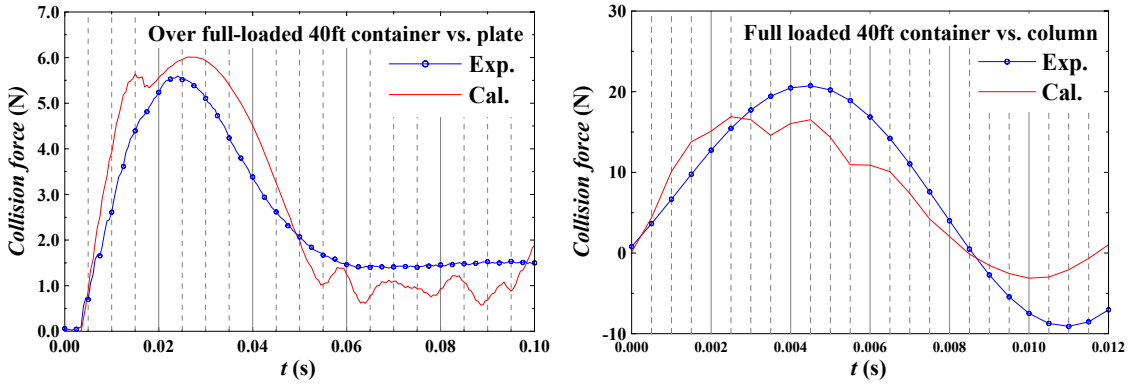

(a) Collision with plate (b) Collision with steel column

Fig. 5.16 Time variations of the collision force by laboratory experiment and drifting collision coupled numerical simulation

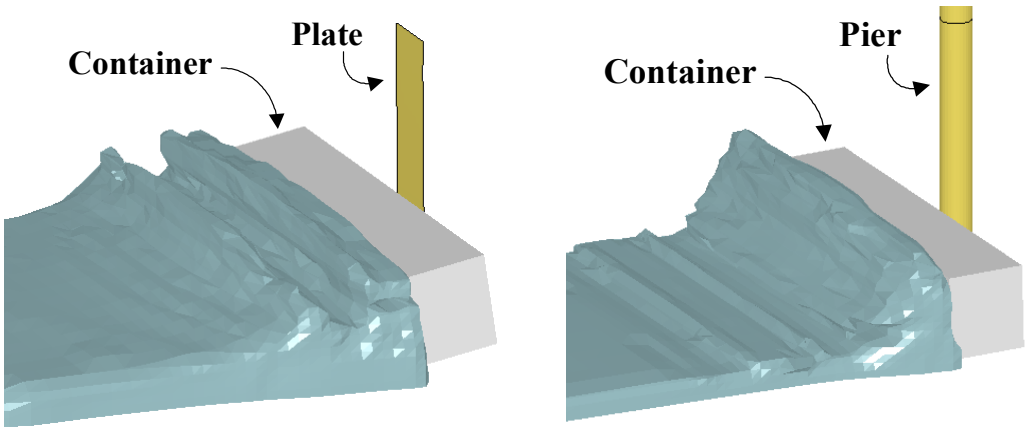

(a) Collision with plate (b) Collision with steel column

Fig. 5.17 Examples of FSI analysis using LS-DYNA

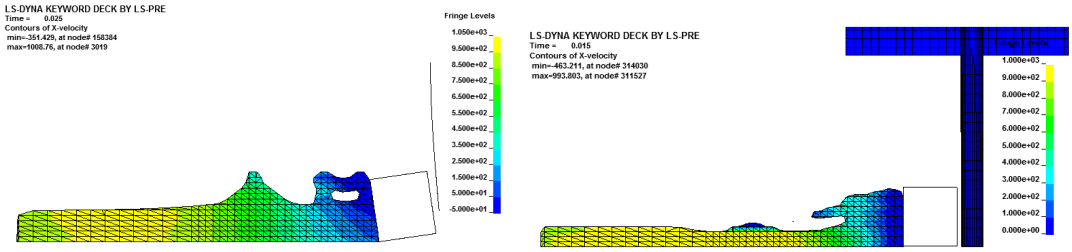

(a) Collision with plate (b) Collision with steel column

Fig. 5.18 Distributions of the fluid velocity behind the drifted container at the moment of the maximum collision force

method was also adopted for Fluid-Structure Interaction (FSI) analyses, and the container and the plate were modeled by Lagrangian elements, and the water and void by Eulerian element. The physical properties used in this collision simulation are listed

in Table 5.1.

Next, it is described on the collision with the steel column. The apron model was changed from Fig. 5.4 as depth=44.5cm, h=47cm and l_1=887cm, and the incident wave condition was employed into T=6.5s and H=3.76cm. The initial position of the container is same with above experiment as x_c=70cm, and FT40G5 (see Fig. 2.2 and Table 2.2) was used as the container model. The steel column with 15.4cm in height, 1.2cm in inside diameter and 0.2cm in thickness as the collided body is strongly fixed by angle bars to move together. And the collision force is measured by the six-component force transducers connected with the angle bars. The initial set up and wave deformation at the moment of the maximum collision force show in Photo 5.2

In this experiment, μ_s=2.05 and μ_k=0.7 were assessed as the coefficients of static and kinetic frictions respectively via the same way with above experiment. Fig. 5.14 represents the fluid velocity and wave deformation behind the drifted container just before collision, and Fig. 5.15 is the geometry in LS-DYNA using Fig. 5.14 as the initial condition. In the figure, the container, steel column and angle bars are modeled by the Lagrangian element while the water and void are modeled by the Eulerian element for FSI analysis using ALE method, and the physical properties were employed as Table 5.1.

The time variations of the collision force by the laboratory and numerical experiments are shown in Fig. 5.16. In the figure, (a) and (b) represent the results with the plate and steel column, and solid line with circle and solid line indicate the experimental results and numerical ones, respectively. From the results, although it is not able to found the accurate correspondence between the experiment and numerical results, the collision time and general tendency of the numerical results are in a good agreement with the experimental ones.

Fig. 5.17 shows FSI simulation results in aforementioned collision analyses by using ALE method of LS-DYNA, and it is found that the interaction between the container and the run-up wave behind container is accomplished in both numerical simulations.

To judge the pertinence of wave range considered in these numerical simulations, the distributions of the fluid velocity behind the container at the moment of the maximum collision force are shown in Fig. 5.18. It can be sad that the range of the run-up wave was proper because the fluid velocity of forepart is only changed.

As the above results, the validities of application of the drifting collision coupled model as well as the drifting and collision models were verified.

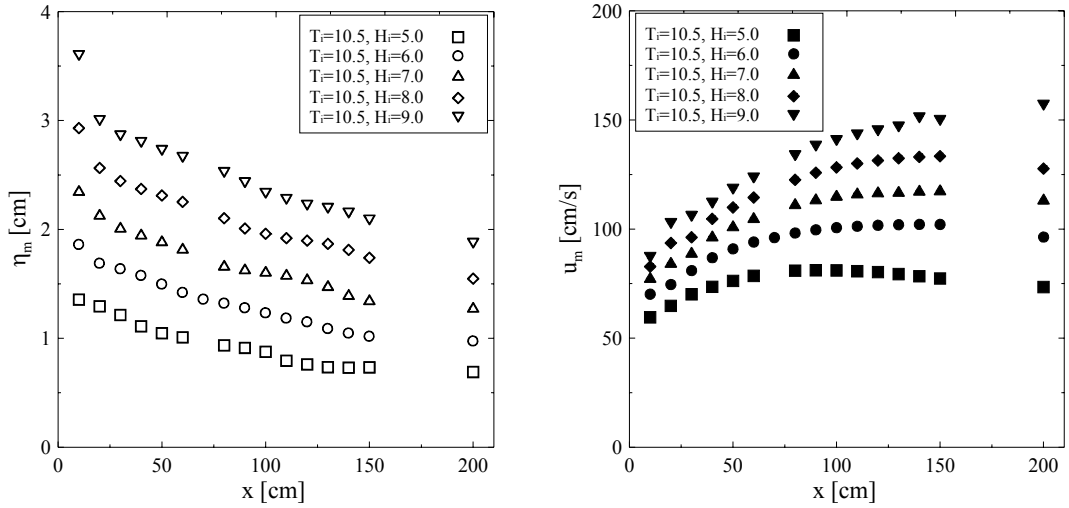

(a) Maximum run-up wave level (b) Maximum fluid velocity

Fig. 5.19 Spatial variations of maximum run-up wave level and maximum fluid velocity on the apron in absence of container

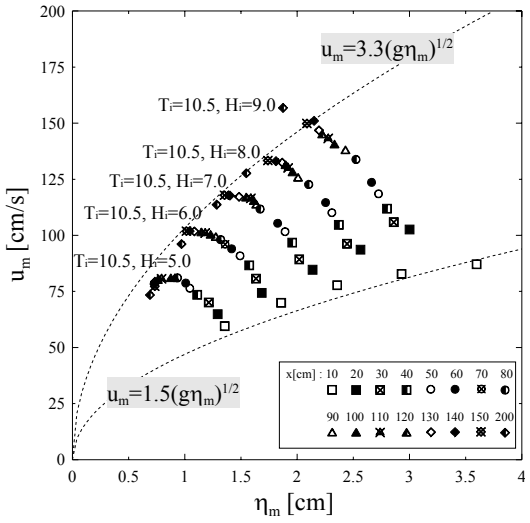

Fig. 5.20 Relationship between maximum run-up wave level and maximum fluid velocity

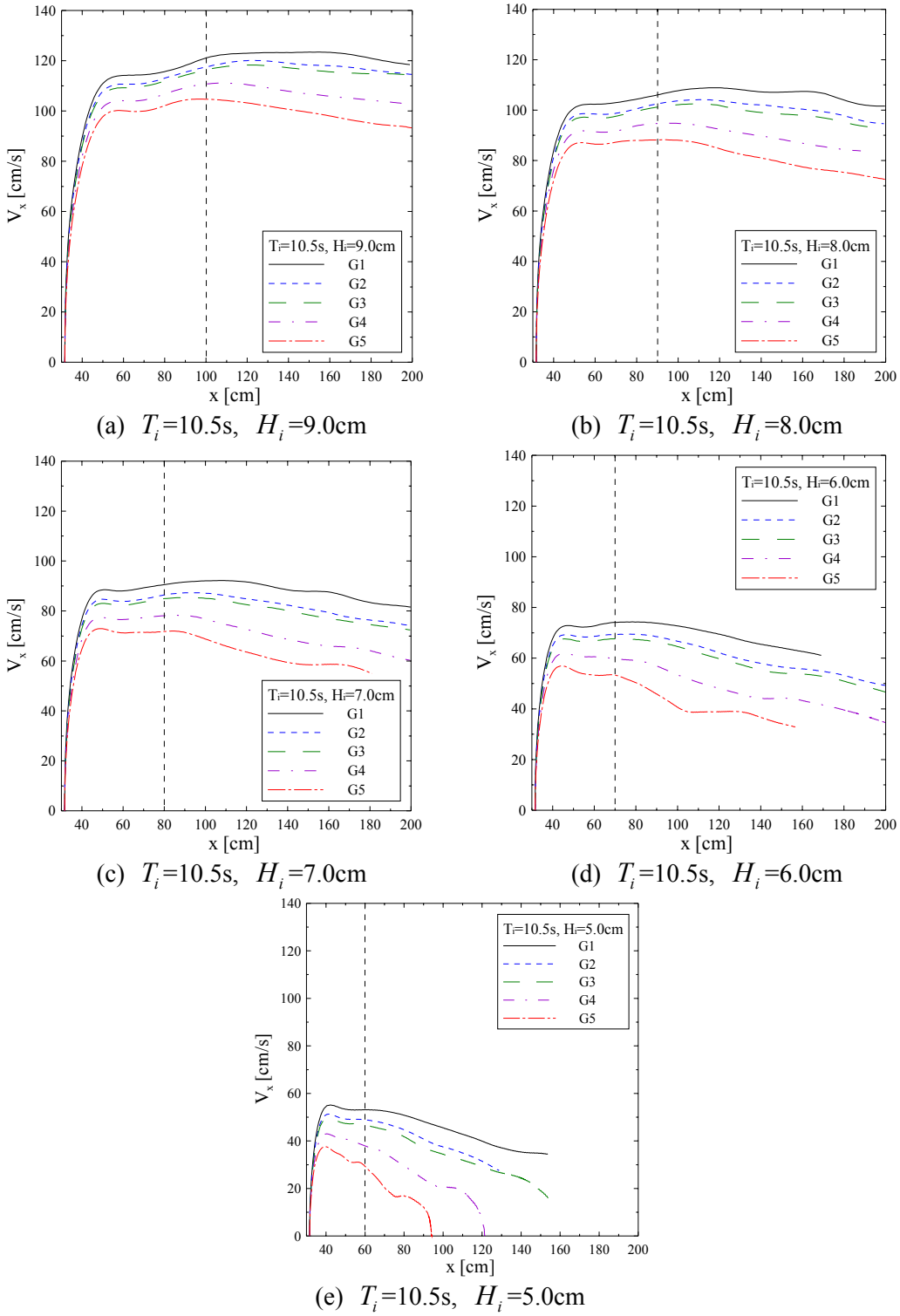

(a) T_i=10.5s, H_i=9.0cm (b) T_i=10.5s, H_i=8.0cm

(c) T_i=10.5s, H_i=7.0cm (d) T_i=10.5s, H_i=6.0cm

(e) T_i=10.5s, H_i=5.0cm

Fig. 5.21 Spatial variations of the drifting velocity of the container as changing incident wave

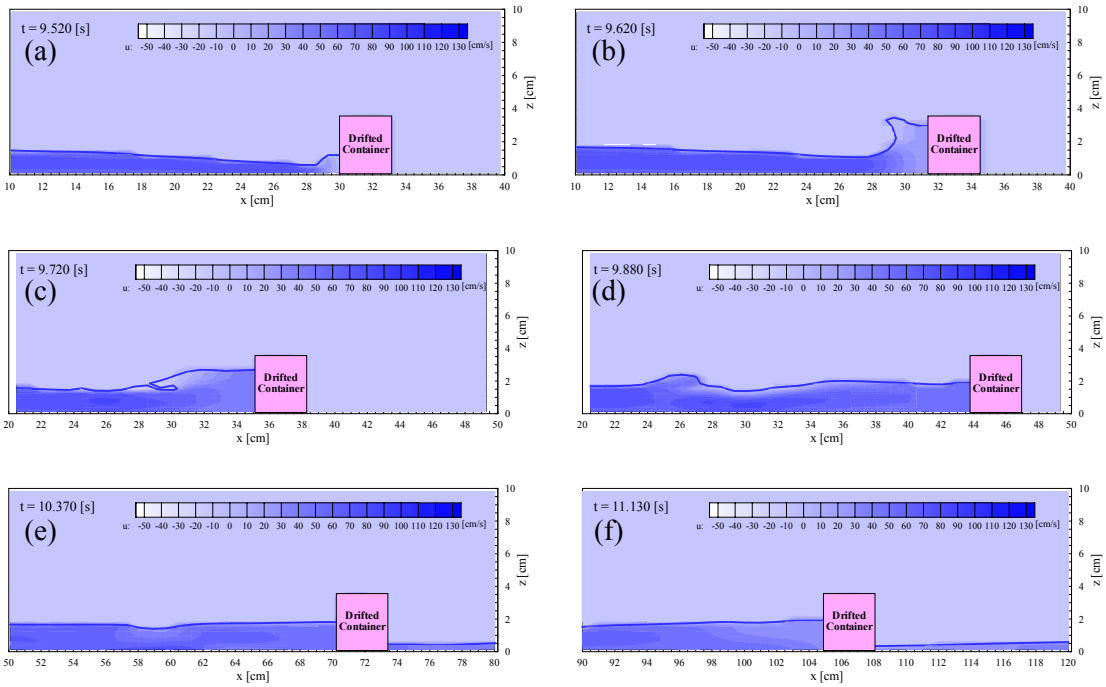

Fig. 5.22 Time variation of distribution of fluid velocity behind the container (T_i=10.5s; H_i=6.0cm; FT40G5)

5.3 Determination of Incident Waves

In order to grasp the relationship between drifting velocity of the container and run-up wave level behind container, the numerical experiments were conducted. The apron model was used as shown in Fig. 5.4, and five kinds of container models (FT40G1 - FT40G5; see Fig. 2.2 and Table 2.2) were employed for the drifting simulations with incident wave generated by T_i=10.5s, H_i=5.0 - 9.0cm, in which T_i and H_i are the incident wave period and the wave height of the long period wave, respectively.

At first, characteristics of the run-up wave on the apron in absence of container are discussed. Fig. 5.19 (a) and (b) depict the spatial variations of maximum run-up wave level and maximum fluid velocity on the apron. The effects of the wave height variation and the conservation of energy according to wave propagation are found from the figures. Then the relationship between the maximum run-up wave level (η_m) and the maximum fluid velocity (u_m) is shown in Fig. 5.20, in which the relationship is expressed as the Froude number ($u_m / \sqrt{g\eta_m}$). The range of the value is 1.5 - 3.3 in these numerical experiments, and this value represents the same degree with Matsutomi and Iizuka's (1998) Froude number (Fr=2.0) in dangerous condition. From the results, it

is known that the wave conditions employed in the numerical experiments are

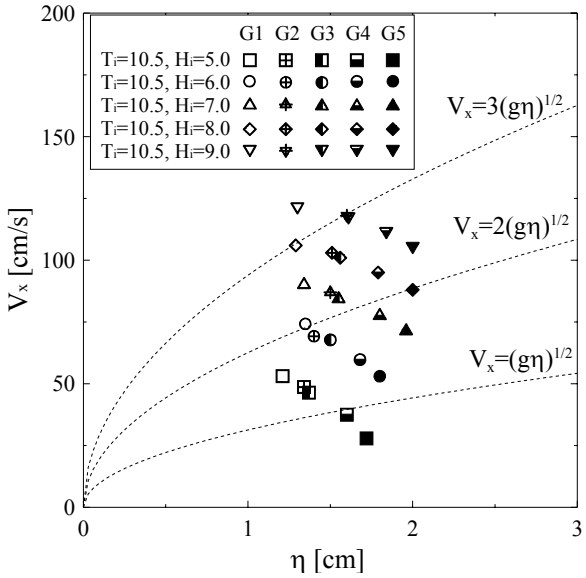

Fig. 5.23 Relationship between drifting velocity of the container and run-up wave level

correspond with general tsunami's.

The drifting numerical experiments were carried out to grasp the relationship of the drifting velocity of the container and run-up wave level behind container. The FT40G1 to FT40G5 (see Fig. 2.2 and Table 2.2) container models with initial position x_c=30cm were employed as drifting body, besides the coefficients of static and kinetic frictions were employed μ_s=0.4 and μ_k=0.3 referred to range of 0.3 to 0.4 for steel and stone in Design criterion of port and fishery harbor (Ministry of land, transport and maritime affairs, Korea, 2005). The spatial variations of drifting velocity of the container are displayed in Fig. 5.21, and the example of the time variation of the fluid velocity distribution for FT40G5, T_i=10.5 and H_i=6.0cm is represented in Fig. 5.22. From Fig. 5.21 (a) - (c), it is known that the drifting velocities reach the nearly peak value at x=100, 90 and 80cm. In Fig. 5.18 (d) and (e), however, the maximum drifting velocities are appeared at around x=40cm. From Fig. 5.22 (c) and (d), it is found that the shape of water surface behind the container at x=40cm is rough, while at Fig. 5.22 (e) (x=70cm) is flat. To considering simplicity of collision model, the drifting velocities of the container and run-up wave levels behind container for H_i=6.0 and 5.0cm were measured at x=70 and 60cm.

The relationship between the maximum drifting velocity of the container (V_x) and the run-up wave level (η) behind container is depicted in Fig. 5.23. It is difficult to correlate the maximum drifting velocity with the run-up wave level because the position of the maximum drifting velocity is varied with incident wave conditions. Hence the

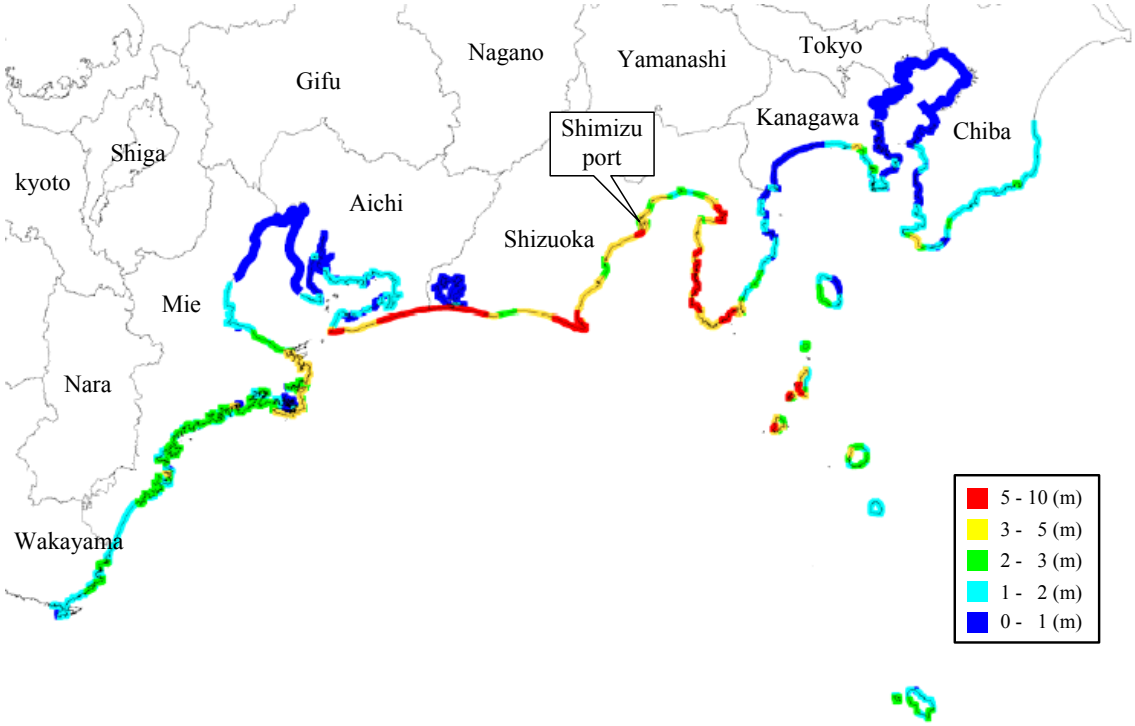

Fig. 5.24 Predicted tsunami height for Tokai-Earthquake by Cabinet Office, Government of Japan (Source: http://www.bousai.go.jp/)

Table 5.2 Incident wave conditions for Tokai-Earthquake

Case	T_i [s]	H_i [cm]
1	10.5	4
2	10.5	9
3	10.5	14
4	21.0	4
5	21.0	9
6	21.0	14
7	31.5	4
8	31.5	9
9	31.5	14

author selects the representative waves (tsunami), and calculates the drifting velocity of the container and run-up wave behind container used in collision analysis.

Then the author employs predicted tsunami heights for Tokai-Earthquake concerned in recent years as mentioned in Chapter 1. Cabinet Office, Government of Japan presented the predicted tsunami height on Tokai area by Tokai-Earthquake as shown in Fig. 5.24. The tsunami height on Shimizu port in Shizuoka prefecture containing a container terminal is considered, in which the tsunami heights are 3 - 5m in the port and 5 - 10m outside the port.

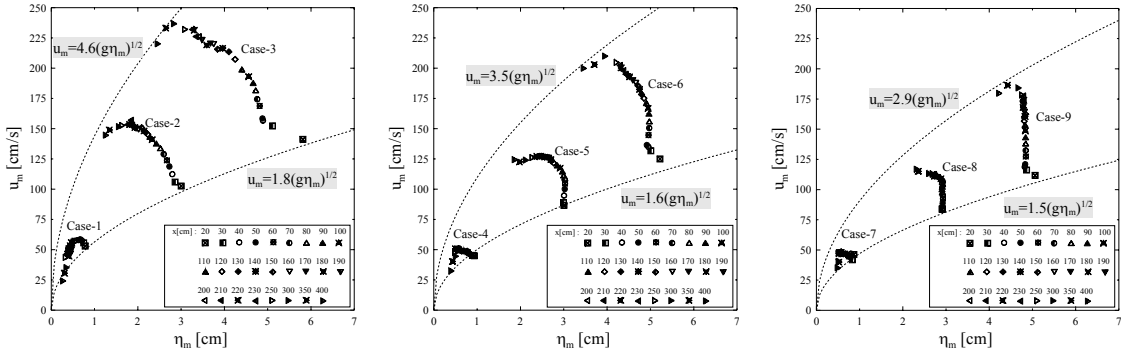

(a) Case 1, 2 and 3 (b) Case 4, 5 and 6 (c) Case 7, 8 and 9

Fig. 5.25 Relationship between maximum run-up wave level and maximum fluid velocity as varying wave heights

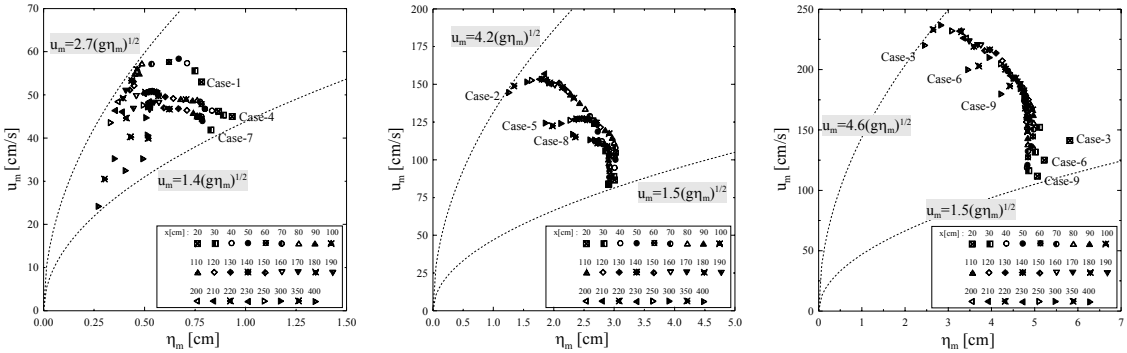

(a) Case 1, 4 and 7 (b) Case 2, 5 and 8 (c) Case 3, 6 and 9

Fig. 5.26 Relationship between maximum run-up wave level and maximum fluid velocity as varying wave periods

Table 5.3 Wave conditions using in drifting simulation

Case	T_i [s]	H_i [cm]	H_m [cm]	H_a [m]
1	10.5	4	4.97	3.7
2	10.5	9	10.41	7.8
3	10.5	14	16.03	12.0
5	21.0	9	9.95	7.5
8	31.5	9	9.67	7.3

To considering aforementioned conditions, the author selected the incident wave conditions as Table 5.2. To pick out the wave conditions using for drifting simulation, the run-up simulations are conducted in absence of container. The apron model in Fig 5.4 was adopted in this numerical simulation. As the results, the relationships between the maximum run-up wave level and the maximum fluid velocity as varying wave heights and wave periods are shown in Figs. 5.25 and 5.26. Among them, Case 1, 2 and 3 for influence of wave height and Case 2, 5 and 8 for influence of wave period, which

Table 5.4 Mass of container scaled in 1/75 and in full scale

Class	Scaled in 1/75 [g]			In full scale [t]		
	Empty	Half-loaded	Full-loaded	Empty	Half-loaded	Full-loaded
20ft container	4.553	26.361	48.168	1.921	11.121	20.321
40ft container	8.021	40.135	72.249	3.384	16.932	30.480

Table 5.5 Physical properties of collision simulation scaled in 1/75

	Material Type	Density ρ [t/mm^3]	Young's ratio E [MPa]	Poisson ratio	Viscosity coefficient μ [g/cm·s]
Container	Mat_1-Elastic	1.667	3.30E3	0.3	-
k4 Plate	Mat_1-Elastic	1.200	3.30E3	0.3	-
Water	Mat_9-Null	1.000			1.002E-2

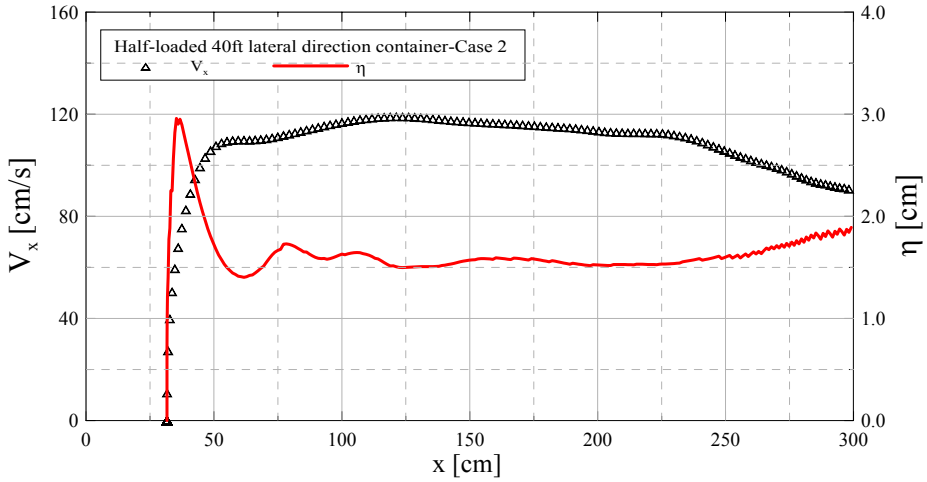

Fig. 5.27 An example of spatial variations of the drifting velocity of the container and the wave level

are representing clear tendency, are employed for the drifting simulations as the incident waves.

Table 5.3 lists the picked out wave conditions, in which H_m and H_a represent the wave levels above the still water level at the front of apron in the model tests and the actual field based on the Froude similarity law with a length ratio of 1/75, respectively. It indicates that these incident wave conditions considered in present study are capable of reproducing the tsunami heights (3 - 5m in the port and 5 - 10m outside the port) on Shimizu port for Tokai-Earthquake.

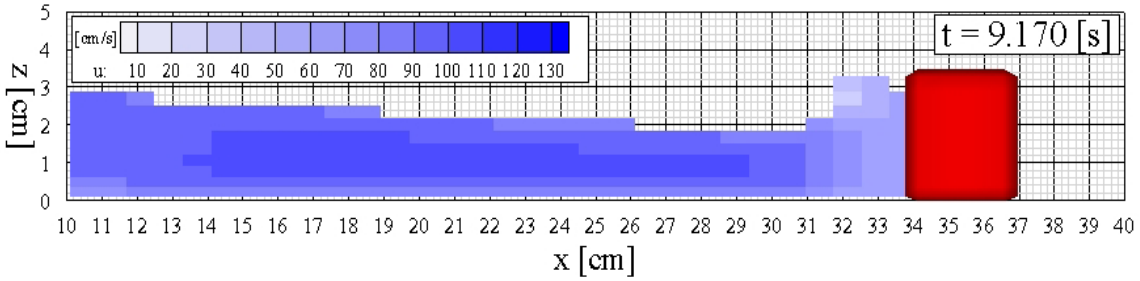

(a) Position of the maximum wave level

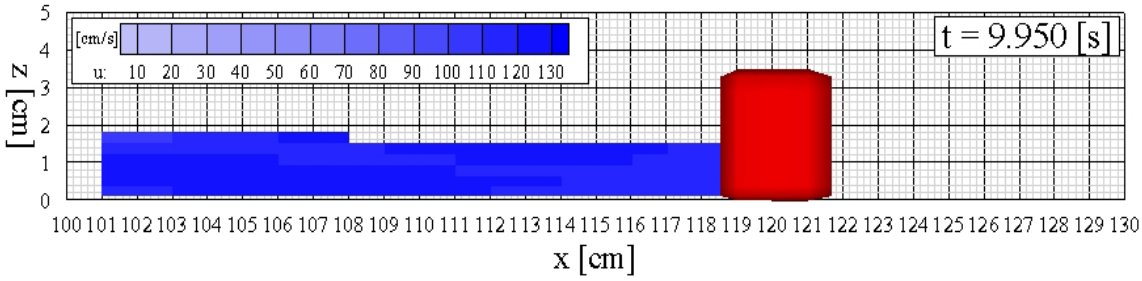

(b) Position of the maximum drifting velocity

Fig. 5.28 Distribution of the fluid velocity behind the container (Half-load 40ft container model; Case 2)

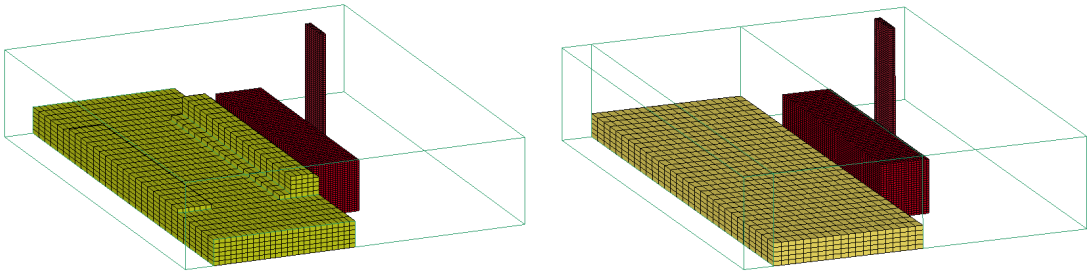

(a) Position of the maximum wave level (b) Position of the maximum drifting velocity

Fig. 5.29 Geometry of the collision model (LS-DYNA) using Fig. 5.28 as initial condition

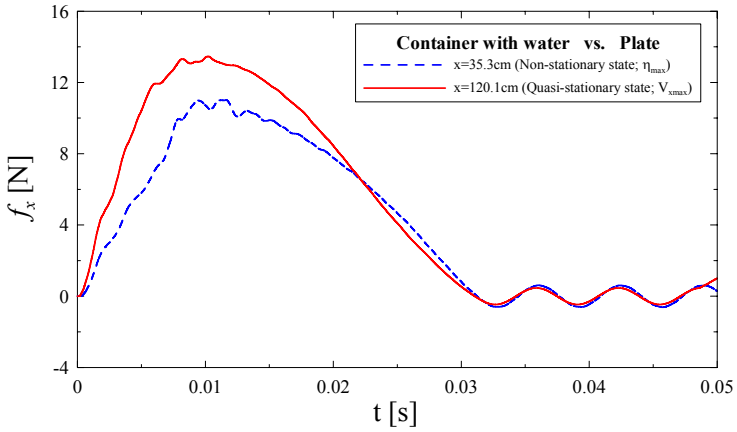

Fig. 5.30 Comparison of the collision forces using the maximum wave level and maximum drifting velocity

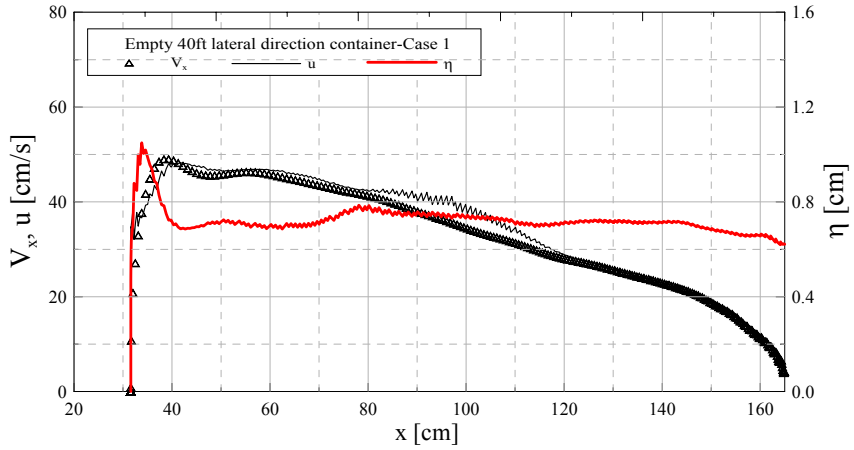

Fig. 5.31 An example of spatial variations of drifting velocity of the container, behind wave level and fluid velocity for the lateral direction empty 40ft container with the wave condition of Case 2

5.4 Collision Forces as Changing Position

The wave conditions used in drifting simulations were decided as shown in Table 5.3. However, it is important that which value from the drifting simulation is employed in the collision model. Therefore the author examined the collision force at representative positions of the drifted container. At first, a representative drifting simulation was conducted to obtain the drifting velocity of container, wave level behind the container and fluid velocity used in the collision simulation as the initial condition. The mass of container models scaled in 1/75 based on Froude similarity law for application to actual conditions are listed in Table 5.4, however the thickness is considered as 1mm uniformly. The numerical wave flume and apron model were used identically with Fig. 5.4 besides half-loaded 40ft container model (see Fig. 2.2 and Table 5.4) and Case 2 in Table 5.3 as the incident wave were considered. And the initial container model is place at x_c=30cm in lateral. The spatial variations of the drifting velocity (V_x) of the container and the wave level (η) behind container by the numerical drifting simulation are shown in Fig. 5.27, and the triangle (Δ) and line (—) indicate the drifting velocity and wave level. The author regarded that the positions of the maximum wave level behind the container (η_m; x=35.3cm) and the maximum drifting velocity of the container (V_{xm}; x=120.1cm) are dangerous conditions. Fig. 5.28 (a) and (b) depict the shapes of run-up wave and distributions of fluid velocity at η_m and V_{xm}, respectively. It is found that the wave level behind the container is high while the fluid velocity is slow in Fig. 5.28 (a), and the wave level is low while the fluid velocity is fast in Fig. 5.28 (b). The collision models used results in Fig. 5.28 are displayed in Fig. 5.29. The k4 (4mm thick) acrylic resin plate model as collided body and water model were constructed with solid element

while the container model with shell element. This simulation was also applied ALE method, so void area is considered to express deformation of the run-up wave as shown in Fig. 5.29. The comparison of the collision forces using the maximum wave level (η_{m}) and maximum drifting velocity (V_{xm}) is shown in Fig. 5.30. The horizontal and vertical axes represent the time and collision force, and the dashed and solid lines indicate the values at the maximum wave level in correspond to non-stationary state of the wave and the maximum drifting velocity in quasi-stationary state. From the figure, it is known that the collision force at the maximum drifting velocity (solid line) is greater than the value at the maximum wave level (dashed line). Here after, hence, the author considers the results (drifting velocity of container and wave level), which is employed in the collision simulation, at the maximum drifting velocity in the numerical drifting experiments.

5.5 Drifting Velocity and Wave Level by Drifting Simulation

In order to obtain the drifting velocity of container and run-up wave level behind container, wave condition and class, weight and initial direction of container are considered in numerical drifting simulations, in which five kinds of wave conditions as shown in Table 5.3, 20ft and 40ft containers in class, empty, half- and full-loaded containers in weight, and lateral and longitudinal directions of container are employed as calculation conditions. The author selects the incident wave period (T_i) 10.5s (correspond to 90.0s in actual condition) by considering wave profile separation and reflection from the structure, which is smaller than total tsunami period, and incident wave height (H_i) 4.0cm (4.97cm in scaled model and approximately 3.7m in actual condition at the coast) to considering tsunami height at Shimizu port for Tokai-Earthquake and lateral direction half-loaded 40ft container as the main calculation conditions. The numerical wave flume and apron model follow Fig. 5.4, and the initial position of the container is x_c=30cm.

As an example of results from the drifting simulation, the spatial variations of drifting velocity (V_x) of the container, behind wave level (η) and fluid velocity (u) for the lateral direction empty 40ft container with the wave condition of Case 2 are shown in Fig. 5.31. The triangle (Δ), fine line (−) and bold line (—) indicate the drifting velocity of the container, the fluid velocity behind container and wave level, respectively. From the figure, since it is known that the fluid velocity is identical with the drifting velocity of the container on the whole, it is capable of considering the drifting velocity into the

Tabl 5.6 Calculation conditions and results in the drifting simulations

T_i [s]	H_i [cm]	Class	Direction	Weight	η [cm]	V_x [cm/s]	$V_x/(g\eta)^{1/2}$	Test No.
10.5	4.0	40ft	Lateral	Empty	0.74	49.10	1.82	1
				Half	1.40	27.69	0.75	2
				Full	1.77	16.80	0.40	3
			Longitudinal	Empty	1.40	13.78	0.34	4
				Half	-	-	-	5
				Full	-	-	-	6
		20ft	Lateral	Empty	0.81	44.23	1.57	7
				Half	1.57	18.11	0.46	8
				Full	1.79	3.42	0.08	9
			Longitudinal	Empty	1.10	22.58	0.69	10
				Half	-	-	-	11
				Full	-	-	-	12
	9.0	40ft	Lateral	Empty	0.87	141.69	4.85	13
				Half	1.51	119.01	3.09	14
				Full	1.89	105.25	2.45	15
			Longitudinal	Half	3.31	66.04	1.16	16
		20ft	Lateral	Half	1.83	105.00	2.48	17
	14.0	40ft	Lateral	Half	1.80	186.03	4.43	18
21.0	9.0	40ft	Lateral	Half	1.53	94.33	2.44	19
31.5	9.0	40ft	Lateral	Half	1.56	75.60	1.93	20

fluid velocity in the collision simulation and estimation formula.

The calculation conditions and the drifting simulation results are listed in Table 5.6, in which the results are employed in the collision simulation as the initial conditions. Test No. 5, 6, 11 and 12 denote the non-drifted cases.

5.6 Comparison of Collision Forces by Collision Model and Estimation Formula

In order to verify the modified estimation formula (Eq. 3.6) for the collision force of the drifted container by the run-up tsunami, the numerical collision experiments using the

Table 5.7 Initial conditions for collision simulation scaled in 1/75

T_i [s]	H_i [cm]	Weight	η [cm]	V_x [cm/s]
10.5	9.0	Empty	0.9	141.7
		Half	1.5	119.0
		Full	2.0	105.3
	14.0	Half	1.8	186.0
21.0	9.0	Half	1.5	94.4
31.5	9.0	Half	1.6	75.6

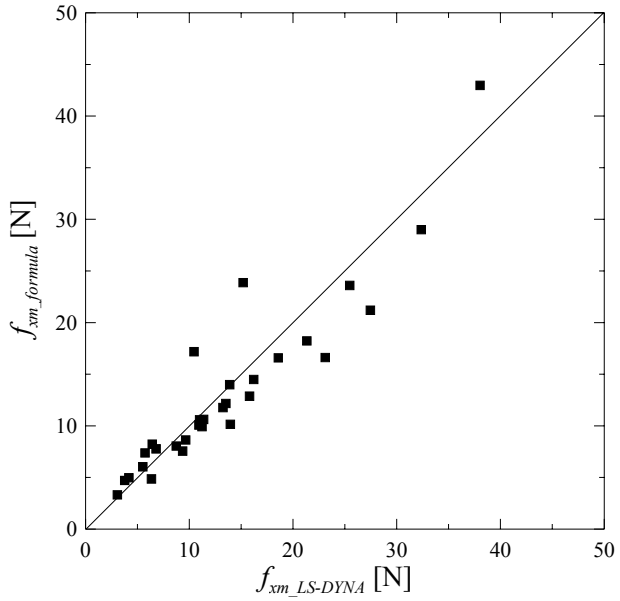

Fig. 5.32 Comparison of the maximum collision forces by the collision model and estimation formula

results (Table 5.6) from the container drifting simulations were carried out. The calculation method (ALE method) and coupling scheme are identical with Section 5.4. Six kinds of initial conditions (Test No. 13~15 and 18~20), which are considering effects of container weight, wave height and wave period, as shown in Table 5.7 are investigated, in which the values were adjusted a little for simplicity of modeling. Besides five kinds of acrylic resin plate (2 to 6mm in thickness) are employed as varying stiffness of the collided body, therefore thirty cases were conducted for the collision simulations.

The comparison of the maximum collision forces by the collision model (LS-DYNA) and the estimation formula (Eq. 3.6) are shown in Fig. 5.32. The horizontal and vertical axes indicate the values by the collision simulation and the modified estimation formula, respectively. In this figure, although some unevenness, the results from the estimation

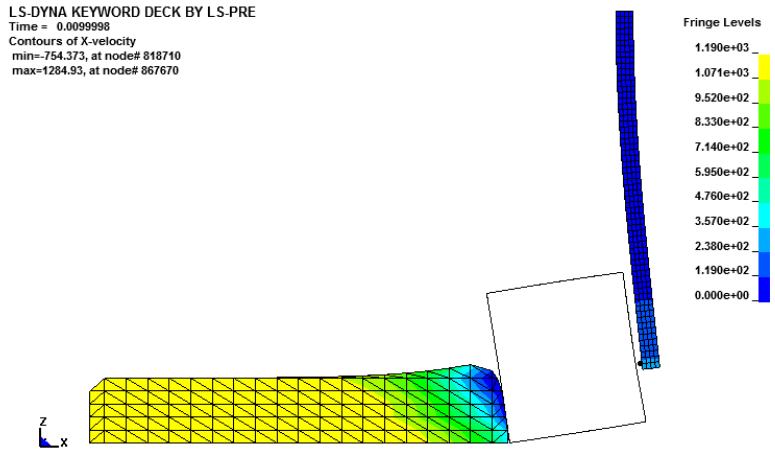

Fig. 5.33 An example of the distribution of the fluid velocity behind the container at the moment of maximum collision force (T_i=10.5s; H_i=9.0cm; lateral direction half-loaded 40ft container; and k4 plate)

formula are in good agreement with the numerical ones on the whole.

The author representatively illustrates the distribution of the fluid velocity behind the container at the moment of maximum collision force in Fig. 5.33, in which T_i=10.5s, H_i=9.0cm, lateral direction half-loaded 40ft container and k4 plate were used. It is found that the initial fluid velocity (V_x=119.0cm/s) is not decelerated in rear side of the run-up wave, hence it can be regarded that the range of run-up wave considered in these simulations was appropriate.

As above results, the validity of the modified estimation formula for the collision force of the drifted container is verified. And finally, the applicability of the formula to actual phenomenon is discussed in next chapter.

5.7 Remarks

In this chapter, the verification of the modified estimation formula was implemented through the comparison with numerical experiments. First of all, the validities of the drifting, the collision and the drifting collision coupled models were confirmed via comparisons with the experimental results.

As a result, the author obtained the following results:

1. In the present study, a drifting collision coupled model, which the results just before the collision in the drifting simulation are used in the collision model as initial conditions, was proposed.

2. The validity of the drifting model was verified through comparison with the experimental results for the wave levels, fluid velocities and drifting behaviors of the container, besides the applicability of the LS-DYNA for the collision analysis was confirmed through comparison with the freely falling experiments.
3. In determination of the wave range behind the drifted container, some part of wave behind the container acted as an added mass for the collision, not whole part. Since the effective range of the run-up wave behind the container is depended on the conditions of colliding and collided bodies, the distribution of fluid velocity behind the drifted container at the moment of maximum collision force should be confirmed to judge appropriateness of the wave length considered in the numerical simulation.
4. The drifting collision numerical analyses predicted the collision forces by the laboratory experiments employing the acrylic resin plate and steel column as the collided body, and reproduced well the interaction between the container and the run-up wave behind the container.
5. The author selected the representative waves for the drifting analysis based on the tsunami heights on Shimizu port for Tokai-Earthquake presented by Cabinet Office, Government of Japan.
6. The collision force at the maximum drifting velocity of the container was greater than at the maximum wave level, and furthermore the wave fields behind the container represented the quasi-stationary state.
7. The drifting velocity of container and the run-up wave level behind container were obtained in the drifting simulations by considering five kinds of wave conditions and variations of class, weight and initial direction of containers.
8. Six kinds of initial conditions, which considered effects of container weight, wave height and period, and five kinds of acrylic resin plate considering varying stiffness were employed as the colliding and collided bodies for the collision simulations, and then it was found that the results from the estimation formula were in good agreement with the numerical ones on the whole. Consequently, the validity of the modified estimation formula for the collision force of the drifted container was verified.

CHAPTER 6.
APPLICABILITY OF ESTIMATION FORMULA TO PROTOTYPE CONDITIONS

6.1 General

The validity of the estimation formula for the collision force of the drifted container by run-up tsunami was verified through comparison with laboratory and numerical model experiments in Chapters 3 and 5. In order to apply to actual field, however, it is necessary to compare with the tests in prototype condition. Matsutomi (1999) conducted large scale experiments to obtain a practical formula for estimating the collision force on structures due to a collision of driftwoods. He carried out small scale experiments in a channel while large scale experiments in the air. Furthermore subject of the present study is the full-scale freight container (20ft and 40ft containers) hence the laboratory experiments for the collision of the drifted container due to the run-up tsunami in the full-scale is more difficult actually because of enormous cost, time and limitations of facilities. To solve this difficulty, the estimation formula is verified through comparing with numerical analyses in full-scale by LS-DYNA, in which the same coupling scheme, which the model collisions employing the results in the drifting model as the initial conditions, is used. For these collision simulations, the results in the drifting simulations are considered as converted values into the full-scale based on the Froude similarity law.

First of all, verification of LS-DYNA is carried out in large scale then collision simulations are performed with full-scale back-yard structures as the collided bodies. And the estimation formula modified in Chapter 3 is revised to apply for large deformation phase also. The author presents the applicability of this estimation formula to prototype conditions, and finally describes on simplification of the estimation formula.

6.2 Verification of Collision Model in Large Scale

In order to use LS-DYNA in the verification of the estimation formula in the full-scale,

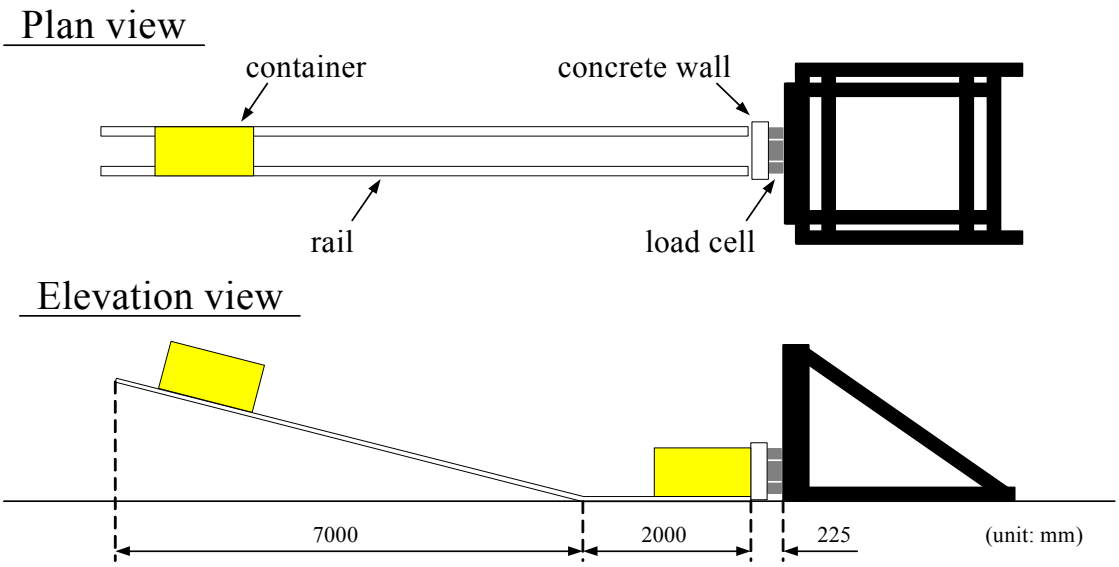

Fig. 6.1 Schematic figures for the free falling experiments in the air (Arikawa et al., 2007)

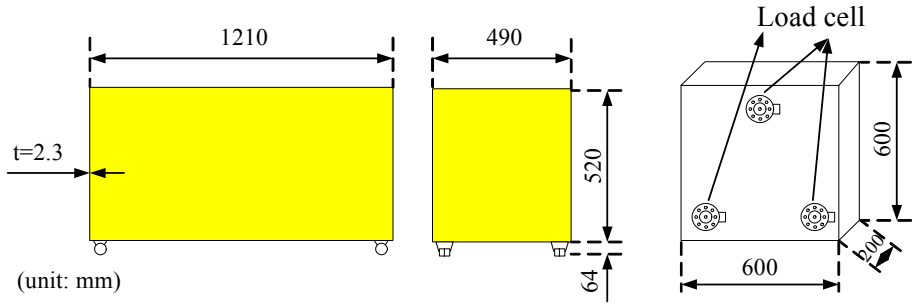

Fig. 6.2 Dimensions of the container and concrete wall, and load cells (Arikawa et al., 2007)

the author employed Arikawa et al.'s (2007) 1/5 scaled container collision experiments which is close to the full-scale. Through the comparison of the results in LS-DYNA and experiments, the applicability of LS-DYNA to prototype conditions is verified. It is proper to compare with the drifting collision experiments in order to using the results of the drifting collision simulation by LS-DYNA, however the author employed free falling experiments in the air due to difficulty of acquiring information for the drifting collision experiments.

Fig. 6.1 shows the schematic figure for the freely falling experiment in the air, and Fig. 6.2 represents the dimensions of the container and concrete wall as the colliding and collided bodies, respectively. The container model assumed ISO 20ft freight container (Japanese industrial standards committee, 1994) is freely fallen and collided with the concrete wall as shown in Photo 6.1. The container has $1210\times490\times520mm^3$ in

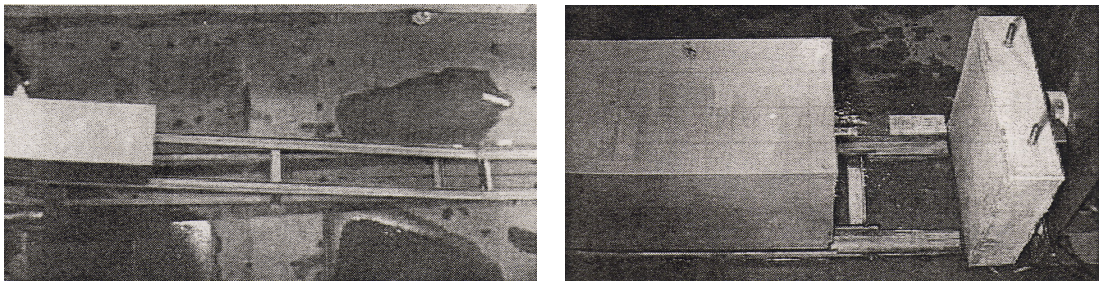

(a) Initial position (b) After collision

Photo 6.1 Video photos for free falling experiments in the air (Arikawa et al., 2007)

dimensions, 2.3mm in thickness and 62kg in mass while the concrete wall has $600\times600\times200mm^2$ in dimensions. The collision velocity was changed by varying heights (50, 75 and 100cm) of initial position of the container and tests were performed 10, 10 and 3 times, respectively. To measuring collision force, three load cells were utilized as shown in Figs. 6.1 and 6.2.

For this collision simulation using LS-DYNA, strain rate effects, controlling hourglass mode and specified concrete model were considered to predict the collision force more accurately. The literature (Ishikawa 1993) describes for strain rate effects on dynamic characteristics of steel materials as follows:

1) Yield stress, tensile strength and fracture toughness are increased as increasing strain rate, and increment of the yield stress is the biggest among them,
2) Young's modulus until yield stress is constant irrelevant to strain rate.

This simulation thus adopts Cowper-Symonds strain rate model (LSTC, 2003; Børvik et al., 2008) to consider the strain rate effects. The equivalent stress is expressed as

$$\sigma_{eq} = \left\{1 + \left(\frac{\dot{\varepsilon}_{eq}}{C}\right)^{1/p}\right\}\left(\sigma_0 + \beta E_p \varepsilon_{eq}\right) \tag{6.1}$$

and

$$E_p = \frac{E \cdot E_t}{E - E_t} \tag{6.2}$$

where σ_0 is the yield stress; ε_{eq} is the equivalent plastic strain; $\dot{\varepsilon}_{eq}$ is the equivalent plastic strain rate; E_p is the plastic hardening modulus; E_t is the tangent modulus;

E is Young's modulus; β is a hardening parameter between 0 (kinematic) and 1 (isotropic); ν is the Poisson's ratio; ε_f is the failure strain for eroding elements; and C and p are the strain rate parameters, in which $C = 40s - 1$ and $p = 5$ for mild steel, besides physical properties of the container model are listed in Table 6.1 (Børvik et al., 2008).

Furthermore, four points integrated shell element is used in the container model to remedy the hourglass energy mode. It is a numerical instability occurred where element distortions are large with one point integration. Certain modes of deformation of solid and shell elements are zero energy modes and have no stiffness. They typically give a zig-zag appearance to a mesh. It can swamp the results of an analysis. To remedy the

Table 6.1 Physical properties for free falling test

Container				
Material type	ρ [t/m^3]	E [MPa]	ν	σ_0 [MPa]
Mat_3-Plastic_Kinematic	9.126	2.1E5	0.3	355
E_t [MPa]	β	C [s-1]	p	ε_f
1000	1.0	40	5	0.8
Concrete wall				
Material type	ρ [t/m^3]	E_t [MPa]	ν	σ_c [MPa]
Mat_84-85-Winfrith_Concrete	2.4	3.1E4	0.2	40
σ_t [MPa]	R_a [mm]			
4	12.5			

Table 6.2 Default pressure versus volumetric strain curve for concrete if the curve is not defined

Volumetric strain	Pressure [MPa]
$-p_1 / K$	1.00× p_1
-0.002	1.50× p_1
-0.004	3.00× p_1
-0.010	4.80× p_1
-0.020	6.00× p_1
-0.030	7.50× p_1
-0.041	9.45× p_1
-0.051	11.55× p_1
-0.062	14.25× p_1
-0.094	25.05× p_1

hourglass energy situation, various vehicle components were either remeshed or were assigned fully integrated finite element formulations, and the later was employed in the present analysis.

For the concrete wall model, the Winfrith concrete model was used. It is capable of analysis smeared crack (sometimes known as pseudo crack). This model was developed by Broadhouse (1995) over many years and has been validated against experiments. Details of the physical properties for the Winfrith concrete model are also listed in Table 6.1 (JSCE Concrete Committee, 1996), in which E_t is the tangent modulus; σ_c is the uniaxial compressive strength; σ_t is the uniaxial tensile strength; and R_a is the aggregate size (radius). In LS-DYNA, if the volume compaction curve is omitted, a default pressure versus volumetric strain curve for concrete is automatically applied as shown in Table 6.2 where p_1 is the pressure at uniaxial compressive failure from:

$$p_1 = \frac{\sigma_c}{3}, \tag{6.3}$$

and K is the bulk unloading modulus computed from:

$$K = \frac{E_s}{3(1-2\nu)}, \tag{6.4}$$

where E_s is one-half the input tangent modulus for concrete and ν is the Poisson's ratio.

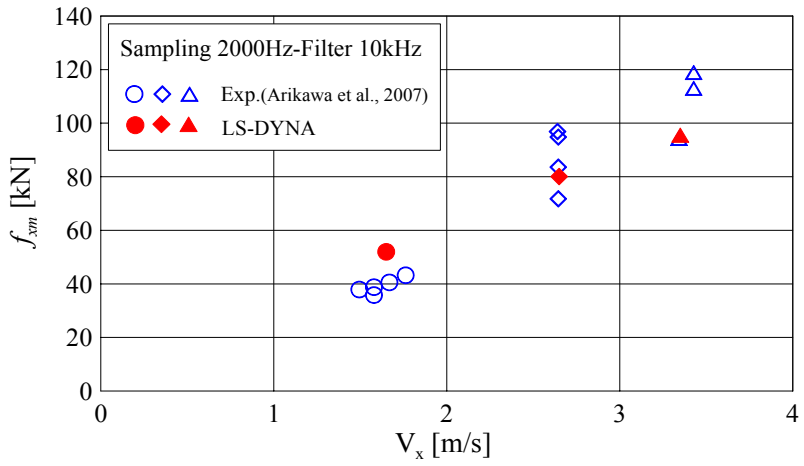

Fig. 6.3 Maximum resultant forces by the laboratory and numerical experiments as varying collision velocities

Photo 6.2 Concrete wall after collision in the laboratory experiment for 100cm in initial height (Arikawa et al., 2007)

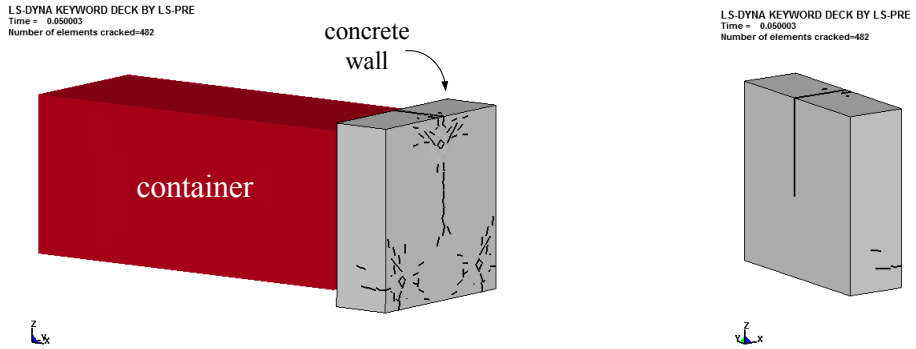

(a) Rear view of the concrete wall (b) Front view of the concrete wall

Fig. 6.4 Concrete wall after collision in the numerical experiment for 100cm in initial height

As mentioned above, the strain rate effects, controlling hourglass mode and specified concrete model were considered in the numerical simulations to reproduce the actual collision phenomenon. Three points at the hinder side of the concrete wall were fixed and their reaction forces were adopted as collision force identically with the laboratory experiments. Fig. 6.3 depicts the maximum resultant forces (f_{xm}) at the load cells behind the concrete wall in the laboratory experiments and at the three fixed points in the numerical ones as varying collision velocities (V_x) of the container just before collision. For the numerical analyses, V_x =1.65, 2.65 and 3.35m/s were employed from the figure, which correspond to free falling velocities of the containers initially placed at 50, 75 and 100cm height. In the figure, unfilled and filled symbols denote the experimental values by Arikawa et al. (2007) and numerical ones by this simulation, respectively. The experimental and numerical results were sampled with 2,000Hz and were filtered at 10kHz or less by Fast Fourier Transform (FFT) identically. From the figure, it is found that the values in the laboratory and numerical experiments represent the same degrees for each collision velocity on the whole.

The crack was occurred on the concrete wall in the laboratory experiment with 100cm in initial height only as shown in Photo 6.2. In the numerical simulation with identical condition to the experiment also, the crack was appeared as in Fig. 6.4.

From above comparison of results by the experiments and LS-DYNA scaled in 1/5, the applicability of LS-DYNA to large scale simulation was verified. Here, LS-DYNA is utilized for validity of applicability of the estimation formula for collision force of the drifted container by the run-up tsunami to actual field.

6.3 Applicability of Estimation Formula to Actual Field

In order to apply the estimation formula to the full-scale container collision accompanying large deformation, the estimation formula (Eq. 3.6) modified in Chapter 3 is reviewed once more. Then the applicability of the estimation formula to prototype conditions is verified through comparison with the numerical simulations (LS-DYNA) validated in above section, and simplification of the estimation formula is described.

6.3.1 *Revision of the modified estimation formula*

For the full-scale collision, large deformation of the container may occur due to relatively high stiffness of the collided body such as a concrete column. Because of different velocities at each nodes of the container due to its deformation, the velocity of the container at the moment of maximum collision force is not reached to zero. Furthermore, for the estimation of the full-scale collision force which mainly depends on the collision time, considering the collision time in presence of the wave to estimating the collision forces due to the container and the added mass by the wave is not reasonable. As an example, the estimated collision force in presence of the wave, in which the collision forces due to the container and the added mass were used identical collision times in presence of the wave, was less than the estimated collision force in absence of the wave, on the contrary. Hence, it is unsuitable to apply Eq. (3.6) in the actual phenomenon, in which the collision forces due to the container and the added mass are considered identical collision times. Thus, the author revises Eq. (3.6) in order to apply for the large deformation of the container. Eq. (3.6) is divided between the collision force (Eq. (6.5)) due to container using the parameters from the numerical simulations in absence of the wave and the collision force (Eq. (6.6)) due to run-up wave behind the container using the parameters from the numerical simulations in

presence of the wave, and then sum of them is adopted as final collision force (Eq. (6.7)).

$$\int_{t_{n1}}^{t_{n2}} f_{xn}(t)dt = m_c\left(V_{xi} - V_{xn}\right) \tag{6.5}$$

$$\int_{t_{w1}}^{t_{w2}} f_{xw}(t)dt = \left(\rho_w \eta B_c V_{xi} \Delta t_w\right)\left(V_{xi} - V_{xw}\right) \tag{6.6}$$

$$f_{xm} = f_{xnm} + f_{xwm} = \beta_n m_c \Delta V_{xn} / \Delta t_n + \beta_w \rho_w \eta B_c V_{xi} \Delta V_{xw} \tag{6.7}$$

where V_{xi} is the initial velocity; V_{xn} and V_{xw} are the velocities of the colliding container at the moment of the maximum collision force in absence and presence of the wave behind the container, respectively; ΔV_x is the velocity change during the collision time (Δt); and subscripts n and w indicate the values in absence of the wave behind the container and in presence of it, respectively. Therefore the numerical simulations were also conducted for both conditions, and the necessary parameters for the estimation formula are adopted. Then, applicability of the estimation formula revised here is verified through comparison of collision forces by the formula and the numerical simulation.

6.3.2 *Definition of collision force in actual phenomenon*

In the full-scale numerical simulations, it is important what kind of value is considered as the collision force. Generally, the dynamic equation of motion for the entire system can be treated as

$$F_I(t) + F_D(t) + F_S(t) = m\ddot{u} + c\dot{u} + ku = P(t) \tag{6.8}$$

where $F_I(t)$, $F_D(t)$ and $F_S(t)$ are the inertia resisting force, viscous damping force and impact resisting force, respectively; m represents the mass and moment of inertia matrix; and c and k are the damping and stiffness matrix for the one degree of freedom system while $P(t)$ represents the external load vector. $\ddot{u}$, $\dot{u}$ and u are the acceleration, velocity and displacement vectors, respectively. The "(t)" denotes the quantities at time t while a dot denotes a derivative with respect to time. The impact resisting force ($F_S(t)$) is the force that collided body itself resists a shock as strength,

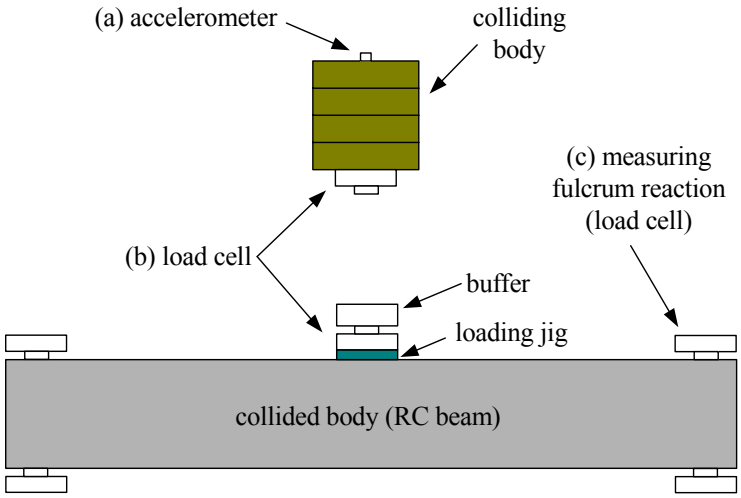

Fig. 6.5 Measuring methods of impact load (Saji et al., 1985)

i.e., the bending or shear strength of the object for static loading test as the resisting force depending on restituting force of collided body. From the point that the viscous damping force ($F_D(t)$) is extremely small compared with the inertia resisting force ($F_I(t)$) and impact resisting force ($F_S(t)$), Saji et al (1985) assumed $F_D(t)=0$ for impact experiments as shown in fig. 6.5 with a small mortar beam as a collided body. They defined that $F_S(t)$ is "impact bending strength" corresponding the static bending strength and the total impact resisting force ($F_I(t)+F_S(t)$) including the inertia resisting force is "impact bending proof strength." Besides Kishi (2004) described as follows:

"The measuring method by accelerometer or load cell in the figure for impact force means that is measuring the impact proof strength involving the inertia resisting force of collided body. Although the inertia resisting force is contained in the reaction force, generally prominent around impact point while a little at fulcrum. Hence the method measuring reaction at fulcrum means that is a measurement the resisting force standing for the deformation of collided body, i.e., corresponding measuring impact bending (or shear) strength. Except impacts with high speed, the bending or shear deformation plays an important role for an overall response of collided body. Therefore, it can be sad that considering the impact bending (or shear) strength in Fig. 6.5 (c) corresponds with conservation of energy for impact phenomena."

Besides Chopra (2007) divided the impact force between peak dynamic force (PDF) and equivalent static force (ESF). PDF is the largest impact force ($F_I(t)+F_D(t)+F_S(t)$) computed during the simulation and is not representative of the design structural demands that engineers need to consider because the structure has not had "time" to respond to the rapid change in loading. And ESF is the static force ($F_S(t)$) necessary to

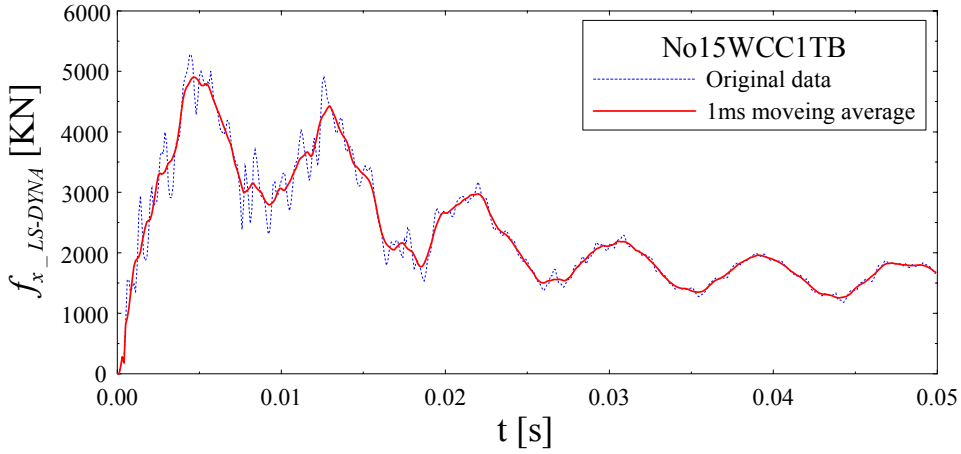

Fig. 6.6 Time variations of collision forces for original and smoothed date

produce the same deflection at the point of interest as produced by the dynamic event and is a function of the stiffness of the system and its dynamic characteristics. ESF is a more appropriate measure of the design structural demand because for structural design the computed element stresses are to be compared with allowable stresses that are specified based on static tests on materials, i.e., tests conducted at slow loading rates.

In LS-DYNA, there are the “rcforc” corresponding contact force at colliding nodes and the “spcforc” corresponding restraint force at restrained nodes (fulcrum reaction) of collided body. For calculating maximum collision force with the numerical collision simulations, hence, the “spcfore” corresponding the ESF is used as the collision force here after.

In treatment of impact problem, generally the high frequency components for fluctuation profiles of acceleration, load and deformation are eliminated for clear and simple analysis. The reason why this procedure is possible is that the averaged behavior of structure is not affected by the impulsive response. From this point of view, the author carried out the moving average (1ms) smoothing method for all of the numerical results in order to smoothing the fluctuation profile of the collision force and clearing the collision time. As an example, time variations of the original collision force (dot line) and smoothed one (solid line) are represented in Fig. 6.6, and it is known that the collision times and maximum collision forces show the same degree between both results. In this full-scale drifting collision simulation, the moving averaged “spcforc” with 1ms is used as the collision force.

6.3.3 *Comparison of collision forces by collision model and revised estimation formula*

At first, the numerical experiments for the collision simulation of drifted container are carried out in full-scale, and then the comparison between maximum collision forces of the drifted container by the estimation formula revised above and the numerical experiments is implemented. For the numerical analysis, the collision model utilizing LS-DYNA employs the results of the container drifting simulation as the initial conditions in the same manner with the small scaled model simulations in Chapter 5. The drifting velocity (V_x) of the container just before collision and run-up wave level (η) behind the container (Table 5.6) in the drifting simulations scaled in 1/75 are converted into the full-scaled values based on the Froude similarity law as shown in Table 6.3, in which Cases 1 and 2 in Table 5.3 are considered as the wave condition. The actual size of an ISO 40ft and 20ft freight container models (Japanese industrial standards committee, 1994) used in the full-scale simulations as colliding bodies are illustrated in Fig. 6.7 and their internal frame works are shown in Fig. 6.8. Empty, half- and full-loaded containers are considered, in which 3.384, 16.932 and 30.480 t_f for 40ft container and 1.921, 11.121 and 20.321 t_f for 20ft container are used, respectively. For simplification of simulations, variation of the weights is controlled by change of container's density. Besides, back-yard structures as collided bodies are employed as follows: a column of tsunami refuge terrace at Okushiri town, Hokkaido; a pier of coastal road; a light tower in container terminal; and two posts of tsunami screen at

Table 6.3 Initial conditions in full-scale collision simulations

T_i [s]	H_i [cm]	H_a [m]	Class	Direction	Weight	η [m]	V_x [m/s]	Test No.
10.5	4.0	3.7	40ft	Lateral	Empty	0.525	4.252	1
					Half	1.050	2.399	2
					Full	1.350	1.455	3
				Longitudinal	Empty	1.050	1.195	4
			20ft	Lateral	Empty	0.600	3.828	7
					Half	1.200	1.568	8
					Full	1.350	0.296	9
				Longitudinal	Empty	0.825	1.957	10
	9.0	7.8	40ft	Lateral	Empty	0.675	12.272	13
					Half	1.125	10.306	14
					Full	1.500	9.119	15
				Longitudinal	Half	2.475	5.716	16
			20ft	Lateral	Half	1.350	9.093	17

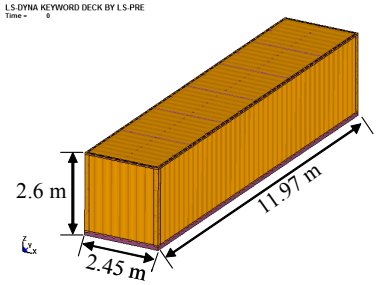

(a) 40ft container

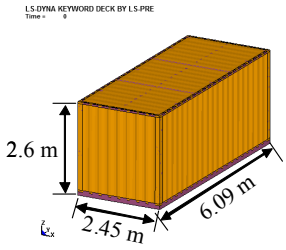

(b) 20ft container

Fig. 6.7 Modeling of ISO freight containers

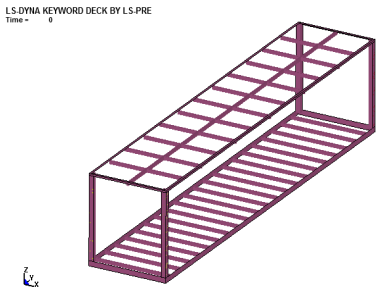

(a) 40ft container

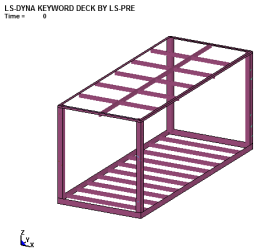

(b) 20ft container

Fig. 6.8 Frame works of full-scale containers

(a) Tsunami refuge terrace at Okushri town
Source: http://www.town.okushiri.lg.jp

(b) Pier of coastal road
Source: Nagoya port terminal public corporation

(c) Light tower in container terminal
Source: Nagoya port terminal public corporation

(d) Tsunami screen at Kushiro region
Source: Maruyama et al. 2008

Photo 6.3 Back-yard structures as collided body employed in full-scale simulation

Table 6.4 Dimensions and material of the models used in full-scale simulations

Model	Dimensions [m]					Fix	Element	Material
	Length	Width	Height	Diameter	Thickness			
40ft container	11.97	2.45	2.60	-	0.0016 ~ 0.0045	-	Shell	Steel
20ft container	6.09	2.45	2.60	-	0.0016 ~ 0.0045	-	Shell	Steel
Concrete column	-	-	4.00	1.0 or 2.0	-	Bottom or Top & Bottom	Solid	Concrete
Squared concrete column	1.0 or 2.0	1.0 or 2.0	4.00	-	-	Top & Bottom	Solid	Concrete
Steel column	-	-	4.00	1.0	0.002	Bottom	Shell	Steel
Tsunami screen@2	-	-	4.00	0.5	0.001	Bottom	Shell	Steel

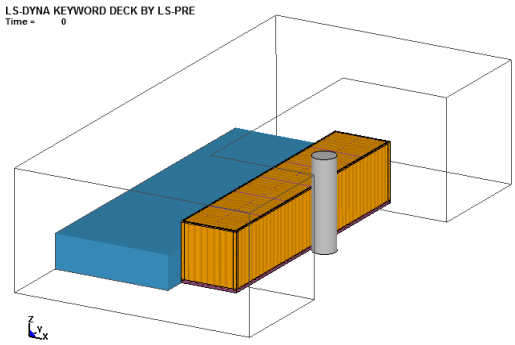

(a) Concrete column in diameter 1.0m

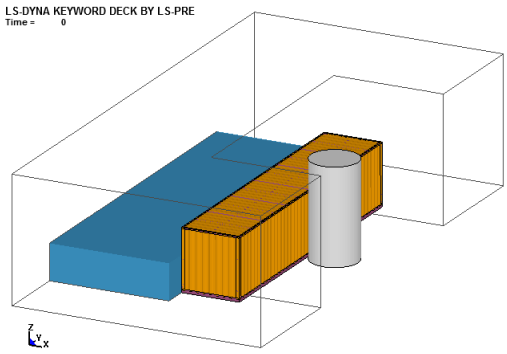

(b) Concrete column in diameter 2.0m

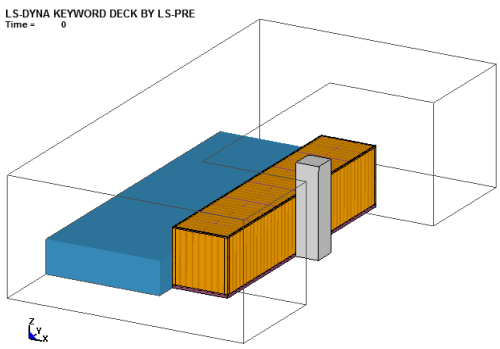

(c) Squared concrete column in width 1.0m

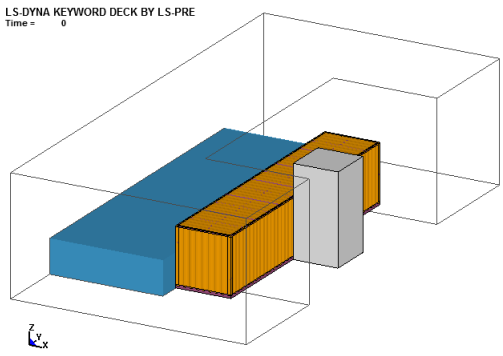

(d) Squared concrete column in width 2.0m

Fig. 6.9 Representative geometries of the full-scale collision simulations

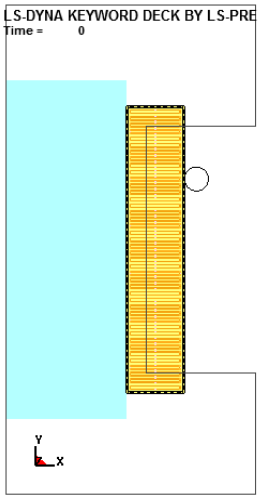

(e) Eccentric collision #1 with concrete column

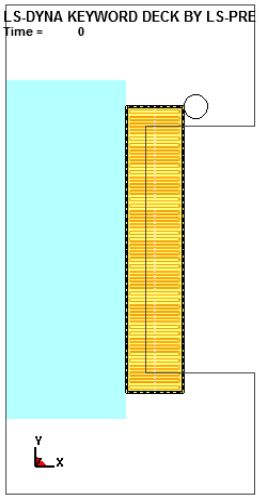

(f) Eccentric collision #2 with concrete column

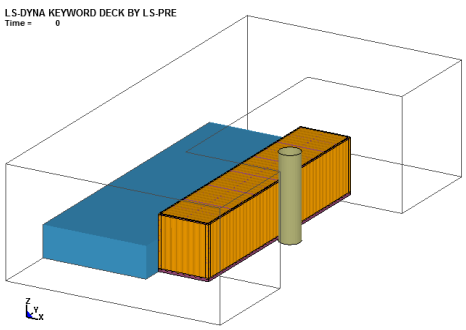

(g) Steel column

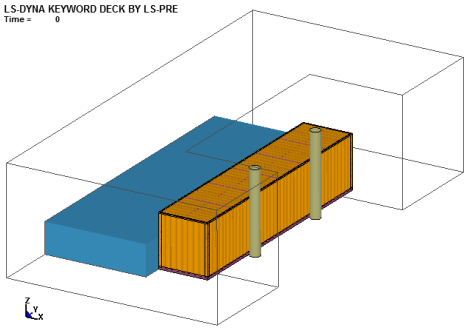

(h) Tsunami screen@2

Fig. 6.9 Continued

Kushiro region, Hokkaido (Photo 6.3). In addition, dimensions, fixed part and material of the full-scale container and collided bodies are listed in Table 6.4. For the physical properties of material, the steel and concrete referred to the container and concrete wall models in the 1/5 scale simulation described above. For fluid-structure interaction (FSI) analysis in the full-scale simulation, the author adopted the ALE method in the same manner as the model simulation in Chapter 5. The representative geometries of the full-scale collision simulation (LS-DYNA) using results of the drifting simulation (Table 6.3) are illustrated in Fig. 6.9.

The initial conditions and running names are listed in Tables 6.5 - 6.9. To simplify referral to the various runs conducted, each run is referred to by unique descriptive name. For example, for the drifting test no. 1 considering behind wave with concrete column in diameter 1.0m fixed at top and bottom parts, the run notation would be No1WCC1TB. The applicability of the estimation formula for drifting collision force of container to actual field is verified by using these structures selected here as the collided bodies.

Table 6.5 Initial conditions and running names for concrete column in diameter 1.0m

Collided body	Fix	H_a [cm]	Class	Direction	Weight	[m]	V_{xi} [m/s]	Run	
								Non-water	Water
Concrete Column (D=1.0m)	Bottom	3.74	40ft	Lateral	Empty	0.525	4.252	No1NCC1B	No1WCC1B
					Half	1.050	2.399	No2NCC1B	No2WCC1B
					Full	1.350	1.455	No3NCC1B	No3WCC1B
				Longitudinal	Empty	1.050	1.195	No4NCC1B	No4WCC1B
			20ft	Lateral	Empty	0.600	3.828	No7NCC1B	No7WCC1B
					Half	1.200	1.568	No8NCC1B	No8WCC1B
					Full	1.350	0.296	No9NCC1B	No9WCC1B
				Longitudinal	Empty	0.825	1.957	No10NCC1B	No10WCC1B
		7.82	40ft	Lateral	Empty	0.675	12.272	No13NCC1B	No13WCC1B
					Half	1.125	10.306	No14NCC1B	No14WCC1B
					Full	1.500	9.119	No15NCC1B	No15WCC1B
				Longitudinal	Half	2.475	5.716	No16NCC1B	No16WCC1B
			20ft	Lateral	Half	1.350	9.093	No17NCC1B	No17WCC1B
	Top & Bottom	3.74	40ft	Lateral	Empty	0.525	4.252	No1NCC1TB	No1WCC1TB
					Half	1.050	2.399	No2NCC1TB	No2WCC1TB
					Full	1.350	1.455	No3NCC1TB	No3WCC1TB
				Longitudinal	Empty	1.050	1.195	No4NCC1TB	No4WCC1TB
			20ft	Lateral	Empty	0.600	3.828	No7NCC1TB	No7WCC1TB
					Half	1.200	1.568	No8NCC1TB	No8WCC1TB
					Full	1.350	0.296	No9NCC1TB	No9WCC1TB
				Longitudinal	Empty	0.825	1.957	No10NCC1TB	No10WCC1TB
		7.82	40ft	Lateral	Empty	0.675	12.272	No13NCC1TB	No13WCC1TB
					Half	1.125	10.306	No14NCC1TB	No14WCC1TB
					Full	1.500	9.119	No15NCC1TB	No15WCC1TB
				Longitudinal	Half	2.475	5.716	No16NCC1TB	No16WCC1TB
			20ft	Lateral	Half	1.350	9.093	No17NCC1TB	No17WCC1TB

Table 6.6 Initial conditions and running names for concrete column in diameter 2.0m

Collided body	Fix	H_a [cm]	Class	Direction	Weight	[m]	V_{xi} [m/s]	Run	
								Non-water	Water
Concrete Column (D=2.0m)	Bottom	3.74	40ft	Lateral	Empty	0.525	4.252	No1NCC2B	No1WCC2B
					Half	1.050	2.399	No2NCC2B	No2WCC2B
					Full	1.350	1.455	No3NCC2B	No3WCC2B
				Longitudinal	Empty	1.050	1.195	No4NCC2B	No4WCC2B
			20ft	Lateral	Empty	0.600	3.828	No7NCC2B	No7WCC2B
					Half	1.200	1.568	No8NCC2B	No8WCC2B
					Full	1.350	0.296	No9NCC2B	No9WCC2B
				Longitudinal	Empty	0.825	1.957	No10NCC2B	No10WCC2B
		7.82	40ft	Lateral	Empty	0.675	12.272	No13NCC2B	No13WCC2B
					Half	1.125	10.306	No14NCC2B	No14WCC2B
					Full	1.500	9.119	No15NCC2B	No15WCC2B
				Longitudinal	Half	2.475	5.716	No16NCC2B	No16WCC2B
			20ft	Lateral	Half	1.350	9.093	No17NCC2B	No17WCC2B
	Top & Bottom	3.74	40ft	Lateral	Empty	0.525	4.252	No1NCC2TB	No1WCC2TB
					Half	1.050	2.399	No2NCC2TB	No2WCC2TB
					Full	1.350	1.455	No3NCC2TB	No3WCC2TB
				Longitudinal	Empty	1.050	1.195	No4NCC2TB	No4WCC2TB
			20ft	Lateral	Empty	0.600	3.828	No7NCC2TB	No7WCC2TB
					Half	1.200	1.568	No8NCC2TB	No8WCC2TB
					Full	1.350	0.296	No9NCC2TB	No9WCC2TB
				Longitudinal	Empty	0.825	1.957	No10NCC2TB	No10WCC2TB
		7.82	40ft	Lateral	Empty	0.675	12.272	No13NCC2TB	No13WCC2TB
					Half	1.125	10.306	No14NCC2TB	No14WCC2TB
					Full	1.500	9.119	No15NCC2TB	No15WCC2TB
				Longitudinal	Half	2.475	5.716	No16NCC2TB	No16WCC2TB
			20ft	Lateral	Half	1.350	9.093	No17NCC2TB	No17WCC2TB

Table 6.7 Initial conditions and running names for squared concrete column

Collided body	Fix	H_a [cm]	Class	Direction	Weight	[m]	V_{xi} [m/s]	Run	
								Non-water	Water
Squared Concrete Column (D=1.0m)	Top & Bottom	3.74	40ft	Lateral	Empty	0.525	4.252	No1NSCC1B	No1WSCC1B
					Half	1.050	2.399	No2NSCC1B	No2WSCC1B
					Full	1.350	1.455	No3NSCC1B	No3WSCC1B
				Longitudinal	Empty	1.050	1.195	No4NSCC1B	No4WSCC1B
			20ft	Lateral	Empty	0.600	3.828	No7NSCC1B	No7WSCC1B
					Half	1.200	1.568	No8NSCC1B	No8WSCC1B
					Full	1.350	0.296	No9NSCC1B	No9WSCC1B
				Longitudinal	Empty	0.825	1.957	No10NSCC1B	No10WSCC1B
		7.82	40ft	Lateral	Empty	0.675	12.272	No13NSCC1B	No13WSCC1B
					Half	1.125	10.306	No14NSCC1B	No14WSCC1B
					Full	1.500	9.119	No15NSCC1B	No15WSCC1B
				Longitudinal	Half	2.475	5.716	No16NSCC1B	No16WSCC1B
			20ft	Lateral	Half	1.350	9.093	No17NSCC1B	No17WSCC1B
Squared Concrete Column (D=2.0m)	Top & Bottom	3.74	40ft	Lateral	Empty	0.525	4.252	No1NSCC2B	No1WSCC2B
					Half	1.050	2.399	No2NSCC2B	No2WSCC2B
					Full	1.350	1.455	No3NSCC2B	No3WSCC2B
				Longitudinal	Empty	1.050	1.195	No4NSCC2B	No4WSCC2B
			20ft	Lateral	Empty	0.600	3.828	No7NSCC2B	No7WSCC2B
					Half	1.200	1.568	No8NSCC2B	No8WSCC2B
					Full	1.350	0.296	No9NSCC2B	No9WSCC2B
				Longitudinal	Empty	0.825	1.957	No10NSCC2B	No10WSCC2B
		7.82	40ft	Lateral	Empty	0.675	12.272	No13NSCC2B	No13WSCC2B
					Half	1.125	10.306	No14NSCC2B	No14WSCC2B
					Full	1.500	9.119	No15NSCC2B	No15WSCC2B
				Longitudinal	Half	2.475	5.716	No16NSCC2B	No16WSCC2B
			20ft	Lateral	Half	1.350	9.093	No17NSCC2B	No17WSCC2B

Table 6.8 Initial conditions and running names for eccentric collisions

Collided body	Fix	H_a [cm]	Class	Direction	Weight	[m]	V_{xi} [m/s]	Run	
								Non-water	Water
Concrete Column (D=1.0m) Eccentricity1	Top & Bottom	3.74	40ft	Lateral	Empty	0.525	4.252	No1NSCC1BE1	No1WSCC1BE1
					Half	1.050	2.399	No2NSCC1BE1	No2WSCC1BE1
					Full	1.350	1.455	No3NSCC1BE1	No3WSCC1BE1
			20ft	Lateral	Empty	0.600	3.828	No7NSCC1BE1	No7WSCC1BE1
					Half	1.200	1.568	No8NSCC1BE1	No8WSCC1BE1
					Full	1.350	0.296	No9NSCC1BE1	No9WSCC1BE1
		7.82	40ft	Lateral	Empty	0.675	12.272	No13NSCC1BE1	No13WSCC1BE1
					Half	1.125	10.306	No14NSCC1BE1	No14WSCC1BE1
					Full	1.500	9.119	No15NSCC1BE1	No15WSCC1BE1
			20ft	Lateral	Half	1.350	9.093	No17NSCC1BE1	No17WSCC1BE1
Concrete Column (D=1.0m) Eccentricity2	Top & Bottom	3.74	40ft	Lateral	Empty	0.525	4.252	No1NSCC1BE2	No1WSCC1BE2
					Half	1.050	2.399	No2NSCC1BE2	No2WSCC1BE2
					Full	1.350	1.455	No3NSCC1BE2	No3WSCC1BE2
			20ft	Lateral	Empty	0.600	3.828	No7NSCC1BE2	No7WSCC1BE2
					Half	1.200	1.568	No8NSCC1BE2	No8WSCC1BE2
					Full	1.350	0.296	No9NSCC1BE2	No9WSCC1BE2
		7.82	40ft	Lateral	Empty	0.675	12.272	No13NSCC1BE2	No13WSCC1BE2
					Half	1.125	10.306	No14NSCC1BE2	No14WSCC1BE2
					Full	1.500	9.119	No15NSCC1BE2	No15WSCC1BE2
			20ft	Lateral	Half	1.350	9.093	No17NSCC1BE2	No17WSCC1BE2

Table 6.9 Initial conditions and running names for steel column and tsunami screen@2

Collided body	Fix	H_a [cm]	Class	Direction	Weight	[m]	V_{xi} [m/s]	Run	
								Non-water	Water
Steel Column (D=1.0m, t=2cm)	Bottom	3.74	40ft	Lateral	Empty	0.525	4.252	No1NSC1B	No1WSC1B
					Half	1.050	2.399	No2NSC1B	No2WSC1B
					Full	1.350	1.455	No3NSC1B	No3WSC1B
				Longitudinal	Empty	1.050	1.195	No4NSC1B	No4WSC1B
			20ft	Lateral	Empty	0.600	3.828	No7NSC1B	No7WSC1B
					Half	1.200	1.568	No8NSC1B	No8WSC1B
					Full	1.350	0.296	No9NSC1B	No9WSC1B
				Longitudinal	Empty	0.825	1.957	No10NSC1B	No10WSC1B
		7.82	40ft	Lateral	Empty	0.675	12.272	No13NSC1B	No13WSC1B
					Half	1.125	10.306	No14NSC1B	No14WSC1B
					Full	1.500	9.119	No15NSC1B	No15WSC1B
				Longitudinal	Half	2.475	5.716	No16NSC1B	No16WSC1B
			20ft	Lateral	Half	1.350	9.093	No17NSC1B	No17WSC1B
Tsunami Screen (D=0.5m, t=1cm)@2	Bottom	3.74	40ft	Lateral	Empty	0.525	4.252	No1NTS0.5B@2	No1WTS0.5B@2
					Half	1.050	2.399	No2NTS0.5B@2	No2WTS0.5B@2
					Full	1.350	1.455	No3NTS0.5B@2	No3WTS0.5B@2
			20ft	Lateral	Empty	0.600	3.828	No7NTS0.5B@2	No7WTS0.5B@2
					Half	1.200	1.568	No8NTS0.5B@2	No8WTS0.5B@2
					Full	1.350	0.296	No9NTS0.5B@2	No9WTS0.5B@2
		7.82	40ft	Lateral	Empty	0.675	12.272	No13NTS0.5B@2	No13WTS0.5B@2
					Half	1.125	10.306	No14NTS0.5B@2	No14WTS0.5B@2
					Full	1.500	9.119	No15NTS0.5B@2	No15WTS0.5B@2
			20ft	Lateral	Half	1.350	9.093	No17NTS0.5B@2	No17WTS0.5B@2

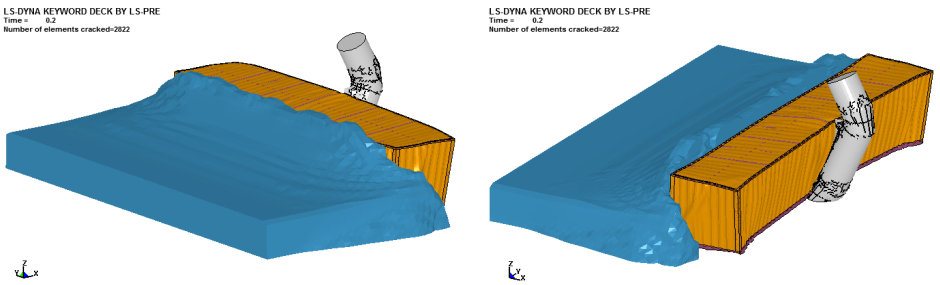

(a) Rear view (b) Front view

Fig. 6.10 Representative images of drifting collision in full-scale for WCC1B

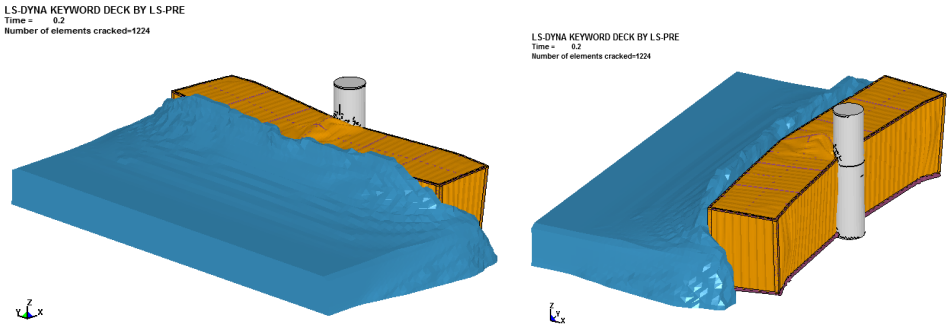

(a) Rear view (b) Front view

Fig. 6.11 Representative images of drifting collision in full-scale for WCC1TB

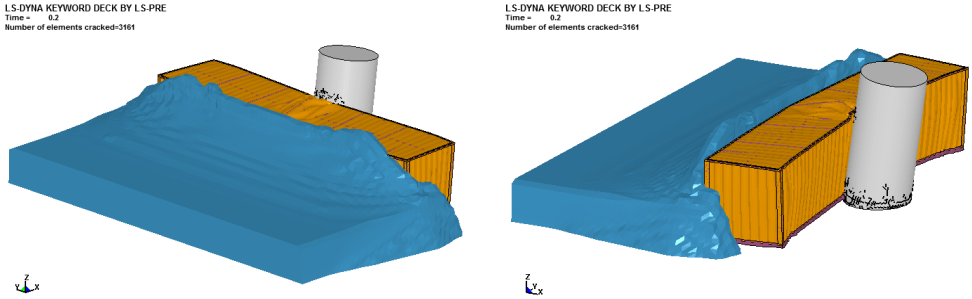

(a) Rear view (b) Front view

Fig. 6.12 Representative images of drifting collision in full-scale for WCC2B

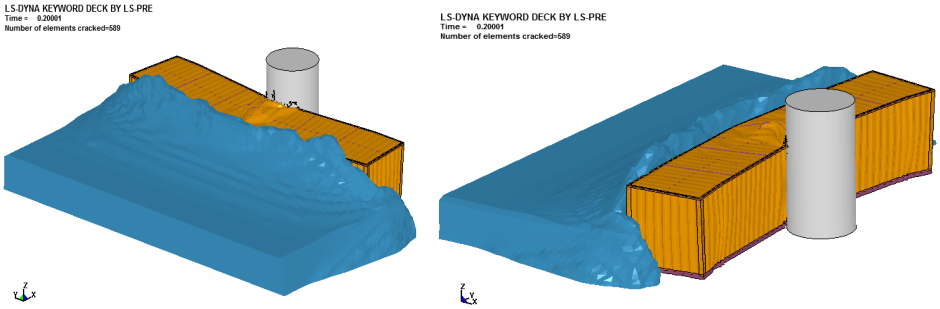

(a) Rear view (b) Front view

Fig. 6.13 Representative images of drifting collision in full-scale for WCC2TB

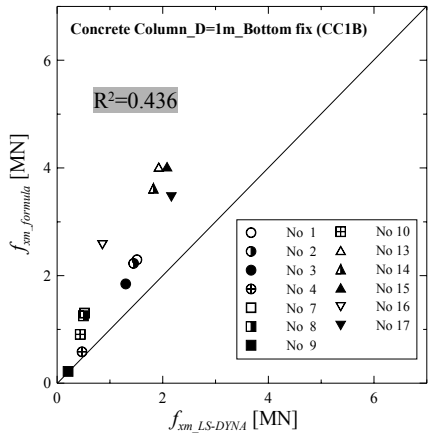

Fig. 6.14 Comparison between the numerical experiment and estimation formula (Eq. 6.6) for CC1B

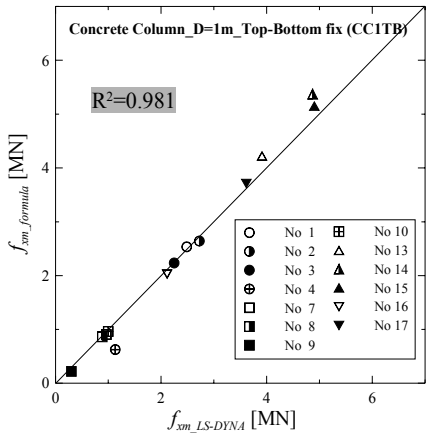

Fig. 6.15 Comparison between the numerical experiment and estimation formula (Eq. 6.6) for CC1TB

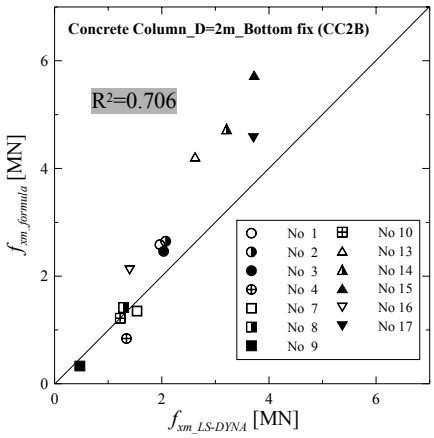

Fig. 6.16 Comparison between the numerical experiment and estimation formula (Eq. 6.6) for CC2B

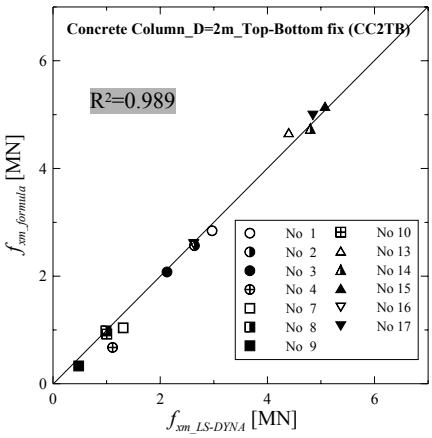

Fig. 6.17 Comparison between the numerical experiment and estimation formula (Eq. 6.6) for CC2TB

As mentioned above, numerical simulations were conducted in two phases; First the simulation in absence of wave behind container is implemented to obtain parameters for estimating collision force due to the container in the estimation formula and then the simulation in presence of wave is performed to obtain parameters for estimating collision force due to the wave in the formula.

Figs. 6.10 - 6.13 illustrate the representative images of drifting collision in the full-scale with concrete column, and indicate the cases of in diameter 1m fixed at bottom and top & bottom and in diameter 2m fixed at bottom and top & bottom, respectively. From the figures, it is found that the upward run-up wave behind the container and the wave passing through the container sides, and therefore it is concluded that the interaction between container and wave was accomplished well. Large deformation of

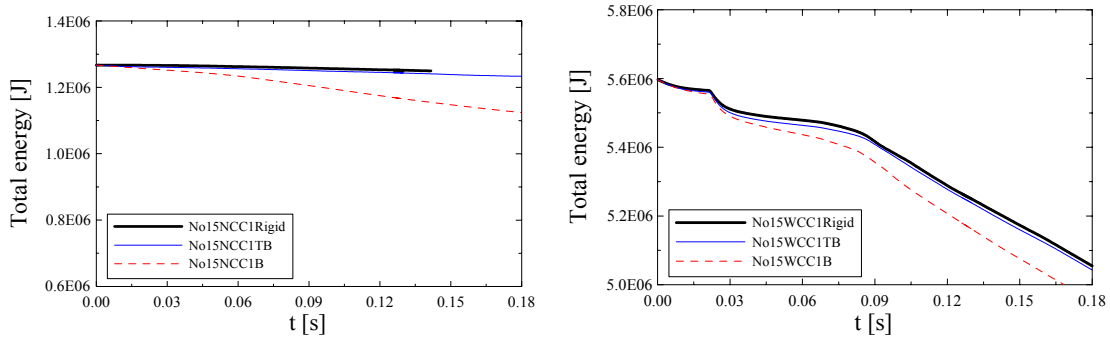

(a) Non-considering wave (b) Considering wave

Fig. 6.18 Time variations of total energy as changing collided body

the container is found in the figures. It caused the discordance of velocity between components of container, and is necessary this modification of the estimation formula in this chapter. The bottom fixed concrete columns (Figs. 6.10 and 6.12) seem to be collapsing while the top & bottom fixed concrete columns (Figs. 6.11 and 6.13) are not deformed nearly with some crack.

The comparisons of maximum collision forces by the numerical simulation and estimation formula (Eq. 6.7) are shown in Figs. 6.14 - 6.17. Horizontal and vertical axes indicate the collision forces by the numerical simulation in considering the wave behind container and the estimation formula using parameters obtained from the numerical simulations which are divided two phases, non-considering wave and considering wave, respectively. Symbols in the figures mean the wave and container conditions. For details, see Tables 6.5 - 6.9. Besides, the author represents coefficient of determination (R^2) in each comparison to confirm agreement between both results. From the figures, it is known that results of the estimation formula are in good agreement with the numerical ones for collision with the top & bottom fixed concrete columns (Figs. 6.15 and 6.17) while the bottom fixed concrete columns (Figs. 6.14 and 6.16) are not coincide.

To understand mechanism of this disagreement, the author investigates on energy loss of the models. Fig. 6.18 (a) shows time variation of total energy of the representative case (No15) in absence of wave and varied collided body, in which the bold line is the rigid column; the fine line is the top & bottom fixed concrete column; and dashed line is the bottom fixed concrete column. For considering rigid column (bold line) which is not occur any deformation, it shows little energy loss on total energy in spite of large deformation of container, and the author regarded that the energy loss due to deformation of container is negligible within the range of this full-scale simulation. For top & bottom fixed concrete column (fine line), although a little energy loss is found due to occurrence of some crack, it is small related with that of the bottom fixed

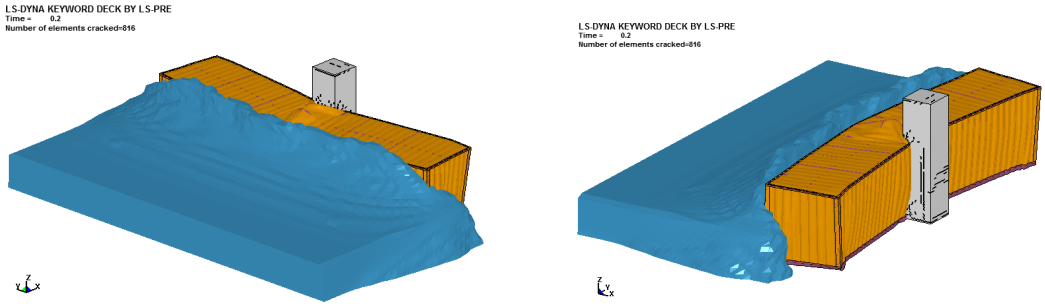

(a) Rear view (b) Front view

Fig. 6.19 Representative images of drifting collision in full-scale for WSCC1TB

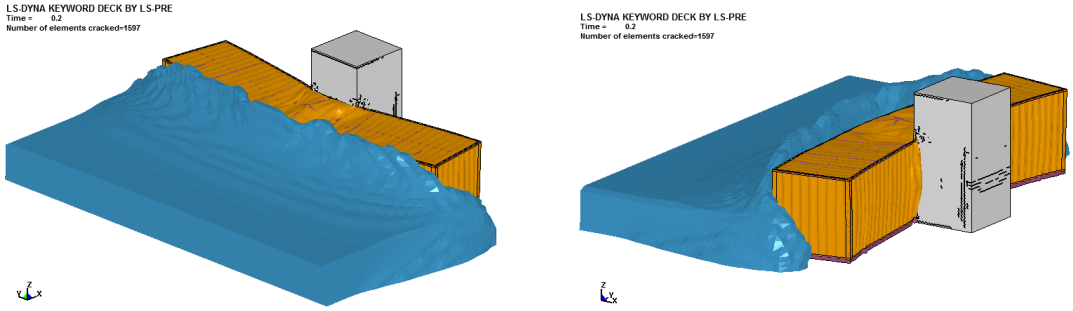

(a) Rear view (b) Front view

Fig. 6.20 Representative images of drifting collision in full-scale for WSCC2TB

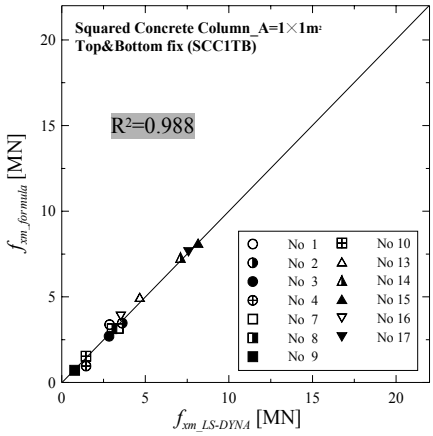

Fig. 6.21 Comparison between the numerical experiment and estimation formula (Eq. 6.6) for SCC1TB

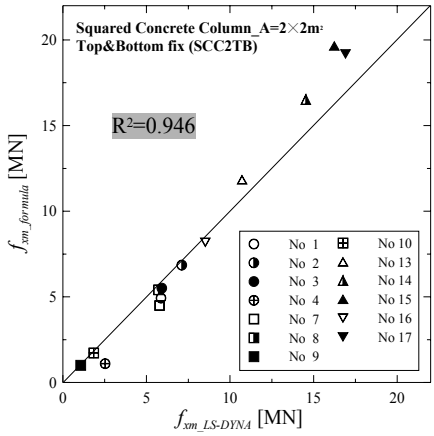

Fig. 6.22 Comparison between the numerical experiment and estimation formula (Eq. 6.6) for SCC2TB

concrete column. Steep total energy loss is found in the bottom fixed concrete and it can be explained using Figs. 6.10 and 6.12. In case of the bottom fixed concrete column, internal energy (within elastic domain) of the column transforms into kinetic energy (plastic domain) due to the small stiffness related with the colliding one. Because of this energy loss due to large deformation of collided body, the collision force (restraint

force) was decreased. Fig. 6.18 (b) considering wave shows a similar tendency with Fig. 6.18 (a) except effect of moving wave behind container in total energy.

As the results, the collision force is decreased for the bottom fixed concrete column as collided body due to large deformation of concrete column. Because this estimation formula is not considering the effect by deformation of collided body, the application to the collision with the bottom fixed concrete column occurred large deformation is not suitable. For following collision with concrete column, the top & bottom fixed restraint condition is considered only.

The representative images and comparisons of collision force by the numerical simulation and estimation formula (Eq. 6.7) for collisions with top & bottom fixed squared concrete column in diameter $1\times1m^2$ and $2\times2m^2$ are shown in Figs. 6.19 - 6.22. For these collisions also, the maximum collision forces by the estimation formula are in accordance with the results by the numerical simulation as shown in Figs. 6.21 and 6.22. It could not found distinct difference between the concrete column (WCC1TB and WCC2TB) and squared concrete column (WSCC1TB and WSCC2TB) in the representative collision image (Figs. 6.11, 6.13, 6.19 and 6.20) while the maximum collision force represents different tendency. The maximum collision forces for CC1TB and CC2TB (Figs. 6.15 and 6.17) are shown in same degree due to having circular cross sections making nearly constant contact area while SCC2TB occurs about double then CC1TB due to doubled contact area. Further the maximum collision force for SCC (squared concrete column) larger then that for CC (concrete column) on the whole. Consequently collision force may be increased in proportion to contact area.

Figs. 6.23 and 6.24 show the representative images of collision simulations for eccentric collisions, in which the concrete column is positioned between center and corner (WCC1TBE1) and at corner (WCC1TBE2) of container. As changing eccentricity, the destruction modes of the container and concrete column and the shapes of run-up wave behind the container are different. The comparisons of maximum collision forces by the numerical simulation and estimation formula (Eq. 6.7) are shown in Figs. 6.25 and 6.26 and it can be found a good agreement.

The representative images of drifting collision with steel column in diameter 1m fixed at bottom and two posts of tsunami screen in diameter 0.5m fixed at bottom except wire rope between posts are illustrated in Figs. 6.27 and 6.28, and it can be found a good interaction between the container and behind wave. The maximum collision forces by the numerical simulation and estimation formula (Eq. 6.7) are represented in Figs. 6.29 and 6.30. Exceptionally the collision force by the estimation formula underestimates for No. 13 in Fig. 6.30 because of decrement of collision velocity change due to

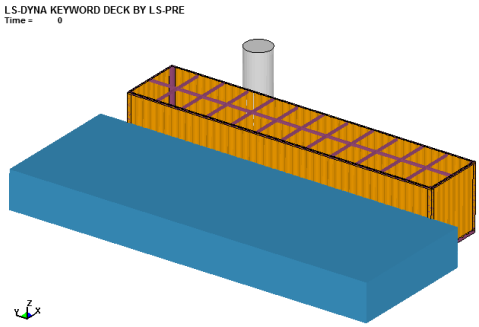

(a) Frame work of the upper part

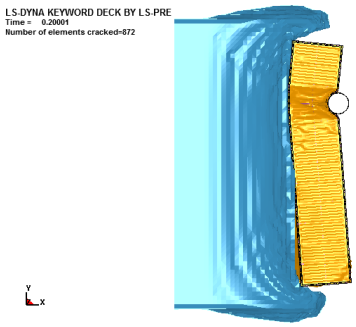

(b) Top view

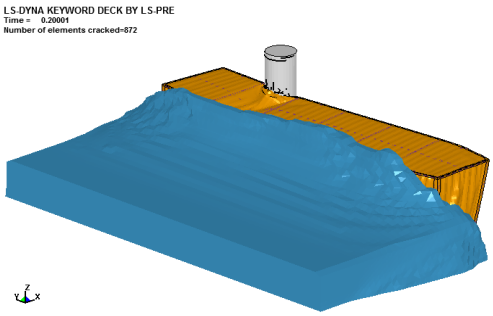

(c) Rear view

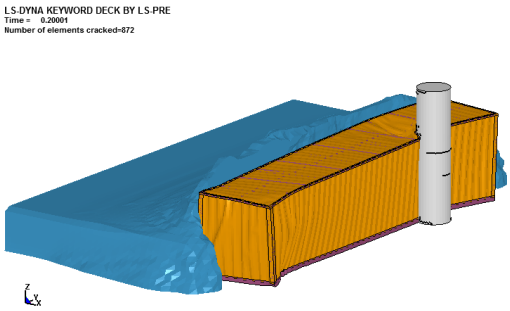

(d) Front view

Fig. 6.23 Representative images of drifting collision in full-scale for WCC1TBE1

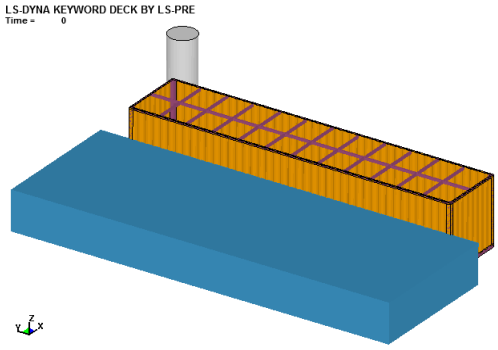

(a) Frame work of the upper part

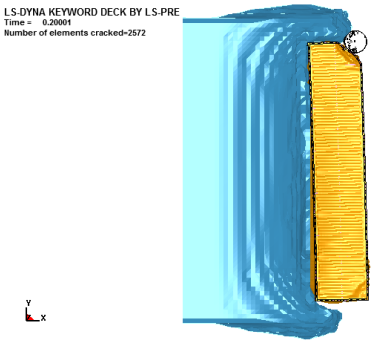

(b) Top view

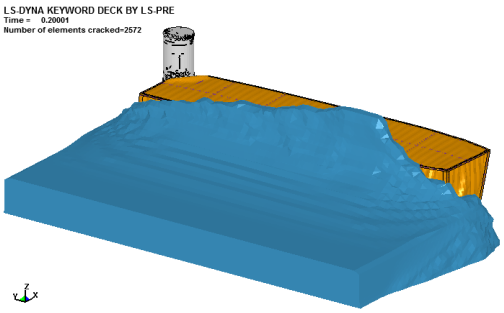

(c) Rear view

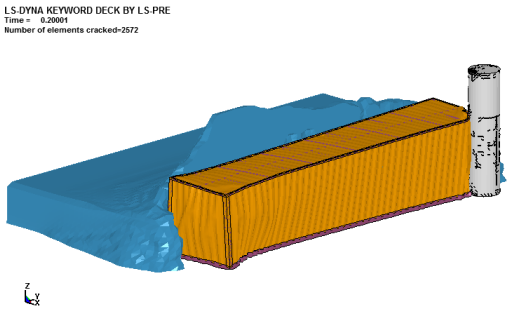

(d) Front view

Fig. 6.24 Representative images of drifting collision in full-scale for WCC1TBE2

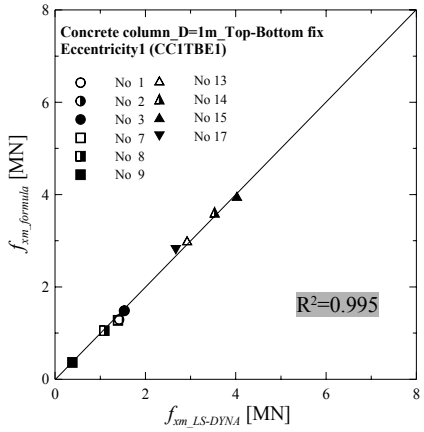

Fig. 6.25 Comparison between the numerical experiment and estimation formula (Eq. 6.6) for CC1TBE1

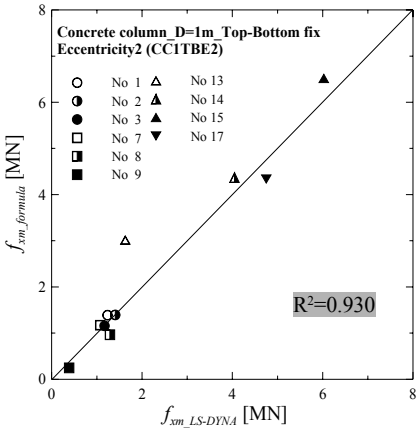

Fig. 6.26 Comparison between the numerical experiment and estimation formula (Eq. 6.6) for CC1TBE2

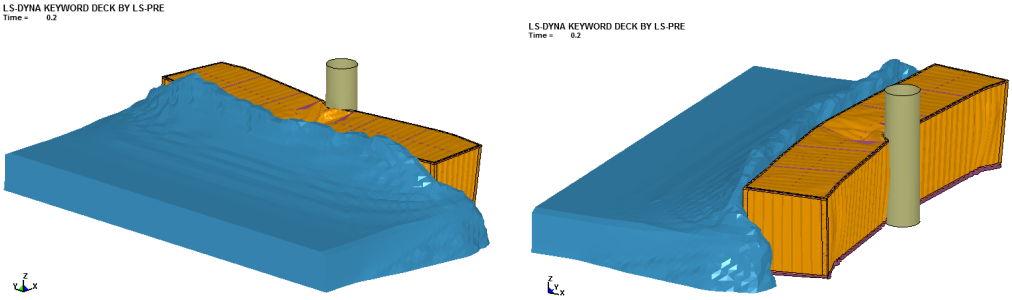

(a) Rear view (b) Front view

Fig. 6.27 Representative images of drifting collision in full-scale for SC1B

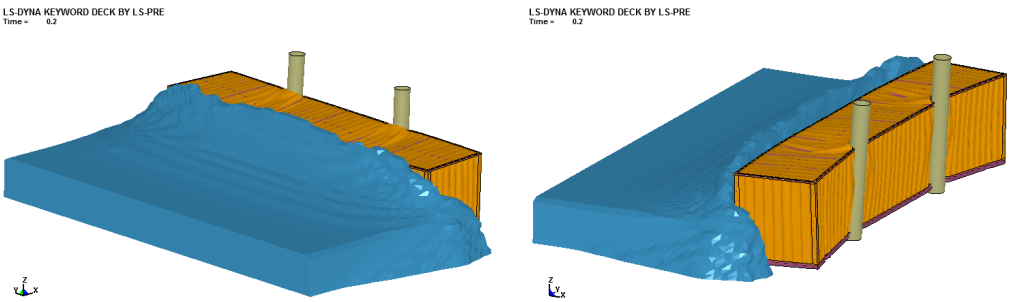

(a) Rear view (b) Front view

Fig. 6.28 Representative images of drifting collision in full-scale for TS0.5B@2

relationship of plastic deformation of the container and collision force. The maximum collision forces by the estimation formula predict the results by the numerical simulations on the whole, in which decrement of the collision force is not occurred in spite of bottom fix because of high stiffness of the steel itself.

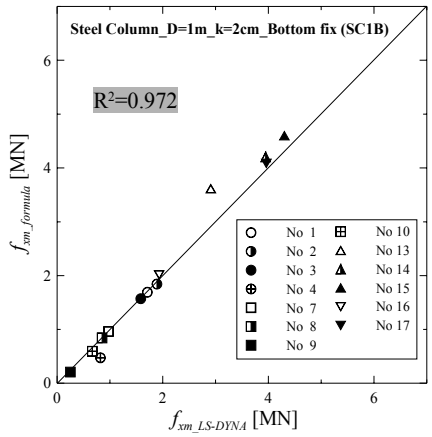

Fig. 6.29 Comparison between the numerical experiment and estimation formula (Eq. 6.6) for SC1B

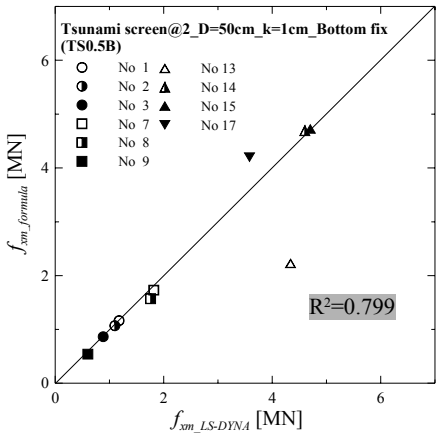

Fig. 6.30 Comparison between the numerical experiment and estimation formula (Eq. 6.6) for TS0.5B@2

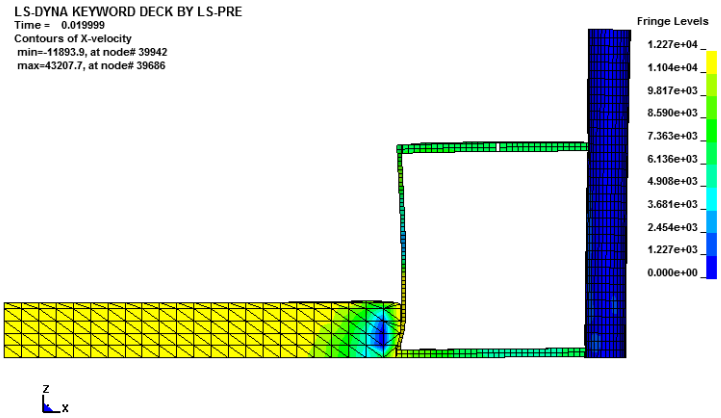

Fig. 6.31 Distribution of fluid velocity behind the drifted container at the moment of maximum collision force for No13WTS0.5B@2

Additionally, representative distribution of the fluid velocity behind the drifted container at the moment of maximum collision force for No13WTS0.5B@2, which case have relatively long collision time in the full-scale simulations, is shown in Fig. 6.31, and it is known that the range of the behind wave considered in the full-scale simulations was suitable from the point in deceleration of the fluid just behind container only.

Through comparisons of the maximum collision forces by the numerical simulation in the full-scale and estimation formula (Eq. 6.7), the applicability of the estimation formula to actual field is confirmed. However, this estimation formula (Eq. 6.7) requires many parameters so the simplification is performed in the next section.

Table 6.10 Selected constant integrated coefficients (β)

	CC1TB	CC2TB	SCC1TB	SCC2TB	CC1TBE1	CC1TBE2	SC1B	TS0.5B@2
H_a=3.74m	1.8	2.1	1.7	2.0	2.3	2.0	1.8	1.5
H_a=7.82m	1.6	1.7	1.4	1.2	1.7	1.6	1.6	1.8

6.4 Simplification of Estimation Formula

The applicability of the estimation formula (Eq. 6.7) for collision force of drifted container to actual field, in which large deformation of the container is occurred, was verified. However, the form of this formulation requiring too many parameters ($\beta_n, \beta_w, \Delta V_{xn}, \Delta V_{xw}, \Delta t_n$) to estimate collision force is not adequate for practical using. Thus the author performs the simplification of the estimation formula to use easily.

First of all, the integration coefficients (β_n and β_w) obtained in the drifting collision simulation in above section are represented in Fig. 6.32. Horizontal and vertical axes denote the test numbers and integration coefficient, and β_n and β_w indicate the values in absence and presence of waves, respectively. From the figure, it is found that β_n and β_w represent almost same value for whole cases, therefore the author considers the β_n and β_w in one value (β). Besides the β is employed the same values according to the change of wave condition (No. 1 to 10 for H_a=3.74m and No. 13 to 17 for H_a=7.82m with same wave period) and collided body. The values were selected to predicting best the numerical results and are listed in Table 6.10. Further the comparisons of the collision forces by the estimation formula using constant integrated coefficient and the numerical simulation are shown in Fig. 6.33. Using Table 6.10, it enables to utilize the estimation formula more easily, furthermore users can consider β=2.0 on the most dangerous condition from Fig. 3.2 and Eq. 3.4. Then the estimation formula can be rewritten as Eq. 6.9, and the required parameters are as follows; $\beta, \Delta V_{xn}, \Delta V_{xw}$ and Δt_n.

$$\begin{aligned} f_{xm} &= \beta\left(m_c \Delta V_{xn} / \Delta t_n + \rho_w \eta B_c V_{xi} \Delta t_w \Delta V_{xw} / \Delta t_w\right) \\ &= \beta\left(m_c \Delta V_{xn} / \Delta t_n + \rho_w \eta B_c V_{xi} \Delta V_{xw}\right) \end{aligned} \quad . \tag{6.9}$$

This estimation formula is applied with the concepts which are $\Delta V_{xn} = V_{xi} - V_{xn}$ and $\Delta V_{xw} = V_{xi} - V_{xw}$, in where V_{xi} is the initial velocity; and V_{xn} and V_{xw} are the velocities of container at the moment of maximum collision force in absence and

presence of waves. Using virtual collision time $\Delta t_n'$ and $\Delta t_w'$ until stop ($V_{xn} = V_{xw} = 0$, $\Delta V_{xn} = \Delta V_{xw} = V_{xi}$) the container movement in progressing direction, Eq. (6.9) can be written as follow;

$$\begin{aligned} f_{xm} &= \beta\left(m_c V_{xi} / \Delta t_n' + \rho_w \eta B_c V_{xi} \Delta t_w V_{xi} / \Delta t_w' \right) \\ &= \beta\left(m_c V_{xi} / \Delta t_n' + \rho_w \eta B_c V_{xi}^2 \Delta t_w / \Delta t_w' \right) \end{aligned} \quad . \tag{6.10}$$

Eq. (6.10) shows the same form with Eq. (3.6) firstly modified in the present study except $\Delta t_w / \Delta t_w'$. Ratios of the collision time (Δt_w) and the virtual collision time ($\Delta t_w'$) until $V_{xw} = 0$ as changing test conditions and collided bodies in presence of the wave are presented in Fig. 6.34. In the figure, Tests No. 1 to 10 and No. 13 to 17 denote H_a=3.74m and 7.82m, respectively. From above results, it is known that the maximum collision force for H_a=7.82m is greater then H_a=3.74m. Therefore effect of the ratio of the collision time and the virtual collision time until $V_{xw} = 0$ on the maximum collision force may be greater for H_a=7.82m. The author applies a constant value $\Delta t_w / \Delta t_w' = 0.1$ into the estimation formula (Eq. 6.10). Then Eq. (6.11) can be described as follow;

$$f_{xm} = \beta\left(m_c V_{xi} / \Delta t_n' + 0.1 \rho_w \eta B_c V_{xi}^2 \right). \tag{6.11}$$

Fig. 6.35 represents the comparisons of the maximum collision forces by the numerical simulation and simplified estimation formula (Eq. 6.11). It is known that the results by the estimation formula predict well those by the numerical simulations in spite of considering some approximations described above. Consequently, the simplified estimation formula (Eq. 6.11) for the collision force of the drifted container capable for considering large deformation of the container was represented the similar form with the estimation formula (Eq. 3.6) modified in Chapter 3. However, the collision force due to the added mass for considering deformation of the container is approximately 1/10 of the collision force for non-considering within range of the collided structures considered in present study.

Finally, the virtual collision time ($\Delta t_n'$) for using the simplified estimation formula (Eq. 6.11) according to colliding conditions and collided bodies are listed in Table 6.11. Although it is difficult to determine the virtual collision time according to colliding conditions and characteristics of collided bodies, it is known that the values in case of the half- and full loaded containers are about 2.5 and 3.3 times of the empty container

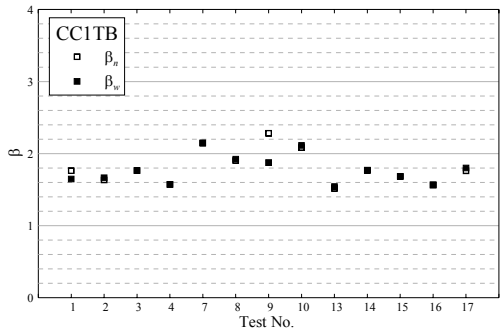

(a) CC1TB

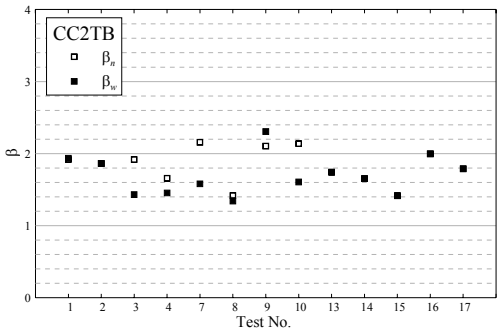

(b) CC2TB

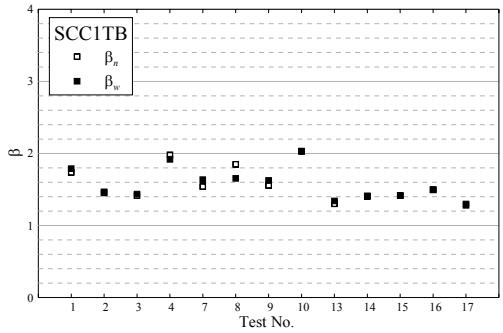

(c) SCC1TB

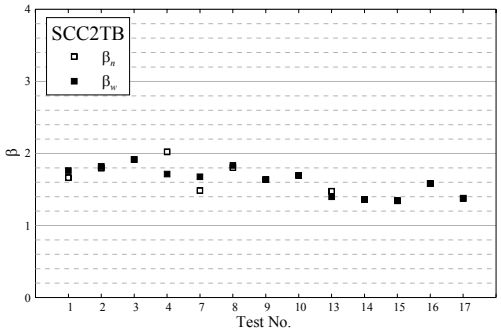

(d) SCC2TB

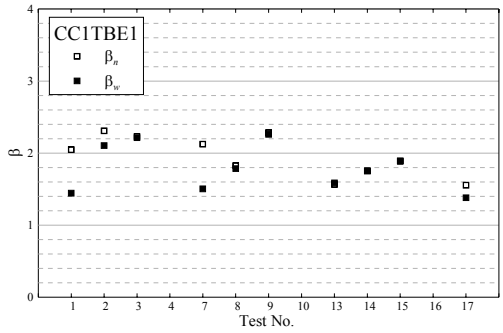

(e) CC1TBE1

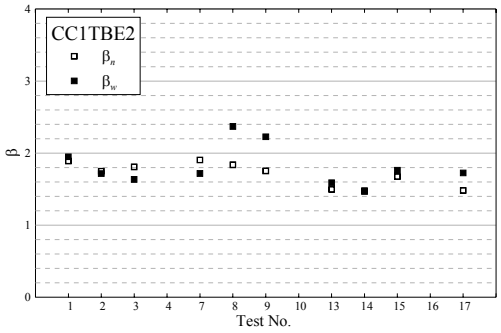

(f) CC1TBE2

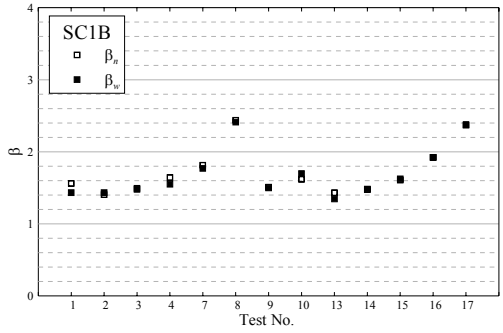

(g) SC1B

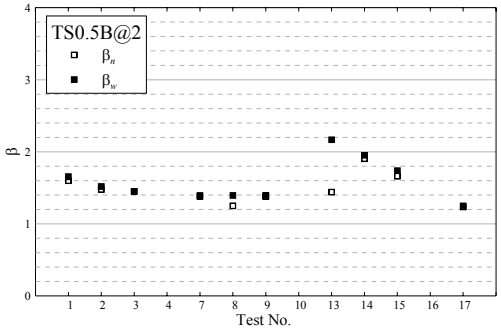

(h) TS0.5B@2

Fig. 6.32 Integrated coefficients by drifting collision simulations in full-scale; β_n is in absence of wave and β_w is in presence of wave

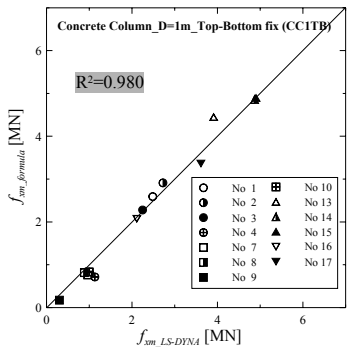

(a) CC1TB

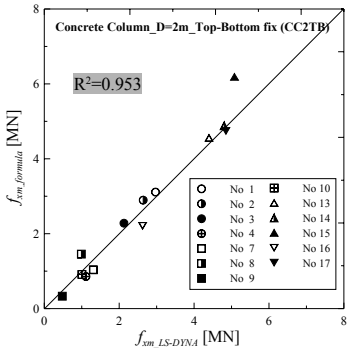

(b) CC2TB

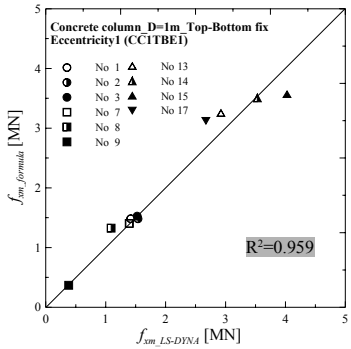

(c) SCC1TB

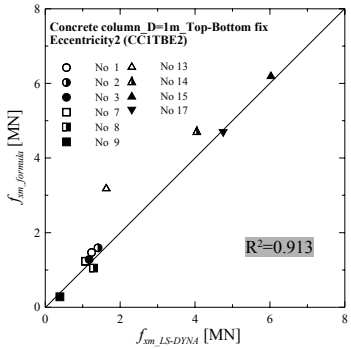

(d) SCC2TB

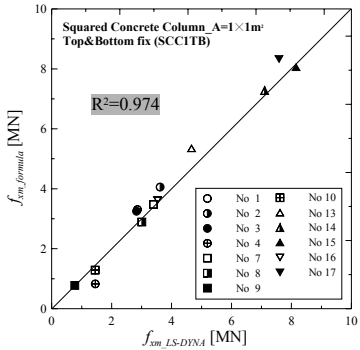

(e) CC1TBE1

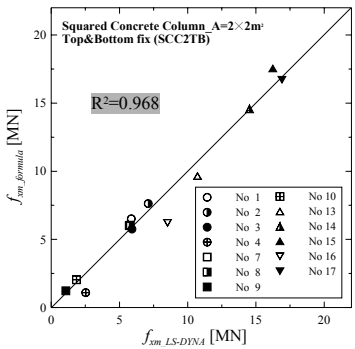

(f) CC1TBE2

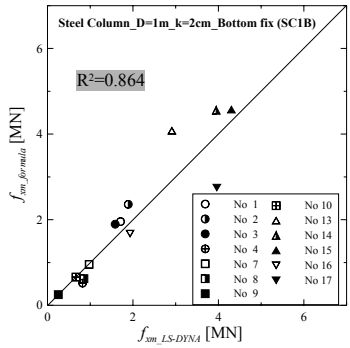

(g) SC1B

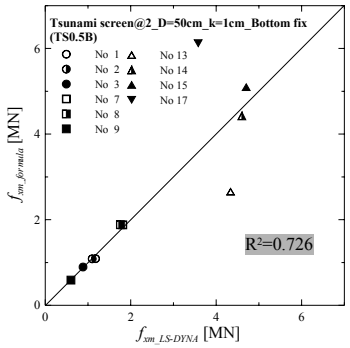

(h) TS0.5B@2

Fig. 6.33 Collision forces by the estimation formula (Eq. 6.9) using constant integrated coefficient and numerical simulation

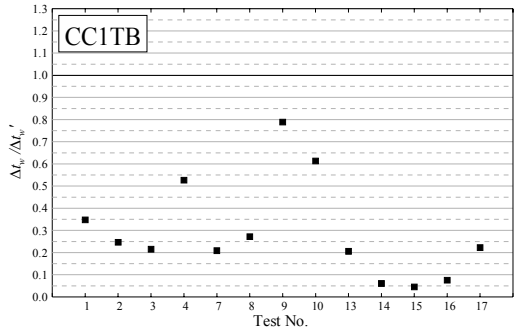

(a) CC1TB

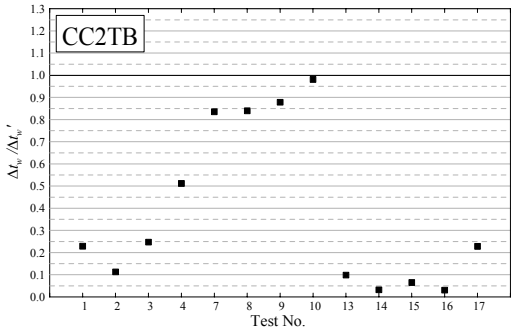

(b) CC2TB

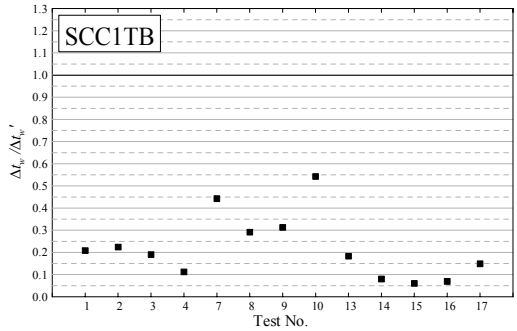

(c) SCC1TB

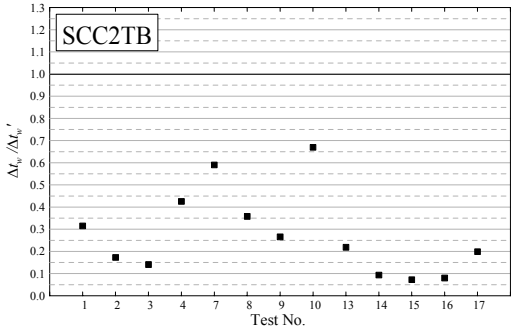

(d) SCC2TB

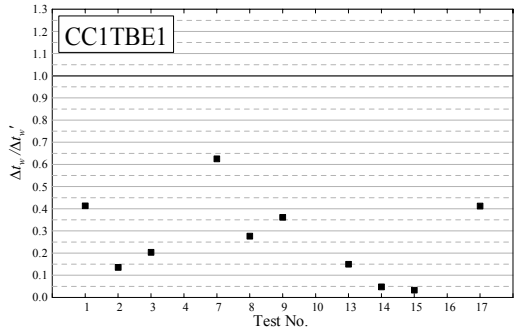

(e) CC1TBE1

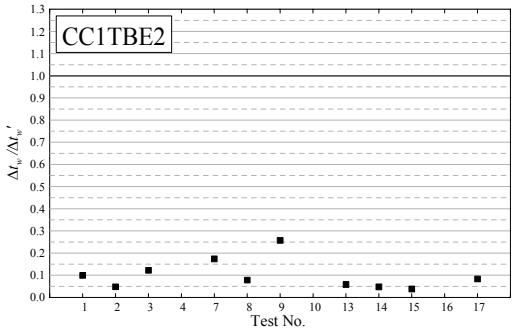

(f) CC1TBE2

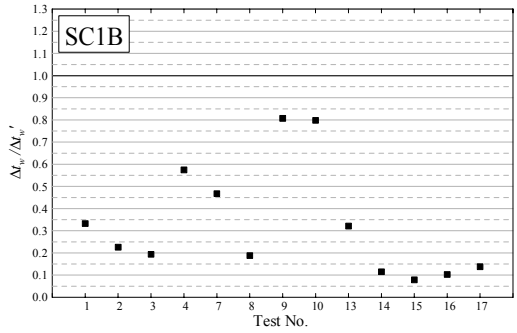

(g) SC1B

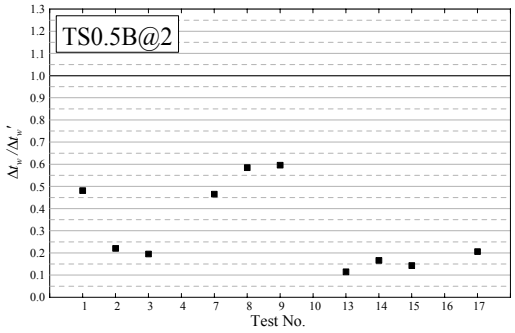

(h) TS0.5B@2

Fig. 6.34 Ratio of the collision time (Δt_w) and the virtual collision ($\Delta t_w'$) time until $V_{xw} = 0$

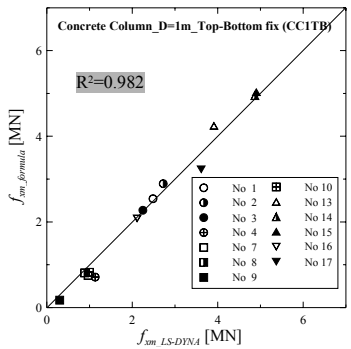

(a) CC1TB

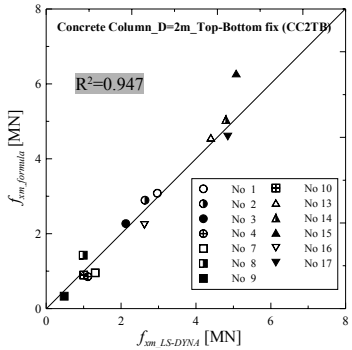

(b) CC2TB

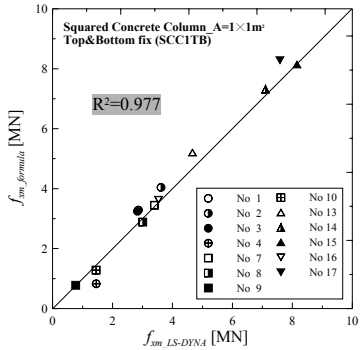

(c) SCC1TB

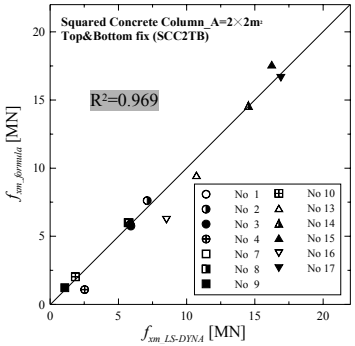

(d) SCC2TB

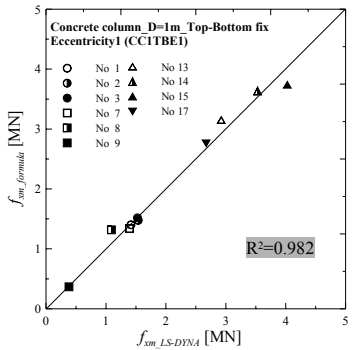

(e) CC1TBE1

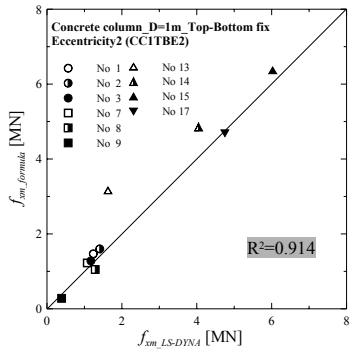

(f) CC1TBE2

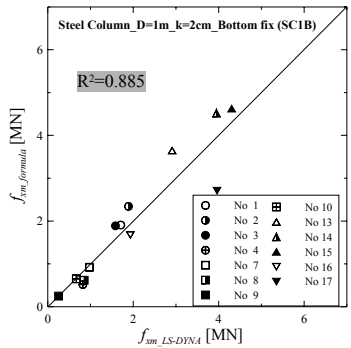

(g) SC1B

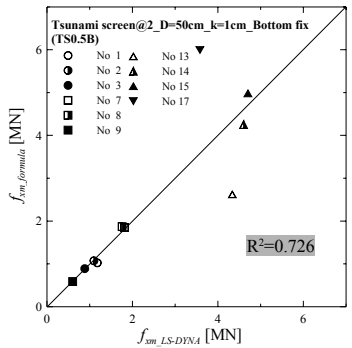

(h) TS0.5B@2

Fig. 6.35 Comparisons of the maximum collision forces by the numerical simulation and simplified estimation formula (Eq. 6.11)

Table 6.11 Virtual collision time ($\Delta t_n'$) in the simplified estimation formula (Eq. 6.11)

	CC1TB	CC2TB	SCC1TB	SCC2TB	CC1TBE1	CC1TBE2	SC1B	TS0.5B@2
No. 1	0.01028	0.00989	0.00749	0.00492	0.02406	0.01992	0.01372	0.02142
No. 2	0.02539	0.02963	0.01714	0.01069	0.06401	0.05124	0.03139	0.05740
No. 3	0.03523	0.04117	0.02327	0.01544	0.06756	0.06973	0.04240	0.07527
No. 4	0.01023	0.00997	0.00833	0.00745	-	-	0.01415	-
No. 7	0.01787	0.01635	0.00363	0.00246	0.01273	0.01210	0.01454	0.00598
No. 8	0.03887	0.02575	0.01029	0.00583	0.03051	0.03332	0.05105	0.01400
No. 9	0.06235	0.03807	0.01307	0.00974	0.03750	0.04271	0.04358	0.01523
No.10	0.00823	0.00882	0.00500	0.00371	-	-	0.01043	-
No.13	0.01641	0.01621	0.01155	0.00534	0.02398	0.02240	0.01925	0.03110
No.14	0.05913	0.06175	0.03431	0.01452	0.08749	0.06038	0.06504	0.07859
No.15	0.09284	0.07844	0.04906	0.01915	0.13557	0.07256	0.10140	0.10612
No.16	0.07523	0.07447	0.03746	0.01868	-	-	0.09389	-
No.17	0.05184	0.03838	0.01729	0.00733	0.06497	0.03534	0.06223	0.03100

for H_a=3.74m, and 3.2 and 4.5 times for H_a=7.82m. By using the estimation formula with these integration coefficient and virtual collision time, collision force of the container drifted by the run-up tsunami with back-yard structures on the container terminal could be easily obtained.

6.5 Remarks

In order to apply the estimation formula to actual fields, it is necessary to compare with the tests in prototype condition. The laboratory experiments for collision of the drifted container in full-scale are very difficult actually because of enormous cost, time and limitations of facilities. To solve this difficulty, the estimation formula was compared with the numerical analysis applying LS-DYNA in full-scale.

As a result, the author obtained the following results:

1. The author employed Arikawa et al.'s (2007) container collision experiments for the freely falling in the air scaled in 1/5 to verify the applicability of LS-DYNA in the large scale collision. The maximum collision forces by LS-DYNA represented the same degrees with the experimental results for each collision velocity on the whole, and the applicability of LS-DYNA to large scale simulation was verified.
2. The present study revised the modified estimation formula in order to apply to the case of the large deformation of the container. From comparisons of the maximum collision forces by the numerical simulation in full-scale and the estimation formula, the applicability of the estimation formula to prototype conditions was confirmed. However, when energy loss of the collided body is occurred severely due to its large deformation, the estimation formula is not able to apply.
3. By considering specific integration coefficients (β_n and β_w) and adoption of the virtual collision time ($\Delta t_n'$ and $\Delta t_w'$) until stop the container movement, the estimation formula, which is capable of considering large deformation of the container, was become simply as the similar form with the firstly modified estimation formula. However, the collision force due to the added mass for considering deformation of the container was approximately 1/10 of the non-considering.

CHAPTER 7
CONCLUSION

This chapter summarizes the works that were done in this dissertation and discusses future works. In tsunami attack, it could be occurred the direct tsunami damages such as human loss, inundation and collapse of structures due to the run-up wave but also the indirect tsunami damages by drifted bodies, e.g, driftwoods, vessels, vehicles, containers and destroyed debris of structure. These indirect damages, which the bodies drifted by run-up wave collide with other back-yard structure and fall down sea route or berth, are concerned. In recent years, cargo amount is increasing via port according to economic growth, and freight container is playing an important role among them. In this study, thus the indirect damages by the freight container were discussed. The behavior of the container drifted by run-up tsunami on the apron was examined by the laboratory experiments. Furthermore the existing estimation formula for the collision force of drifted container was review for application, and the validity of the modified estimation formula was verified through comparisons with the laboratory experiments as well as the numerical experiments based on FSI (Fluid-Structure Interaction) analysis. Finally, applicability of the estimation formula to actual phenomenon was confirmed through the full scale numerical simulations.

Before examining the behavior of the drifted container, the relationship between the maximum run-up wave level and the maximum fluid velocity were investigated in the laboratory experiments. The waves considered in the examination of behavior of the drifted container had the maximum fluid velocity which is approximately 1.5 times of the long period wave velocity based on the maximum run-up wave level. For drifting behavior, container models scaled in 1/75 and a continuous sea wall and a rectangular structure were employed as colliding and collided bodies, respectively. For collision with the continuous sea wall, it was confirmed that the drifted container, which was not collided due to the effect of the reflected waves, shifted the direction to the seaward or revolved on its axis in the complex wave fields. The container was then either stopped

on the apron or fallen down into the sea. It is, therefore, necessary to investigate the countermeasures for preventing the container falling down into the sea, especially a sea route or a berth in the port. Besides, the behavior of the drifted container on the apron in presence of a rectangular structure is discussed. Most container models were drifted away to the rear side of the structure due to the flows on the sides of the structure. As the results, it was pointed out that the damages due to the drifted bodies are able to occur in not only the coastal area but also the inland area.

Additionally, the collision force of a drifted container with a column and the wave force were discussed. The wave force acting on the column could be increased due to the presence of the drifting body in spite of slow fluid velocity and small run-up wave level, and it is expected that tsunami damages are extended due to the bodies drifted by the run-up tsunami. Therefore, the proper countermeasures should be established on the potential damages due to the drifting bodies.

Furthermore, the influence of the presence of the water behind the container on the collision force of the drifted container was discussed. The experiments were conducted both in presence and in absence of water, respectively, and an acrylic resin plate was employed as the collided body. From the results, it was known that the collision force and the collision time in presence of water is larger than in absence of that. In order to evaluate the effect of the added mass, this study examined and modified the estimation formula for collision force of drifted container proposed by Mizutani et al. (2005).

This formula has the concept that the changing amount of momentum for the collision is equal to the impulse, and considers the constant maximum collision force in the impulse. In this study, the time variation of the collision force was considered in the impulse instead of the constant maximum collision force of the original formula. To verify the modified estimation formula, the author compared with the hydraulic model experiments. The collision tests were conducted with various weighted 40ft container models as the colliding body and three kinds of the acrylic resin plates which are k2, k3 and k4 (2, 3 and 4mm in thickness) as the collided body. From comparison of the estimation formula and experimental results, it was confirmed that the collision forces from the modified estimation formula more agreed with the results from the experiment than the original estimation formula.

The validity of the modified formula for various conditions was also demonstrated through the numerical experiments. In order to calculate the drifting collision force of the container exactly, reproducing of the whole process for drifting collision due to the run-up tsunami is necessary, in which generating and propagating of tsunami, the run-up onto the land, drifting of object, colliding with other structure, reproducing of

deformation of colliding and collided bodies and estimating collision force are involved. This process was analyzed by using ALE (Arbitrary Lagrangian Eulerian) method in FE (Finite Element) model such as LS-DYNA, a code for nonlinear dynamic analysis of structures in three dimensions. However this code has a weakness, i.e., high calculation load. In this study, in order to reduce calculation load in the LS-DYNA, a drifting model using IB (Immersed Boundary) method was adopted from wave generation to just before the collision and a collision model, LS-DYNA, was utilized during the collision phase in which results from the drifting model were employed in the collision model as initial conditions.

Before estimating collision force by the drifting collision simulation, verifications of the drifting model as well as the collision model were conducted. The wave level and fluid velocity by the drifting model were in good agreement with the experimental ones. Besides, through freely falling container tests, the validity of the collision model was verified. The author performed the coupling of the drift and collision models to reduce calculation load. However, it is unreasonable to consider whole the range of the wave behind the drifted container. Thus, the collision simulations were carried out as changing wave range (length) behind the container, and it was found that the maximum collision force and collision time represent uniform values for the range of the run-up wave behind the drifted container considering extent or over. And from the distribution of the fluid velocity behind the container at the moment of the maximum collision force, deceleration was not confirmed in the rear side of the water. The effective range of the run-up wave behind the container depends on the conditions of collision, therefore the distribution of fluid velocity behind the drifted container at the moment of maximum collision force should be confirmed to judge appropriateness of the water length considered in the numerical simulation.

Additionally, the drifting collision forces by the collision simulation using the results, which are the drifting velocity of container, fluid velocity and run-up wave level behind the container, obtained in the drifting simulation was compared with the experimental ones, and good agreement was confirmed. As above, the validity of the coupling system of the drifting and collision models for the drifting collision analysis was verified.

The author examined the collision simulations using the results from the drifting model at the maximum run-up wave level and the maximum drifting velocity, and it was known that the collision force at the maximum drifting velocity was greater than the value at the maximum wave level. Hence, the author considered the results (drifting velocity of container and behind wave level), which is employed in the collision simulation, at the maximum drifting velocity in the numerical drifting experiments.

In order to obtain the drifting velocity of container and the run-up wave level behind

the container, wave condition and class, weight and initial direction of container were considered in the numerical drifting simulations, in which five kinds of wave conditions, 20ft and 40ft containers in class, empty, half- and full-loaded containers in weight, and lateral and longitudinal directions of container were employed as calculation conditions.

Moreover, to verify the modified estimation formula for the collision force of the drifted container by the run-up tsunami, the numerical collision experiments using the results in the container drifting simulations were carried out. Six kinds of initial conditions (Test No. 13~15 and 18~20) considering effects of container weight, wave height and wave period were investigated, besides five kinds of acrylic resin plate (2 to 6mm in thickness) were employed as varying stiffness of the collided body. It was confirmed that the results by the estimation formula were in good agreement with the numerical ones on the whole, as the results the validity of the modified estimation formula for the collision force of the drifted container was verified.

In order to use the LS-DYNA to verify the estimation formula in accrual phenomenon, the author employed Arikawa et al.'s (2007) container collision experiments for the freely falling in the air scaled in 1/5 which is close to the full scale. It was found that the collision forces by the laboratory and numerical experiments represented the same degrees for each collision velocity on the whole, and the applicability of the LS-DYNA in large scale simulation was verified.

For actual phenomenon, large deformation of the container was occurred due to relatively high stiffness of the collided body such as a concrete column so the velocity of the container at the moment of maximum collision force was not reached to zero. Furthermore, for the estimation of the full scale collision force which depends on the collision time, considering the collision time in presence of the wave for estimating the collision forces due to the container and the added mass is unreasonable. In this case, the collision force due to the container and the added mass using the collision time in presence of wave is smaller then the collision force due to the container using the collision time in absence of wave. Thus, the author revised the modified estimation formula to apply for the large deformation of the container, and the formula was divided between the collision force due to container using the parameters from the numerical simulations in absence of the wave and the collision force due to run-up wave behind the container using the parameters from the numerical simulations in presence of the wave, and then sum of them was adopted as the final collision force. To verify applicability of it to actual phenomenon, the actual size ISO 40ft and 20ft freight containers were used as the colliding bodies and a column of the tsunami refuge terrace at Okushiri town, Hokkaido; a pier of coastal road; a light tower in container terminal;

and two posts of tsunami screen at Kushiro region, Hokkaido were considered as the collided bodies. From comparisons of the maximum collision forces by the numerical simulation in full-scale and estimation formula, the applicability of the estimation formula to actual phenomenon was confirmed.

However this estimation formula required many parameters for using hence the simplification was performed. Through considering specific integration coefficients (β_n and β_w) and adoption of the virtual collision times ($\Delta t_n'$ and $\Delta t_w'$) until stop the container movement, the simplified estimation formula for the collision force of the drifted container capable for considering large deformation of the container was become as the similar form with the firstly modified estimation formula. However, the collision force due to the added mass for considering deformation of the container was approximately 1/10 of the collision force for non-considering within range of the collided structures considered in this study. By using the estimation formula with these integration coefficient and virtual collision time, the collision force of the container drifted by run-up tsunami with back-yard structure could be easily obtained.

Reference

Amsden, A.A. and Harlow, F.H., 1970. A Simplified MAC Technique for Incompressible Fluid Flow Calculation, *Journal of Computational Physics*, Vol. 6, pp. 322-325.

Anno, K., Nishihata, T. and Moriya, Y., 2007. Numerical and Experimental Study on Drift Due to Tsunami for Several Drifting Bodies, *Annual Journal of Coastal Engineering*, JSCE, Vol. 54, pp. 866-870 (In Japanese).

Arikawa, T., Nakano, Fumitake, Ohtsubo, D., Shimosako, K. and Ishikawa, N., 2007. Research on Destruction and Deformamtion of Structures Due to Surge Front Tsunami, *Annual Journal of Coastal Engineering*, JSCE, Vol. 54, pp. 841-845 (in Japanese).

Arikawa, T., Ohtsubo, D., Nakano, F., Shimosako, K., Takahashi, S., Imamura, F. and Matsutomi, H., 2006. Large Model Test on Surge Front Tsunami Force, *Annual Journal of Coastal Engineering*, JSCE, Vol. 53, pp. 796-800 (in Japanese).

Arikawa, T., Orita, T., Kuroda, T. and Shimosako, K., 2003. Experimental Study on Impulsive Loading Acting on the Wall by Wave Dissipating Concrete Block, *Proceedings of Coastal Engineering*, JSCE, Vol. 50, pp. 716-720 (in Japanese).

Asakura, R., Iwase, K., Ikeya, T, Takao,M., Kaneto, K., Fujii, N. and Ohmori, M., 2000. An Experimental Study on Wave Force Acting on On-Shore Structures due to Overflowing Tsunamis, *Proceedings of Coastal Engineering*, JSCE, Vol. 47, pp. 911-915 (in Japanese).

Atahan, A.O., 2006. Finite-Element Crash Test Simulation of New York Portable Concrete Barrier with I-Shaped Connector, *Journal of Structural Engineering*, ASCE, Vol. 132, No. 3, pp. 430-440.

Brackbill, J.U., Kothe, D.B. and Zemach, C., 1992. A Continuum Method for Modeling Surface Tension, *Journal of computational Physics*, Vol. 100, pp. 335-354.

Broadhouse, B.J., 1995. The Winfrith Concrete Model in LS-DYNS3D, *Report: SPD/D(95)363*, Structural Performance Department, AEA Technology, Winfrith Technology Centre, U.K.

Børvik, T., Hanssen, A.G., Dey, S., Langberg, H. and Langseth, M., 2008. On the Ballistic and Blast Load Response of a 20ft ISO Container Protected with Aluminium Panels Filled with a Local Mass - Phase I: Design of Protective System, *Engineering Structures*, Elsevier, Vol. 30, pp. 1605-1620.

Chakravarthy, S.R. and Osher, S., 1985. A New Class of High Accuracy TVD Schemes for Hyperbolic Conservation Law, *AIAA Paper*, 85-0363.

Choi, B.H., Hong, S.J., Hwang, D., Hidayat, R., Kaistrenko, V., Korolev, Yu., Kukin, A., Pelinovsky, E., Polukhin, N., Prasetya, G., Razzhigaeva, N., Subandono, D., Yalciner, A., Yoon, S.B. and Zaitsev, A., 2005. Catastrophic Tsunami in the Indian Ocean (December 26, 2004): Data of Two Field Surveys and Numerical Simulation, Sumatra Tsunami on 26 December 2004, *Proceedings of the Special Asia Tsunami Session*, Asia and Pacific Coasts, pp. 159-187.

Choi, J.-I., Oberoi, R.C., Edwards, J.R. and Rosati, J.A., 2007. An Immersed Boundary Method for Complex Incompressible Flows, *Journal of Computational Physics*, Vol. 224, pp. 757-784.

Chopra, A.K., 2007. Dynamics of Structures - Theory and Applications to Earthquake Engineering, Third Edition, *Upper Saddle River*, New Jersey, Prentice Hall, p876.

Elmarakbi, A., Sennah, K., Samaan, M. and Siriya, P., 2006. Crashworthiness of Motor Vehicle and Traffic Light Pole in Frontal Collision, *Journal of Transportation Engineering*, ASEC, Vol. 132. No. 9, pp. 722-733.

El-Tawil, S., Severino, E. and Fonseca, P., 2005. Vehicle Collision with Bridge Piers, *Journal of Bridge Engineering*, ASCE, Vol. 10, No. 3, pp. 345-353.

Fujii, N., Fukuyama, T., Inagaki, S., Ikeya, T., Yanagisawa K. and Ohmori, M., 2007. Experimental Study on Variability in Drifting Behavior Due to Tsunami and Its evaluation Method, *Annual Journal of Coastal Engineering*, JSCE, Vol. 54, pp. 241-245 (In Japanese).

Fujii, N., Ohmori, M., Ikeya, T., Asakura, R., Iriya, T. and Yanagisawa, K., 2005a. Fundamental Study on Behavior of Drifting Bodies Due to Tsunami, *Annual Journal of Civil Engineering in the Ocean*, JSCE, Vol. 21, pp. 127-132 (In Japanese).

Fujii, N., Ohmori, M., Ikeya, T., Asakura, R., Takeda, T. and Yanagisawa, K., 2005b. Numerical Simulation of Tsunami Drifting Bodies in a Harbor, *Annual Journal of Coastal Engineering*, JSCE, Vol. 52, pp. 296-300 (In Japanese).

Germano, M., Piomelli, U., Moin, P. and Cabot, W.H., 1991. A Dynamic Subgrid-Scale Eddy Viscosity Model, *Physics and Fluids A*, Vol. 3, No. 7, pp. 1760-1765.

Golshani, A., Mizutani, N, Hur, D.-S. and Shimizu, H., 2003. Three-Dimensional Analysis on Nonlinear Interaction between Water Waves and Vertical Permeable Breakwater, *Coastal Engineering Journal*, JSCE, Vol. 45, No. 1, pp. 1-28.

Haehnel. Robert B. and Daly. Steven F., 2004. Maximum Impact Force of Woody Debris on Floodplain Structure, *Journal of Hydraulic Engineering*, ASCE, Vol. 130, pp. 112-120.

Hallquist, J.O., 1976. A Procedure for the Solution of Finite Deformation Contact-Impact Problems by the Finite Element Method, *University of California*, Lawrence Livermore National Laboratory, Rept. UCRL-52066.

Hanssen, A.G., Girard, Y., Olovsson, L., Berstad, T. and Langseth, M., 2006. A Numerical Model for Bird Strike of Aluminium Foam-Based Sandwich Panels, *International Journal of Impact Engineering*, Vol. 32, pp. 1127-1144.

Hinatsu, M., 1992. Numerical Simulation of Unsteady Viscous Nonlinear Waves Using Moving Grid System Fitted on a Free Surface, *Journal of the Kansai Society of Naval Architects*, Vol. 217, pp. 1-11.

Hirt, C.W. and Nichols, B.D., 1981. Volume of Fluid (VOF) Method for Dynamics of Free Boundaries, *Journal of Computational Physics*, Vol. 39, pp. 201-225.

Hur, D.-S. and Mizutani, N., 2007. Sand Suction Mechanism in Artificial Beach Composed of Rubble Mound Breakwater and Reclaimed Sand Area, *Ocean engineering*, Elsevier, Vol. 3, No. 8-9,

pp. 1104-1119.

Ikeno. M., Mori. N. and Tanaka. H., 2001. Experimental Study on Tsunami Force and Impulsive Force by a Drifter under Breaking Bore Like Tsunamis, *Proceedings of Coastal Engineering*, JSCE, Vol. 48, pp. 846-850 (In Japanese).

Ikeno. M. and Tanaka. H., 2003. Experimental Study on Impulse Force of Drift Body and Tsunami Running Up to Land, *Proceedings of Coastal Engineering*, JSCE, Vol. 50, pp. 721-725 (In Japanese).

Ikeya, T., Asakura, R., Fujii, N., Ohmori, M., Takeda, T. and Yanagisawa, K., 2005. Experiment on Tsunami Wave Force Acting on a Floating Body and Development of an Evaluation Method, *Annual Journal of Coastal Engineering*, JSCE, Vol. 52, pp. 761-765 (in Japanese).

Ikeya, T., Inagaki, S., Asakura, R., Fukuyama, T., Fujii, T., Ohmori, M., Takeda, T. and Yanagisawa, K., 2006. Experimental and Analytical Study of Impulsive Forces by a Drifter due to Tsunami, *Annual Journal of Coastal Engineering*, JSCE, Vol. 53, pp. 276-280 (in Japanese).

Ikeno, M. and Tanaka, H., 2003. Experimental Study on Impulse Force of Drift Body and Tsunami Running Up to Land, *Annual Journal of Coastal Engineering*, JSCE, Vol. 50, pp. 721-725 (in Japanese).

Imamura, F., Arikawa, T., Tomita, T., Yasuda, T. and kawata, Y., 2005. Field Investigation on the 2004 Indian Ocean Tsunami in the Southwestern Coast of Sri Lanka, Sumatra Tsunami on 26 December 2004, *Proceedings of the Special Asia Tsunami Session at APAC*, pp. 93-05.

Ishii, T., Hashimoto, A. and Nakamura, Y., 2006. Numerical Simulation of Parachute Opening Using an Immersed Boundary Method, *Proceedings of Japan Society of Fluid Mechanics*, JSFM, B4-3.

Ishikawa, N., 1993. Impact Behavior and Design of Structures, Structural Engineering Series 6, *Subcommittee of Impact Problems, Committee of Structural Engineering*, Japan Society of Civil Engineers, 312p.

Japanese Industrial Standards Committee, 1994. Freight Containers for International Trade - External Dimensions and Ratings, *JIS Z1614*, 4p.

JSCE Concrete Committee, 1996. Standard Specification for Concrete Structures - Design, *Maruzen co., LTD.*, 230p.

Kawasaki, K., 2005a. Numerical Model of 2-D Multiphase flow with Solid-Liquid-Gas Interaction, *International Journal of Offshore and Polar Engineering*, Vol. 15, No. 3, pp. 198-203.

Kawasaki, K., 2005b. Numerical Simulation of Solid-Gas-Liquid Phase Flow in a Three-Dimensional Field, *Proceedings of 3rd International Conference on Asian and Pacific Coasts*, Jeju, Korea, pp. 1868-1879.

Kawasaki, K., Hakamata, M. and Ogiso, K., 2007. Development of Multiphase Flow Model "Dolphin-2D/3D" with Irregular Mesh Size Grids and Dynamic Motion Analysis of Multiple Rigid Bodies, *Annual Journal of Civil Engineering in the Ocean*, JSCE, Vol. 23, pp. 207-212 (In Japanese).

Kawasaki, K. and Ogiso, K., 2008. Sophistication of Two-Dimensional Multiphase Flow Model

Taking into Account Lagrange Analysis of Rigid Bodies and Constitutive Law of Bingham Fluid, *Annual Journal of Coastal Engineering*, JSCE, Vol. 55, pp. 36-40 (in Japanese).

Kim, J.-H. and Shin, H.-C., 2008. Application of the ALE Technique for Underwater Explosion Analysis of a Submarine Liquefied Oxygen Tank, *Ocean Engineering*, Elsevier, Vol. 35, pp. 812-822.

Kishi, N., 2004. Practical Methods for Impact Test and Analysis, Structural Engineering Series 15, *Subcommittee of Impact Problems, Committee of Structural Engineering*, Japan Society of Civil Engineers, 167p (In Japanese).

Koike, T., 2007. Study on Behavior of Drift vessels Due to Tsunami and Collision Forces, *Bachelor Thesis*, Nagoya University, 25p (in Japanese).

Kumagai, K., Oda, K. and Fujii, N., 2006. Applicability of Simulation Model for Drift Behavior of Containers Due to Tsunami, *Annual Journal of Coastal Engineering*, JSCE, Vol. 53, pp. 241-245 (in Japanese).

Kumagai, K., Oda, K. and Fujii, N., 2007. Simulation Model for Drift Behavior of Container due to Tsunami and Collision Force, *Annual Journal of Coastal Engineering*, JSCE, Vol. 54, pp. 236-240 (in Japanese).

Kumagai, K., Oda, K. and Fujii, N., 2008. The Field Experiment for Containers Floating on Sea Surface and Numerical Simulation of Container Drift, *Annual Journal of Coastal Engineering*, JSCE, Vol. 55, pp. 271-275 (in Japanese).

Kunugi, T., 2000. MARS for Multiphase Calculation, *CFD Journal*, Vol. 9, No. 1, IX-563.

Lee, K.-H. and Mizutani, N., 2007. Numerical Wave Flume with Immerged Boundary Method and Its Applicability in Wave Field Simulation around a Horizontal Circular Cylinder, , *Annual Journal of Coastal Engineering*, JSCE, Vol. 54, pp. 821-825 (In Japanese).

Lima E Silva, A.L.F., Silveira-Nero, A. and Damasceno, J.J.R., 2003. Numerical Simulation of Two Dimensional Flows Over a Circular Cylinder Using the Immersed Boundary Method, *Journal of Computational Physics*, Vol. 189, pp. 351-370.

LSTC, 2003. LS-DYNA Keyword User's Manual Version 970, *Livermore Soft Technology Corporation*, USA.

LSTC, 2006. LS-DYNA Theory Manual, *Livermore Soft Technology Corporation*, USA.

Ma, J. and Usman, M., 2004. Modeling of Fuel Sloshing Phenomena Considering Solid-Fluid Interaction, *Proceedings of 8th International LS-DYNA Users Conference*, 4-15.

Matsutomi, H., 1999. A Practical Formula for Estimating Impulsive Force Due to Driftwoods and Variation Features of the Impulsive Force, *Journal of Hydraulic, Coastal and Environmental Engineering*, JSCE, No. 621, II-47, pp. 111-127 (In Japanese).

Matsutomi, H., Fujii, M. and Yamaguchi, T., 2007. Experiments and Development of a Model on the Inundated Flow with Floating Bodies, *Annual Journal of Coastal Engineering*, JSCE, Vol. 54, pp. 226-230 (In Japanese).

Matsutomi, H. and Iizuka, H., 1998. Tsunami Current Velocity on Land and Its Simple Estimation Method, *Annual Journal of Coastal Engineering*, JSCE, Vol. 45, pp. 361-365 (In Japanese).

Ministry of Land, Transport and Maritime Affairs, Korea, 2005. Design Criterion of Port and Fishery Harbor, *Korean Port and Harbour Association*, 1637p (In Korean).

Minorsky, V.U., 1959. An Analysis of Ship Collision with Reference to Protection of Nuclear Power Ships, *Journal of Ship Research*, Vol. 3, No. 2, pp. 1-4.

Mizutani, N., Shiraishi, K., Usami, A., Miyajima, S., and Tomita, T., 2006. Experimental Study on Tsunami Excitation on Container Rested on Apron and Collision Force of Drift Container, *Annual Journal of Coastal Engineering*, JSCE, Vol. 53, pp. 791-795 (In Japanese).

Mizutani, N., Takagi, Y., Shiraishi, K., Miyajima, S., and Tomita, T., 2005. Study on Wave Force on a Container on Apron due to Tsunamis and Collision Force of Drifted Container, *Annual Journal of Coastal Engineering*, JSCE, Vol. 52, pp. 741-745 (In Japanese).

Morinishi, Y. and Vasilyev, O.V., 2001. A Recommended Modification to the Dynamic Two-Parameter Mixed Subgrid Scale Model for Large Eddy Simulation of Wall Bounded Turbulent Flow, *Physics and Fluids*, Vol. 13, No. 11, pp. 3400-3410.

Motora, S., Fujino, M., Sugiura, M. and Sugita, M., 1971. Equivalent Added Mass of Ships in Collisions. *Selected Papers from the Journal of the Society of Naval Architects of Japan*, Vol. 7, pp. 138-148.

Nakamura, T., Kuramitsu, Y. and Mizutani, N., 2008. Tsunami Scour around a Square Structure, *Coastal Engineering Journal*, JSCE, Vol. 50, No. 2, pp. 209-246.

Nakamura, T., Shiraishi, K., Usami, A., Mizutani, N., Miyajima, S. and Tomita, T., 2006. Three-Dimensional Numerical Analysis on Tsunami Waves around Container on Apron and Tsunami-Induced Wave Pressure and Tsunami Force Acting on Containers*, Annual Journal of Civil Engineering in the Ocean*, Vol. 22, pp. 517-522 (in Japanese).

National Astronomical Observatory of Japan, 2003. Chronological Scientific Tables, *Maruzen Co., Ltd*., Tokyo, 945 p. (in Japanese).

National Diet Material Compilation Committee of Japan, 1998. Natural disaster on Japan, *Hirakawa Kogyosha Co,, Ltd*., Tokyo, 637p (in Japanese).

Ohmori, M., Fujii, N., Kyouya, O., Takao, M., Kaneto, T. and Ikeya, T., 2000. Numerical Simulation of Water Level, Velocity and Wave Force Overflowed on Upright Seawall by Tsunamis, *Proceedings of Coastal Engineering*, JSCE, Vol. 47, pp. 376-380 (in Japanese).

Osher, T. and Chakravarthy, S., 1984. Very High Order Accurate TVD Schemes, *ICASE Report*, No. 84-44, NASA Langey Research Center, Virginia, 64p.

Peskin, C.S, 1977. Numerical Analysis of Blood Flow in the Heart, *Journal of Computational Physics*, Vol. 25, pp. 220-252.

Petersen, M.j. and Pedersen, P.T., 1981. Collision between Ships and Offshore Platforms, *Offshore Technology Conference*, Houston, USA, Paper OTC 4134.

Rider, W.J. and Kothe, D.B., 1998. Reconstruction Volume Tracking, *Journal of Computational Physics*, Vol. 141, pp. 112-152.

Saji, T., Matsufuji, Y. and Ohkubo, T., 1985. A Basic Study on the Method of the Evaluation of Impact Bending Strength for Brittle Materials, *Journal of Structural and Construction Engineering (Transactions of AIJ)*, No. 358, pp. 10-21 (In Japanese).

Salvetti, M.V. and Banerjee, S., 1995. A Priori Tests of a New Dynamic Subgrid-Scale Model for Finite Difference Large-Eddy Simulations, *Physics and fluids*, Vol. 7, No. 11, pp. 2831-2847.

Simamora, C., Shiginori, Y. and Fujima, K., 2007. Experimental Study on Tsunami Forces Acting on Structures, *Annual Journal of Coastal Engineering*, JSCE, Vol. 54, pp. 831-835 (in Japanese).

Shiraishi, K., 2007. Study on behavior of Drift Container Due to Run-up Tsunami and its Impact Force, *Master Thesis*, Nagoya University, 30p (in Japanese).

Smagorinsky, J., 1963. General Circulation Experiments with the Primitive Equations, *Monthly Weather Review*, Vol. 91, No. 3, pp. 99-164.

Souli, M., Olovsson, L. and Do, I., 2002. ALE and Fluid-Structure Interaction Capabilities in LS-DYNA, *Proceedings of 7th International LS-DYNA Users Conference*, 10-27.

Souli, M., Ouahsine, A. and Lewin, L., 2000. ALE Formulation for Fluid-Structure Interaction Problems*, Computer Methods in Applied Mechanics and Engineering*, Vol. 190, pp. 659-675.

Takagi, U., 2005. Study on Tsunami Force Acting on a Container on Apron and Behavior of Drifting Container, *Master Thesis*, Nagoya University, 31p (in Japanese).

Tatsumi, D., Takahashi, S., Fufima, K., Shigihara, Y., Matsutomi, H., Kosa, K., Shohi, G., and Murashima, Y., 2007. Field Survey on 2006 Java Tsunami, *Annual Journal of Coastal Engineering*, JSCE, Vol. 54, pp. 1416-1420 (In Japanese).

The Central Disaster Prevention Committee of Cabinet Office, Government of Japan, 2005. *Report*: Meiji Sanriku Earthquake Tsunami in 1896, Mizuho Information & Research Institute. Inc., 167p (In Japanese).

Tokura, S. and Ida, T., 2005. Simulation of Wave-Dissipating Mechanism on Submerged Structure Using Fluid-Structure Coupling Capability in LS-DYNA, *Proceedings of 5th European LS-DYNA Users Conference*, 2c-37.

Tomita, T., Kawai, H. and Kakinuma, T., 2004. Tsunami Disasters and Tsunami Characteristics Due to the Tokachi-oki Earthquake in 2003, *Technical Note of the Port and Airport Research Institute*, No. 1082, 30p (in Japanese).

Tosaka, N., Miyata, H., Shimazaki, Y., Nomura, T., Shimura, M. and Hatanaka, K., 1995. *Analysis of Moving Boundary Flows,* Computational Fluid Dynamics Series 4, University of Tokyo Press.

Tryland, T., Larsen, P.K. and Langseth, M., 2004. Design of I Beams and Deck Profiles under Concentrated Loading, *Journal of Structural Engineering*, ASCE, Vol. 130, No. 3, pp. 441-422.

Turner, M.J., Clough, R.W., Martin, H.C. and Topp, L.J., 1956. Stiffness and Deflection Analysis of Complex Structures, *Journal of Aeronautical Science*, Vol. 23, pp. 805-823.

Usami, A., 2006. Study on Excitation of Run-up Tsunami on Container on Apron and Behavior of the Drifting Container, *Bachelor Thesis*, Nagoya University, 25p (in Japanese).

Ushijima, S., Fukutani, A. and Makino, O., 2008. Prediction Method for Movements with Collisions of Arbitrarily-Shaped Objects in 3D Free-Surface Flows, *JSCE Journal B*, Vol. 64, No. 2, pp. 128-138 (in Japanese).

Ushijima, S., Takemura, M., Yamada, S. and Nezu, I., 2003. Computational Method for Multiphase Incompressible Flows (MICS) and Its Applicability to Particle-Laden Liquid Flows, *JSCE Journal*, Vol. 740/II-64, pp. 121-130 (in Japanese).

Ushijima, S., Makino, O. and Toshikawa, N., 2009. 3D Numerical Prediction for Transportation and Entrapment of Driftwood with T-Type Solid Model, *Journal of Hydroscience and Hydraulic Engineering*, Vol. 27, No. 1, pp. 11-21.

Ushijima, S., Yamada, S., Fujioka, S. and Nezu, I., 2006. Prediction Method (3D MICS) for Transportation of Solid Bodies in 3D Free-Surface Flows, *JSCE Journal B*, Vol. 62, No. 1, pp. 100-110 (in Japanese).

Van Leer, E., 1977. Towards the Ultimate Conservative Difference Scheme. IV. A New Approach to Numerical Convection, *Journal of Computational Physics*, Vol. 23, pp. 276-299.

Winslow, A.M., 1990. Equipotential Zoning of the Interior of a Three-Dimensional Mesh, *Lawrence Radiation Laboratory*, UCRL-7312.

Xiao, F., Yabe, T., Ito, T. and Tajima, M., 1997. An Algorithm for Simulating Solid Objects Suspended in Stratified Flow, *Computer Physics Communications*, Elsevier, Vol. 102, pp. 147-160.

Yoneyama, N., Nagashima, H. and Toda, K., 2008. Development of a Numerical Analysis Method for the Drift Behavior in Tsunami, *Annual Journal of Coastal Engineering*, JSCE, Vol. 55, pp. 886-890 (In Japanese).

Youngs, D.L., 1982. Time Dependent Multimaterial Flow with Large Fluid Distortion, *Numerical Methods for Fluid Dynamics*, ed. Morton, K.M. and Baines, M.J., Academic Press, 517p.

Yuki, Y., Takeuchi, S. and Kajishima, T., 2007. Efficient Immersed Boundary Method for Strong Interaction Problem of Arbitrary Shape Object with the Self-Induced Flow, *Journal of Fluid Science and Technology*, JSME, Vol. 2, No. 1, pp. 1-11.

Zang, Y., Street, R.L. and Koseff, J.R., 1993. A Dynamic Mixed Subgrid-Scale Model and Its Application to Turbulent Recirculating Flows, *Physics and Fluids A*, Vol. 5, No. 12, pp. 3186-3196.

Zhang, A. and Suzuki, K., 2007. A Comparative Study of Numerical Simulations for Fluid-Structure Interaction of Liquid-Filled Tank during Ship Collision, *Ocean Engineeri*ng, Elsevier, Vol. 34, pp. 645-652.

http://www.bousai.go.jp/

http://www.nptc.or.jp/

http://www.pref.shizuoka.jp/bousai/

http://www.town.okushiri.lg.jp/